ISTANBUL TECHNICAL UNIVERSITY ★ GRADUATE SCHOOL OF SCIENCE

ENGINEERING AND TECHNOLOGY

INVESTIGATION OF WIND TURBINE EFFECTS
ON RADAR PERFORMANCE

Ph.D. THESIS

Osman KARABAYIR

Department of Electronics and Communications Engineering

Telecommunications Engineering Programme

MAY 2016

**ISTANBUL TECHNICAL UNIVERSITY ★ GRADUATE SCHOOL OF SCIENCE
ENGINEERING AND TECHNOLOGY**

**INVESTIGATION OF WIND TURBINE EFFECTS
ON RADAR PERFORMANCE**

Ph.D. THESIS

Osman KARABAYIR
(504112307)

Department of Electronics and Communications Engineering

Telecommunications Engineering Programme

Thesis Advisor: Prof. Dr. Sedef KENT PINAR

MAY 2016

İSTANBUL TEKNİK ÜNİVERSİTESİ ★ FEN BİLİMLERİ ENSTİTÜSÜ

RÜZGAR TÜRBİNLERİNİN RADAR PERFORMANSI ÜZERİNDEKİ ETKİLERİNİN ARAŞTIRILMASI

DOKTORA TEZİ

Osman KARABAYIR
(504112307)

Elektronik ve Haberleşme Mühendisliği Anabilim Dalı

Telekomünikasyon Mühendisliği Programı

Tez Danışmanı: Prof. Dr. Sedef KENT PINAR

MAYIS 2016

Osman KARABAYIR, a Ph.D. student of ITU Graduate School of Science Engineering and Technology 504112307 successfully defended the thesis entitled "INVESTIGATION OF WIND TURBINE EFFECTS ON RADAR PERFORMANCE", which he/she prepared after fulfilling the requirements specified in the associated legislations, before the jury whose signatures are below.

Thesis Advisor :   **Prof. Dr. Sedef KENT PINAR**   ....
Istanbul Technical University

Jury Members :   **Prof. Dr. Filiz GÜNEŞ**   ....
Yıldız Technical University

    Assoc. Prof. Dr. Işın ERER   ....
Istanbul Technical University

    Prof. Dr. Funda AKLEMAN YAPAR   ....
Istanbul Technical University

    Prof. Dr. Osman Nuri UÇAN   ....
Istanbul Aydın University

Date of Submission :   **01 April 2016**
Date of Defense :   **26 May 2016**

To my spouse and son,

FOREWORD

First of all, I would like to thank my advisor Professor Sedef KENT PINAR very much for her inspiration, guidance, and patience. Professor KENT PINAR believed me and I was encouraged by her support. I would also like to thank to Prof. Dr. Filiz GÜNEŞ and Assoc. Prof. Dr. Işın ERER for their useful comments and suggestions which have improved the technical content and clarity of this thesis.

I would like to express my immense gratitude to my wife Öznur KARABAYIR and our lovely son Ahmet Yiğit KARABAYIR for their time, patience and constant encouragement I have gotten over the years. I undoubtedly could not have done this without you.

I would like to give special thanks to my colleagues: Dr. Hüseyin Avni SERİM, Dr. Senem MAKAL YÜCEDAĞ, Dr. Ahmet Faruk COŞKUN, Dr. Okan Mert YÜCEDAĞ, Uğur SAYNAK, Baki BATI, Mustafa ÜNAL, Mehmet BIYIK and Özge BATI for their invaluable supports and encouragements during my study.

I am also grateful to Dr. Deniz BÖLÜKBAŞ who founded the Radar Performance and Signature Analysis Center (RAPSİM) in The Scientific and Technological Research Council of Turkey (TÜBİTAK). My dissertation is supported by RAPSİM.

Lastly, I would like to express my gratitude to my whole family and in particular to my mother and my father.

May 2016   Osman KARABAYIR

TABLE OF CONTENTS

ABBREVIATIONS

ATC	**:**	Air Traffic Control
CA-CFAR	**:**	Cell Averaging-Constant False Alarm Rate
CFAR	**:**	Constant False Alarm Rate
CI	**:**	Coherent Integration
CPI	**:**	Coherent Processing Interval
CW	**:**	Continuous Wave
FMCW	**:**	Frequency Modulated Continuous Wave
GNN	**:**	Global Nearest Neighbor
GO	**:**	Geometrical Optics
HAWT	**:**	Horizontal Axis Wind Turbine
LFM	**:**	Linear Frequency Modulation
LoS	**:**	Line of Sight
MoM	**:**	Method of Moments
MTI	**:**	Moving Target Indicator
MTT	**:**	Multiple Target Tracking
MW	**:**	Mega Watt
NCI	**:**	Non-Coherent Integration
PD	**:**	Probability of Detection
PDA	**:**	Probabilistic Data Association
PDR	**:**	Pulse-Doppler Radar
PEC	**:**	Perfectly Electrical Conducting
PO	**:**	Physical Optics
PRF	**:**	Pulse Repetition Frequency
PRI	**:**	Pulse Repetition Interval
PSD	**:**	Power Spectral Density
PSF	**:**	Point Spread Function
RADAR	**:**	RAdar Detection and Ranging
RCS	**:**	Radar Cross Section
RPM	**:**	Revolution Per Minute
SAR	**:**	Synthetic Aperture Radar
SCV	**:**	Sub-Clutter Visibility
SNR	**:**	Signal to Noise Ratio
UHF	**:**	Ultra High Frequency
VAWT	**:**	Vertical Axis Wind Turbine
WF	**:**	Wind Farm
WGN	**:**	White Gaussian Noise
WT	**:**	Wind Turbine
WTC	**:**	Wind Turbine Clutter

LIST OF TABLES

LIST OF FIGURES

xviii

INVESTIGATION OF WIND TURBINE EFFECTS
ON RADAR PERFORMANCE

SUMMARY

Wind farm (WF) investments have recently attracted great attention throughout the world due to being an economical way of producing renewable energy. As stated in several work of the related literature, the wind farm installations are expected to increase in the following decades due to the increasing demand on wind power for producing electricity. Unfortunately, the increasing deployment rates of WFs bring along with a great need for the detailed investigation of their effects on the performance of radar systems. Due to having electrically large dimensions and rotating blades, wind turbines (WTs) have been known to violate radar operation through causing some deteriorating effects such as false alarm, reduction on radar detection sensitivity, seduction or breakage of genuine targets' tracks, shadowing, SAR image blurring and so on.

Since WTs are shown to have deteriorating effects on radar systems' performance, specification and mitigation of WT clutter (WTC) have been of great importance for radar engineers. In recent years, important research projects have been carried out in order to characterize the signals scattered by the wind turbines. However, due to the complicated scattering and motional characteristics, there have been no effective method or simulation tool which fully characterizes and mitigates the deteriorating effects of WTs. Therefore, the most radar systems that are used in the areas of defence, navigation and surveillance have been suffering from the WFs, and great effort has been spend on the researches about mitigating their adverse effects.

In order to deal with or solve the problems caused by WTs, actually the reasonable way is to investigate the origin of the problem. Therefore, presenting a comprehensible description of WF effects on detection, tracking and imaging performances of different radar services is assumed as the main goal throughout this dissertation. In this context, initially, simulation frameworks for those radar operations are prepared by also introducing a WT model that is composed of electrically small canonical segments. Then, scattering and motional characteristics of the WTs are examined in terms of theoretical and experimental aspects with the consideration of obtaining priory information about their deteriorations.

By using the related simulation frameworks and the proposed signal model, adverse WT effects on radar systems' detection and tracking performances are investigated for pulse-Doppler radar (PDR) systems which are commonly employed for various civilian and military missions. Examinations about detection characteristics of WTs pave the way of constructing an analytical wind turbine clutter (WTC) model as well as determination of detection properties of genuine targets in the vicinity of WTs. From the detection examinations, it can be concluded that the WTs might cause unpredictable and variable detection signatures in radar systems due to their

time-varying scattering properties. As an additional effort, a novel WT mitigaton approach which is based on CLEAN algorithm is also proposed after completing detection analyses.

Degradations on multiple target tracking (MTT) operation of PDRs in terms of false track generation, seduction and/or breakage of genuine targets' tracks are analyzed in the vicinity of WTs through various simulation scenarios. Performances of two different association methods namemly global nearest neighbor (GNN) and probabilistic data association (PDA) are also tested for each simulation cases. Following the examination about WT deteriorations on MTT operation, a novel WF design approach which recommends settling the WTs according to a predefined rule is proposed. Promising results obtained for the proposed WF settlements present the effectiveness of the approach in terms of mitigation of WT effects from radar tracking operation.

Lastly, studies on determining the WT effects on radar imaging applications are performed for synthetic aperture radar (SAR) systems. First of all, mathematical derivations background the problem is presented. Then, it is demonstrated through simulation results that WTs have the possibility to spread over multiple cross-range positions or desensitize the targets nearby. It can be also inferred that the effects mentioned are strongly dependent on instantaneous scattering and motional properties of the WTs.

Consequently, deteriorating effects of WTs on detection, tracking and imaging operations of radar systems are examined throughout this dissertation. Moreover, in order to employ at the detection and tracking stages of PDR systems, two novel WTC mitigation approaches are proposed. The examinations, obtained results and also introduced mitigation procedures could be utilized in forming baselines and constituting frameworks when dealing with the WT deteriorations.

RÜZGAR TÜRBİNLERİNİN RADAR PERFORMANSI ÜZERİNDEKİ ETKİLERİNİN ARAŞTIRILMASI

ÖZET

Dünyanın birçok bölgesinde, bir yenilenebilir enerji kaynağı olan rüzgâr çiftliği kurulumları her geçen gün artmaktadır. Yapılan teorik ve deneysel çalışmalar neticesinde, bu çiftliklerin bir çok radar sistemine olumsuz etkilerde bulunduğu tecrübe edilmiştir. Rüzgâr çiftliği kaynaklı olumsuz etkiler, türbinlerin yapısal, yansıtıcı ve hareket özelliklerine bağlı olarak çeşitlilik göstermektedir. Rüzgâr çiftliklerini oluşturan rüzgâr türbinleri, enerji ihtiyaçlarına bağlı olarak elektriksel olarak çok büyük boyutlarda imal edilebilmektedir. Yaklaşık 200 m'ye varan boyutları, rüzgâr türbinlerinin radar sistemlerinin elektromanyetik görüşü açısından ciddi bir engel olmasına ve dolayısıyla radar sisteminin tespit performansının düştüğü gölgelenen alanların/kör bölgelerin oluşmasına sebep olmaktadır. Yapılarında bulunan yansıtıcı özelliğe sahip yapısal malzemeler ile birlikte türbinlerin hareketli kanatları, radar sisteminde türbin kaynaklı hareketli hedef imzası oluşmasına sebep olmaktadır. Bu durum, radar sistemine sahte hedef, kargaşa ve hayalet hedef biçiminde olumsuz olarak yansımaktadır. Elektriksel olarak büyük ve yansıtıcı özellikli yapıları, rüzgâr türbinlerinin büyük RKA değerine sahip olmasına, dolayısıyla türbinlerden radara dönen işaretin genliğinin de oldukça yüksek olmasına sebebiyet vermektedir. Bu sebeple, yüksek genlikli türbin ekolarının, cıvıltı (chirp) işaret formu kullanan radar sistemlerinde uyumlu filtreleme aşamasında yüksek yan lob oluşturması, tespit aşamasında sabit yanlış alarm olasılığı (constant false alarm rate, CFAR) eşiğini yükseltmesi ve analog-sayısal çevirme (analog-to-digital, ADC) işleminin sunduğu dinamik aralığı domine etmesi gibi sebeplerle radar sisteminde gerçek hedeflere yönelik tespit kayıpları ve desensitizasyon gibi olumsuz etkilerde bulunması mümkündür. Rüzgâr çiftliklerinde bulunan türbinlerin sayıları ve bu türbinlerin radar sisteminde neden olduğu tespit anlamındaki olumsuz etkiler, radar sistemlerinin çoklu hedef takibi (multiple target tracking, MTT) performansını da olumsuz etkileyebilmektedir. Hareketli hedef imzası oluşmasına sebep olan çok sayıdaki rüzgâr türbininin radar ekranında sabit veya hareket eden sahte iz başlatması mümkündür. Bununla birlikte, rüzgâr çiftliği yakınında seyreden gerçek hedeflere ait izlerin, tespit kayıpları veya yanlış tespit ile eşleştirme gibi durumlara bağlı olarak koptuğu, yanıldığı veya belirli bir süre boyunca bekleme durumunda kaldığı bilinmektedir. Bu durumdan dolayı, gerçek hedeflerin tespit olasılığı (probability of detection, PD) performansı zafiyete uğramaktadır.

Literatürde, rüzgâr türbinlerinin radar sisteminde tespit edilmesine yönelik çok sayıda çalışma yer almaktadır. Bu çalışmalarda, işaretlerin uzamsal ve spektral farklılıklarını kullanma, türbinlerin lokasyonunu bildiren transponder uygulaması, menzil-Doppler işleme, adaptif kargaşa haritalama ve radyal hız farklılıklarından yararlanma gibi yöntemler kullanılmıştır. Bununla birlikte, türbin etkisini gidermeye yönelik olan ve işaret işleme anlamında multi-kuadratik interpolasyon veya band geçiren

filtreleme uygulama, radar operasyonu anlamında boşluk doldurma veya doğrudan görüşü giderme veya, türbin görünmezliği anlamında gizleme (stealth) teknolojisi gibi metodlardan yararlanan çalışmalar da mevcuttur. Türbin etkisini hava trafik kontrol (air traffic control, ATC) radarlarında gidermeye yönelik metodlar, ön-tespit aşamasında huzme işleme, tespit aşamasında Doppler tabanlı kargaşa haritalama ve iyileştirilmiş CFAR, tespit sonrası aşamasında ise uyarlamalı iz takip lojiği biçimindedir. Radar bakış açısı, anlık türbin oryantasyonu, yapısal malzeme, yapısal biçim gibi çok sayıda parametreye bağlı ve zamanla değişen yansıtıcılık ve hareket özellikleri sebebiyle, rüzgâr türbinlerinin radar sisteminde tespiti ve giderimi oldukça zor bir problem teşkil etmektedir. Bundan dolayı tespit ve giderim kapsamında yapılan çalışmalar belirli durumlar veya sistemler için özel çözümler sunmakta olup, problemi tam olarak çözmemektedir. Rüzgâr türbini probleminde çözüme yaklaşabilmek için öncelikle problem karakteristiğinin tam olarak ortaya çıkarılması gerekmektedir. Problem karakteristiğini az maliyetli bir biçimde ortaya koyma yollarından bir tanesi sistemler için rüzgâr türbini işaret modelleri geliştirmek ve benzetim ortamında problemi incelemektir. Bu doğrultuda yapılan çalışmalar incelendiğinde, kanatların silindirik yapılar biçiminde modellendiği ve türbin gövdesinin dikkate alınmadığı işaret modeli ile, türbin hareketinin modellenip saçıcılık özelliklerinin dâhil edilmediği işaret modeli karşımıza çıkmaktadır. Türbinlerin saçıcılık özelliklerinin ve saçıcılığa en fazla katkıyı yapan türbin parçası olan kulenin işaret modeline dâhil edilmesi rüzgâr türbini probleminin analizinde önemli yer tutmaktadır.

Radar sistemleri açısından rüzgâr türbinlerinin neden olduğu en ciddi etkilerden bir tanesi sistemin MTT performansında meydana gelen zafiyettir. Sahte hedef izi oluşması, gerçek hedef izinin yanılsaması veya gerçek hedef izlerinin kopması biçimindeki MTT performans zafiyeti özellikle ATC radarlarında büyük önem arz etmektedir. Radar sistemleri için rüzgâr çiftliklerinin MTT performansına yaptığı etkilerin gerçek saha testleri ile ortaya konulduğu çalışmalar literatürde yer almaktadır. Diğer taraftan, problemin net olarak belirlenebilmesi açısından uçuş testlerinin farklı hava şartları için farklı zamanlarda ve çok sayıda yapılması gerekliliği göz önünde bulundurulduğunda bu şekildeki problem incelemesinin oldukça pahalı olacağı açıktır. Bu sebeple, geliştirilen bir iz takip benzetim modeli ile MTT performans değerlendirmesi yapmak hem zaman tasarrufu sağlayacak hem da daha az maliyetli olacaktır.

Rüzgâr türbinlerinin radar sistemlerinde oluşturabildiği bir başka problem yapay açıklıklı radar (SAR) görüntülerindeki bozulmalardır. Bilindiği üzere, SAR sistemleri durağan hedeflerin çapraz-menzil bilgilerini bu hedeflerin bulundukları çapraz-menzille ilişkili olarak oluşturdukları Doppler etkisi sayesinde belirlemektedir. Bu durumda, sabit gövdelerinin yanı sıra, türbinlerin hareketli kanatlarının SAR sisteminde kanat hareketi ile orantılı olarak çok sayıda Doppler bilgisi üretmesi söz konusudur. Bu da, türbinlerin çapraz-menzil doğrultusunda çok sayıda sahte hedef oluşmasına sebebiyet verebilmektedir.

Bu çalışmada, temel olarak, rüzgâr türbinlerinin radar sistemlerinin tespit, hedef izleme ve görüntüleme performansına yapması muhtemel olumsuz etkiler, önerilen bir rüzgâr türbini işaret modeli ve gerçeklenen işaret işleme prosedürleri yardımıyla incelenmiştir. Bu doğrultuda, öncelikle, uzak alan kriterlerinin sağlatılmasına yönelik olarak yeterince düşük boyutlu kanonik segmentlerin süperpozisyonu biçiminde bir türbin modeli ile türbinlerin anlık saçıcılık ve hareket kabiliyetlerini dikkate alan bir

işaret modeli tatılmaktadır. Önerilen modeller yardımıyla, türbinlerin farklı bakış açıları için saçılma karakteristikleri simülasyon ve ayrıca deneysel çalışmalar ile ortaya konulmuştur.

Türbinlerin radar sistemlerinin tespit ve hedef izleme işlemlerine etkisi farklı amaçlara yönelik yaygın olarak kullanılan darbe-Doppler radar (pulse-Doppler radar, PDR) sistemleri için incelenmiştir. Tespit açısından yapılan incelemeler ile türbinlerin tespit karakteristiklerinin çıkarılmasının yanı sıra, yeni bir rüzgâr türbini kargaşa (wind turbine clutter, WTC) modeli oluşturulmuştur. Bununla birlikte, türbin yakınında seyreden gerçek bir hedefin tespit performansının değerlendirilmesi de ayrıca incelenmiştir. Tespit analizi sonuçlarından yararlanarak, rüzgâr türbini etkisinin tespit aşamasında giderilmesine yönelik CLEAN algoritması temelli bir giderim metodu önerilmiştir. Hedef izlemeye olan türbin etkilerinin araştırıldığı analizlerde, çok sayıda senaryo durumu için gerçek bir hedefin radar tarafından izlenme performansı ve meydana gelen zafiyetler belirlenmiştir. Yapılan araştırmalar ve analiz sonuçları baz alınarak, gerçek hedeflere yönelik hedef izlemede zafiyet oluşma olasılığının yüksek olduğu tespit edilmiştir. Bu nedenle, türbin kaynaklı etkiyi minimize edecek yeni bir rüzgâr çiftliği yerleşim tasarımı önerilmiştir. Yeni tasarıma ilişkin benzetim sonuçlarında hedef izleme performansının arttığı gözlemlenmiştir.

SAR sistemlerinde türbin kaynaklı görüntü bozulmaları yine önerilen türbin ve işaret modelleri kullanılarak incelenmiştir. Bozulma etkisinin teorik çıkarımlarına ek olarak simülasyon sonuçları da göstermiştir ki türbinler, çapraz-menzil boyutunda çoklu hedef izi oluşturma veya yüksek yansıtıcı gövdeleri sebebiyle zayıf saçıcı özellikli başka hedeflerin tespit edilememesi gibi problemlere sebep olabilmektedir.

1. INTRODUCTION

Deteriorating effects of wind turbines (WTs) and wind farms (WFs) on detection, tracking and imaging performances of radar systems are investigated in this dissertation. In this scope, a novel WT signal model is introduced initially. Then, signal processing frameworks of pulse-Doppler and synthetic aperture radar (PDR and SAR) systems are implemented in order to examine adverse WT effects. Moreover, approaches about reduction of WT effects on the detection and target tracking operations of PDRs are proposed by utilizing the exhaustive examination outputs.

1.1 Motivation and Problem Statement

In the last decades, WTs have been attracting the attention of a large number of researcher especially from radar community. It is because of their adverse effects on the performance of radar operations that were proven via several studies. WTs are also at the heart of this study, therefore, detailed information about their operational and structural characteristics constitute vital importance. Hence, related topics constituting the problem background are considered throughout this chapter.

1.1.1 Wind turbines

Decrease in petrol sources, energy prices, supply uncertainties, and environmental concerns are driving most of the countries in the world to develop diverse sources of clean and renewable energy. The countries are working toward generating more energy from domestic resources that can be cost-effective and "renewed" without contributing to climate change or major adverse environmental impacts. One of the energy sources that meet those criterias is the wind energy. Therefore, there has been an increasing trend in wind power installations all over the world especially recently. Figure 1.1 annually and cumulatively summarizes the globally installed wind capacity for the years from 1997 to 2014 [1].
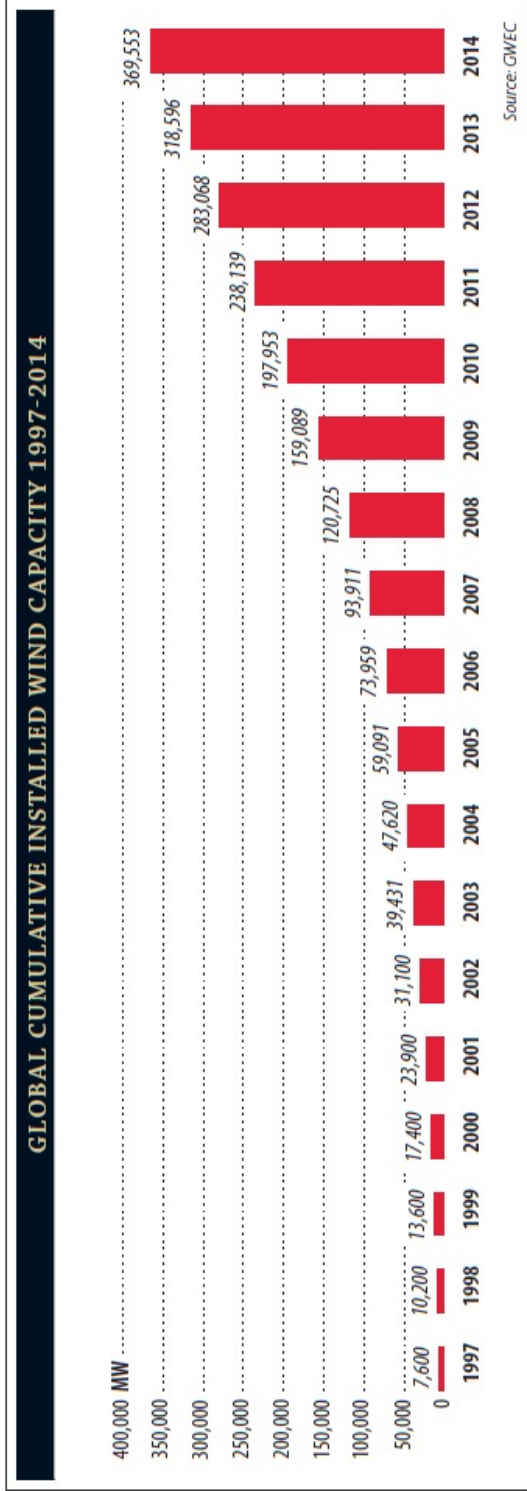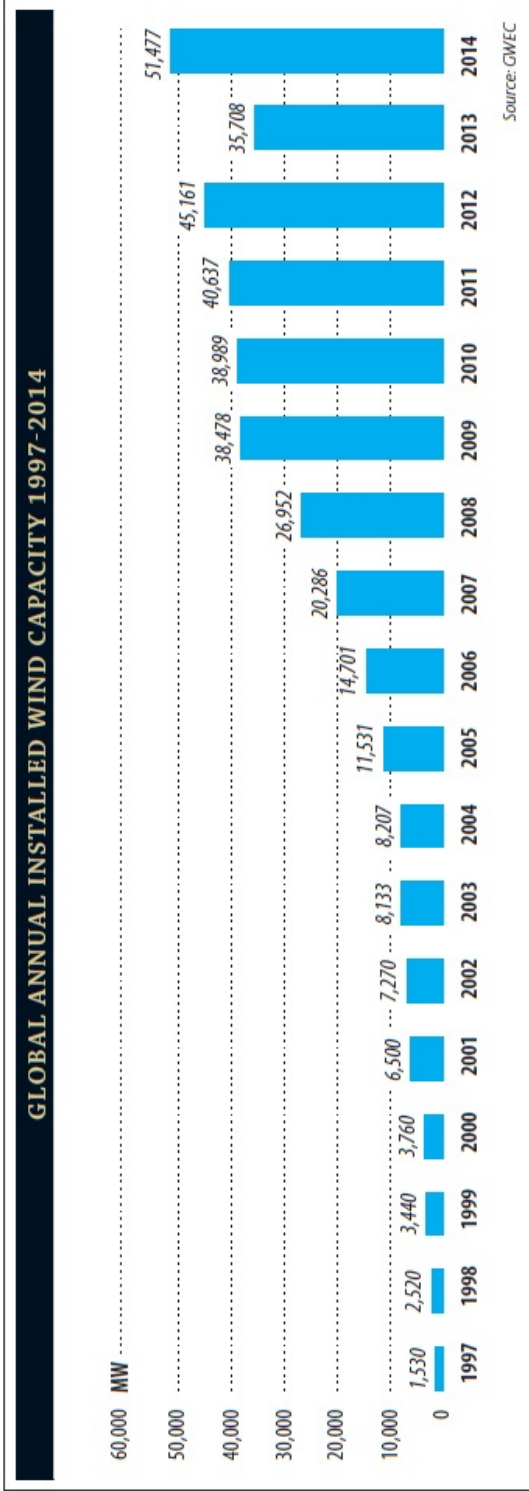
Figure 1.1 : Wind power installation statistics all over the world.

2

Similar to the global statistics, there is also a remarkable increase in the wind power installations in Turkey for the last years. It could be inferred from Figure 1.2 that the recent installations are above 500 megawatt (MW) in average [2].
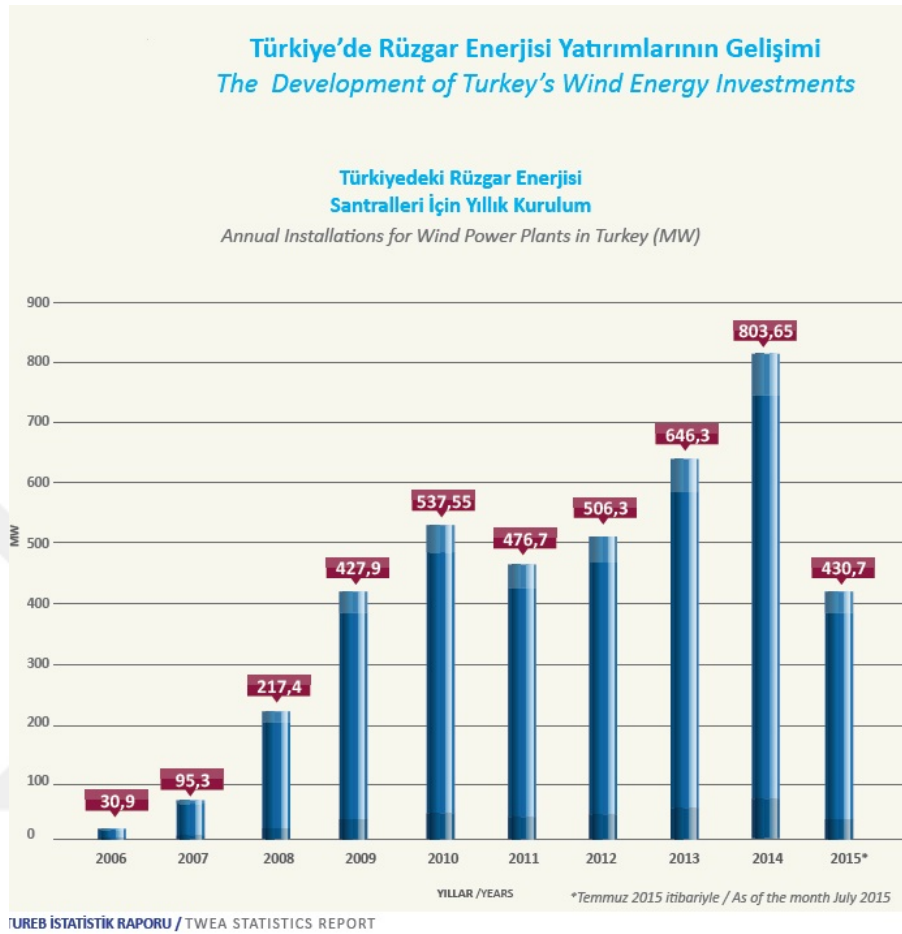
Figure 1.2 : Wind power installation statistics in Turkey.

According to the global and local statistics, the wind power usage is likely to be widespread all around the world. Maybe it will be possible to see WTs everywhere by courtesy of advence in power-efficient wind turbine technology soon.

1.1.1.1 Technical specifications

Wind turbines consist of four main parts which are the blades, nacelle, tower and the base. The blades act much like an airplane wing. When the wind blows, a pocket of low-pressure air forms on the downwind side of the blade. The low-pressure air pocket then pulls the blade toward it, causing the blades (rotor) to turn. This is called lift. The force of the lift is actually much stronger than the wind's force against the front side of the blade, which is called drag. The combination of lift and drag causes the rotor to spin like a propeller [3]. The nacelle houses a generator and a gearbox. The spinning

3

blades are attached to the generator through a series of gears. The gears increase the rotational speed of the blades to the generator speed. As the generator spins, electricity is produced. Those generators can be either variable or fixed speed. Variable speed generators produce electricity at a varying frequency. Fixed speed generators do not need to be corrected, but can not take advantage of fluctuations in wind speed. The tower which is the third component of a WT contains the electrical conduits, supports the nacelle, and provides access to the nacelle for maintenance. Finaly, the base, which is made up of concrete and steel, supports the whole structure.

WT parts those mentioned might vary significantly in terms of appearence and structural characteristics depending upon the types of the WTs. Essentially, horizontal axis wind turbine (HAWT) and vertical axis wind turbine (VAWT) are the commonly employed WT types whose structural componenets are demonstrated in Figure 1.3.
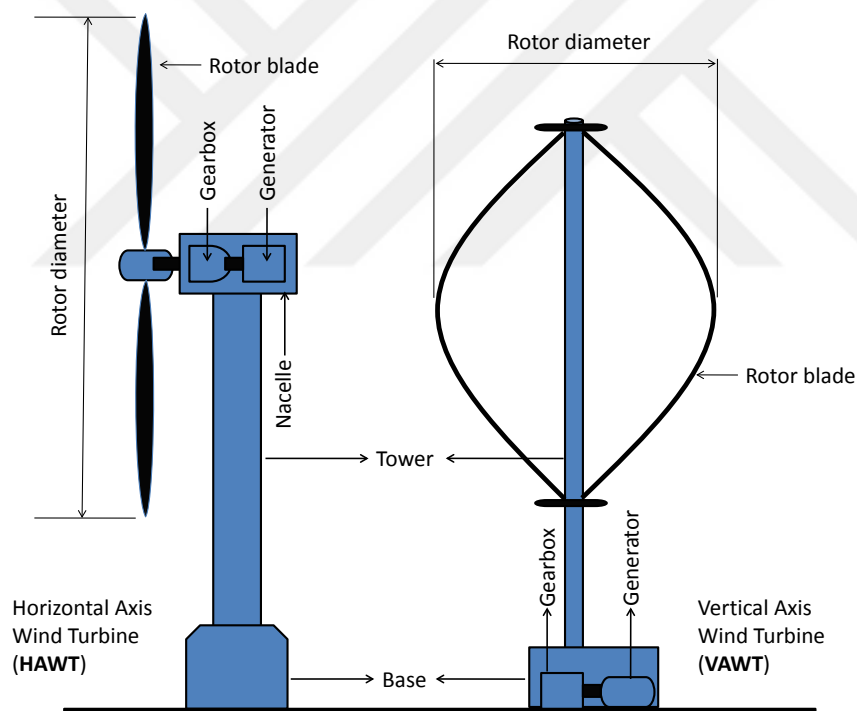
Figure 1.3 : Physical characteristics of HAWT and VAWT type WTs.

The position of blades is the main difference between the VAWT and HAWT type wind turbines. In HAWT, blades are on the top, spinning in the air and are most commonly seen while in VAWT, generator is mounted at the base of the tower and blades are wrapped around a shaft.

There are some advantages of VAWT on HAWT. First of all, the turbine generator and gearbox can be placed lower to the ground making maintenance easier and lower

the construction costs. Moreover, the main advantage of VAWT is that it does not need to be pointed towards the wind to be effective. In other words, they can be used on the sites with high variable wind direction. Since VAWTs are mounted closer to the ground they are more bird friendly and do not destroy the wildlife [4]. Finally, VAWTs are quiet, efficient, economical and perfect for residential energy production, especially in urban environments. Despite these advantages, VAWTs have some significant drawbacks that harden their usability. As the VAWTs are mounted closer to the ground, less wind speed is available to harness which means less production of electricity [4]. VAWTs are very difficult to erect on towers, which means they are installed on base, such as ground or building. Another disadvantage of VAWT is the inefficiency of dragging each blade back through the wind. Due to their structural and motional characteristics, HAWTs could produce by far the higher amount of energy than the VAWTs. Generally, in the case of plentiful energy necessities, HAWTs are preferred while the VAWTs are employed in order to meet local energy requirements such as highway lighting. Typical HAWT and VAWT type wind turbine installations are demonstrated in Figure 1.4 [5], [6].

Wind turbines can be used as stand-alone applications, or they can be connected to a utility power grid or even combined with a photovoltaic (solar cell) system. For utility-scale (megawatt-sized) sources of wind energy, a large number of wind turbines are usually built close together to form a wind plant, referred to as a wind farm. As well as the installations on land, stand-alone or farm based WT installations can be designated on sea which is named as off-shore installation. An exemplary off-shore wind farm installation is depicted in Figure 1.5 [7].

1.1.1.2 Possible effects on radar systems

Beside their significant mission in terms of renewable energy production, it has been properly stated that WTs confront the radar systems with several adverse impacts. The reason for those impacts arises from reflective, structural and motional characteristics of the WTs.

As is well-known that radar systems could detect targets that cause echoes strong enough to exceed radar detection threshold. Strength of a target echoe is actually depending on the scattering level of that target which is represented by radar cross

(a)

(b)

Figure 1.4 : Typical WT installations a) HAWT installation for general purpose electricity production, b) VAWT installation for street lighting.

Figure 1.5 : An exemplary off-shore wind farm installation.

section (RCS) metric. Accordingly, targets with relatively higher RCS have a potential to be detected by radar systems. Additional to the RCS levels, Doppler shift caused by the motion of the targets is an another important metric in radar target detection. Most of radar systems such as air traffic control or air defense ones utilize Doppler shift phenomenon to discriminate moving targets from stationary ones.

In order to satisfy the demands on energy production, wind turbines might have very large sizes. Dimensions of some exemplary wind turbine models in terms of total turbine height are given in Table 1.1 [8].

Table 1.1 : Sample WT sizes.

Model	Manufacturer	Total Height
E44	ENERCON	85 m
N90	NORDEX	124 m
V112	VESTAS	174 m

According to this table, it could be inferred that a wind turbine might be larger than an airplane which is the main target of interest for radar systems.

Due to material properties they consist of and huge dimensions, wind turbines have large reflective surfaces in two areas, the tower and the blades. The tower is obviously stationary and so its RCS is fixed. The RCS of the blades changes dramatically as the blades rotate. This can result in a 'flash' of high RCS as the surface of the blade

becomes perpendicular to the line of sight (LoS) between the radar and the wind turbine. The resulting RCS profile is very similar to that of a hovering helicopter.

With their rotating blades, wind turbines can also mimic moving targets in radar systems. This occurs because of the Doppler shift arised in the returned signal from the rotating portions of wind turbines. In summary, having larger dimensions together with motional and high reflective structural characteristics, wind turbines play a significant role and could cause detrimental effects in radar operation. Some possible effects are summarized here briefly.

Clutter: Unwanted echoes are considered as "clutter", and may reduce the detection capability of a radar system. WTs present large physical targets and therefore a large amount of energy is reflected back towards the radar. Much of the structure is static and therefore the return can be significantly reduced by conventional Doppler processing. However, the reflections can not be suppressed entirely. The blades rotate with large tip speeds and cause a significant Doppler profile that can not be rejected [9].

Range sidelobe effects: Most of radar systems utilize pulse compression and suffer from the appearance of range sidelobes. Returns from large scattering surfaces of wind turbines can leak in through the sidelobes, causing a smearing of the wind turbine return in range [10].

Detection shadowing: Constant False Alarm Rate (CFAR) processing uses a sliding window to provide a varying threshold with range based on the local clutter levels. Since the wind farm appears as a large clutter return, the threshold is raised, reducing radar detection sensitivity around the wind farm. The threshold is also raised around the vicinity of the wind farm due to the CFAR window range extent. This effect, coupled with the range sidelobe effects mentioned above, causes detection shadowing around the wind farm, potentially a few kilometers away [11].

Physical shadowing: Due to having larger physical structures, wind turbines might be responsible for the shadowed regions where the radar systems face degradations on target detection. It is obvious that the tower is the highest contributor part of the WTs for those shadowed regions.

Ghost targets: WT towers produce large specular returns and can create a multi-path environment. It is reported that this can result in false "ghost" targets appearing.

Track creation: The signal processing in any radar system creates a spatial pattern of detections that changes from scan to scan. The track creation algorithm looks at how this pattern evolves between scans to initiate a track on the radar screen. The turbines in a wind farm can create false plots that will scintillate from scan to scan and can therefore create false tracks.

Track seduction and splitting: An aircraft flying over a wind farm can have its own track altered. When the aircraft moves into a region where probability of detection is low, the tracking algorithm may assume that the returns from the wind turbine blades/towers are that of the target. This may result in the position and velocity of the target aircraft being misreported and even the formation of splitting tracks.

Saturation: Marine radars do not include Doppler processing, and interference is primarily due to echoes from WT towers, which present high RCS values at related radar frequencies. Consequently, echoes of small crafts within the wind farm can merge with strong echoes generated by the turbines when the craft pass close to the towers, making them invisible to radar observers or automatic plotting facilities. [12].

Erroneous measurement in weather radars: Doppler weather radars measure the echo strength of the targets together with their radial velocities [11]. The motion of the rotor blades of a WT is interpreted by the radar as the wind speed, leading to erroneous wind estimates.

Image blurring in SAR: Doppler frequency shifts caused by each target determine the cross-range of those targets in SAR systems. WTs with rotating blades have potential to induce wide Doppler spectrum that cause additional target signatures in SAR images. This might suppress the neighboring targets and blur the focused images.

1.2 Literature Review

In spite of the increasing tendency of wind energy throughout the world, several works have theoretically and experimentally exhibited the degrading effects of wind turbines on the performances of electromagnetic radiating systems. Wind farm-based degradations have been shown to vary depending on the structural, reflectivity and motional properties of WTs. The huge dimensions of WTs (e.g., total heights up to 200 m) cause them to constitute as challenging obstacles for radar systems, and result

in shadowed regions in which the radar detection performance severely degrades [13]. Together with the high-reflectivity components they consist of, the rotating blades of WTs cause moving target signatures which arise in the form of false target detections [14], clutter and ghost targets [9], [15] on the radar scope. The electrically-huge and high-reflective characteristics of WTs result in high radar cross section values that produce radar echoes with considerable amplitudes. High-amplitude radar returns related to WTs might, for example, give rise to higher range side-lobe returns from the pulse compression stage of radar systems employing chirp waveforms [10], and to increase in the detection threshold during constant false-alarm rate filtering [16], desensitization of genuine targets (GTs) and the increased missed detection rates related to them because of the domination of WT clutter on the dynamic range provided by the analog-to-digital conversion process [17]. The increasing number of WTs in WFs and the challenges produced by them in radar detection process would also deteriorate the radars' MTT performances. Since the increase in the number of WTs causes moving target signatures, WTs have the potential to trigger several false tracks of static or moving characteristics that would result in degradations on the detection and tracking performances [17], [18]. Besides, it has been known that the radar tracking events related to GTs might be corrupted by the WTs because of the detection misses and incorrect associations with false detections [19]- [20].

The literature includes many works focused on the detection of WTs on radar scopes. Within these works, several approaches such as the usage of spatial [21] and spectral [22] features of received radar signals, the usage of transponders on WTs to indicate their locations [23], range-Doppler processing [24] and adaptive clutter mapping [25] are employed. Additionally, there are examinations that focus on the mitigation of WF effects via different signal processing approaches such as multi-quadratic interpolation [21], [26] or band-pass velocity filtering [22], different radar operations such as gap-filling [9] or blocking the radar line-of-sight to WTs, and WT stealth technology. In [18], the mitigation approaches for WF effects on ATC radars have been listed as beam processing during pre-detection interval, Doppler-based clutter mapping and enhanced CFAR during detection interval, and the adaptive tracking logic during the post-detection interval. Since the reflectivity and kinematic characteristics of WTs are dependent on the radar aspect, time-varying WT orientation, structural material

properties and structure geometries, the investigation of WT detections and mitigation of their effects have been challenging. Previous works on the determination and mitigation of WFs' deteriorations have focused on some specific cases and systems. One should note that, in order to provide an extensive mitigation scheme for WF effects on the radar detection and tracking processes, the whole nature of the WT degradations should be well-investigated. One of the most efficient and low-cost solutions to deal with WT interactions is to model and simulate the radar signal and the WF-scattering phenomenon. When examining the related works performed via the simulation-based approach, it would be possible to see the signal models considering the rotating blades of WTs as cylindrical segments by also disregarding the contribution of WT mast [27], and considering the rotational motion of the WT blades without including the scattering characteristics [28]. The inclusion of the scattering characteristics of masts, which are the components of WTs with the highest scattering contribution in the signal model plays a critical role in WT scattering signal evaluation. The examination provided in [29] has been based on a signal model considering the time-varying scattering characteristics of WT mast and blades that are modeled as the assembly of cylindrical and rectangular segments in order to satisfy the far-field condition.

One of the most crucial types of disturbance that WTs have introduced to radar systems is the degradation on the radar's MTT performance. The deterioration of the MTT performance that might occur in the form of false-target tracking, the seduction and corruption of GTs' tracks, has been reported for ATC radars via the numerous flight-based experiments [19], [20], [30], [31]. The experimental characterization of the WF effects on the MTT performance of radars might be only possible via several flight-based trials made in different weather conditions, time intervals and for different target routes which would be costly and time-consuming. Hence, it would be important to examine the WF effects on the radar MTT performance via employing a tracking simulation model that would provide both time- and cost-efficiency. In literature, there is insufficient examinations for the WF effects on the radar MTT performance using a simulation model. In [32], the MTT performance of marine surveillance radar while tracking a boat in the vicinity of off-shore WTs has been simulated and compared to the results of actual cruise experiments. Within the study in [32], the

scattering characteristics of the boat and WTs have been considered as time- and orientation-invariant. By considering that particularly the scattering characteristics of WTs have sensitivity on the WT orientations and radar aspect, it would be apparent that using uniform and constant RCS values within the simulation model would result in misinterpretation of WF effects and the tracking performance.

In the literature, some of the studies considering the impacts of rotating targets to SAR systems exist [33], [34], however, there is little work dealing with the adverse effects of WTs on SAR imaging. An exemplary work given in [35] examines the deteriorating Doppler effects caused by WTs in SAR images. As can be inferred from that study, WTs with their rotating blades might cause deteriorations in SAR images along the cross-range dimensions. This is actually an expectable situation since the SAR systems evaluates the cross-range position of stationary targets through the Doppler shift that those targets induce. Rotating blades can produce additional Doppler shifts and therefore cause multiple target signatures along the cross-range. On the other hand, it is clear to note that the interfering Doppler contributions would be meaningful when they have sufficiently high amplitude levels. Hence, investigating only the Doppler effects of WTs is not enough to extract all of adverse WT effects in SAR imaging.

1.3 Contributions

In this dissertation, the main focus is on the presentation of detrimental WT effects on detection, tracking and imaging performances of radar systems. In order to achieve the targeted goals, first of all, a novel wind turbine signal model is introduced. By using the proposed signal model and implementing the typical signal processing algorithms, analysis frameworks are designed for pulse-Doppler and synthetic aperture radar systems. With the help of those frameworks:

- Detection characteristics of WTs in PDRs are investigated.

- A novel WTC model is constructed by exploiting WT detection characteristics.

- Adverse effects of WTs on the detection of genuine targets are investigated.

- Adverse effects of WTs and WFs on the multiple target tracking performances of PDRs in terms of GNN and PDA association methods are examined.

- Adverse effects of WTs and WFs on the imaging performances of SARs are investigated.

Additional to the WT impact analyses, two extra efforts are made about the reduction of adverse WT effects on radar performance. One of the efforts deals with subtraction of WT contributions from radar raw data via utilizing CLEAN algorithm. The aim of that operation is to mitigate WT effects at pre-detection stage. On the other hand, the other study intends to increase the multiple target tracking performance in the vicinity WFs. To this end, a novel WF settlement approach is designed in order to reduce degradations on the tracking performance of radar systems.

1.4 Thesis Organisation

The organization of this dissertation is as follows: Chapter 2 provides fundamental information about radar systems. Additionally, raw data generation and signal processing schemes of pulse-Doppler and synthetic aperture radars are given in detail. Chapter 3 introduces a novel canonical wind turbine model which is utilized to form radar raw data for wind turbines. Scattering properties of the wind turbines are also examined by using the proposed model. Detection characteristics of the wind turbines on pulse-Doppler radar systems are investigated in Chapter 4. By making use of those characteristics, a new wind turbine clutter model is proposed. Moreover, degradation in the detection performance of genuine targets in the vicinity of wind turbines are investigated in the case of various tubine aspects. At the end of this chapter, a mitigation approach to reduce wind turbine effect at the pre-detection stage is presented. Chapter 5 is mainly dedicated to analyze deteriorating WF effects on radar systems' multiple target tracking operation. In addition to the analyses for various simulation scenarios, a novel wind farm design approach which aims at decreasing adverse effects of wind farms on genuine targets' tracking performance is introduced. Detrimental wind farm effects on radar imaging performance is studied in Chapter 6. Corruptions at especially cross-range dimension of a SAR images are demonstrated

for both single and multiple turbine cases. Finally, Chapter 7 concludes whole work considered in this dissertation.

2. RADAR FUNDAMENTALS AND SIMULATION BACKGROUND

2.1 Radar Fundamentals

The word radar is an abbreviation for RAdio Detection And Ranging. Generally, radar systems employ modulated waveforms and directive antennas to transmit electromagnetic energy to search for targets. Targets within a search volume reflect portions of this energy back and produce echoes in the radar system. These echoes are then processed by the radar to extract target information such as range, bearing, velocity, and other target identifying characteristics.

Frequency band for radar operation ranges from HF to MMW depending on the operational purposes. Typical air surveillance radars are operated in L and S band while the imaging, target or missile tracker ones use X and Ku bands. Radar operating frequency bands and some typical applications dedicated to those bands are given in Table 2.1.

Table 2.1 : Radar frequency bands and typical applications.

Band	Frequency Range	Typical Applications
HF	3-30 MHz	Over-the-horizon surveillance
P	30-300 MHz	Applied for early radar systems
UHF	300-1000 MHz	Ballistic missile early warning
L	1-2 GHz	Air traffic control, surveillance
S	2-4 GHz	Air traffic control, marine
C	4-8 GHz	Weather, satellite transponder
X	8-12 GHz	Missile guidance, imaging
Ku	12-18 GHz	Imaging, satellite altimetry
K	18-27 GHz	Meteorology missions, speed control
Ka	27-40 GHz	Airport surveillance, photography
MMW	40-110 GHz	Satellite communications, automotive

2.1.1 Radar range equation

One of the fundamental tools for radar systems is the radar range equation which is utilized in system design studies and calculation of some operational metrics such as

the received power, maximum detectable range, achievable signal to noise ratio (SNR), etc. Stepwise derivation of that equation is provided here. First of all, a radar with an omni directional antenna that radiates energy equally in all directions is considered. In this case, peak power density (power per unit area) at any point in space is defined as:

$$P_D = \frac{Peak\ transmitted\ power}{area\ of\ sphere}\ \frac{watts}{m^2}. \tag{2.1}$$

Then, with the assumption of lossless propagation medium, the power density at range R away from the radar becomes

$$P_D = \frac{P_t}{4\pi R^2}, \tag{2.2}$$

where P_t is the peak transmitted power and $4\pi R^2$ is the surface area of a sphere of radius R. This power density is also proportional to the antenna gain G in the illuminated direction, therefore, it gains the form

$$P_D = \frac{P_t G}{4\pi R^2}, \tag{2.3}$$

where, G is the function of antenna effective aperture A_e and the wavelength of the operated electomagnetic signal λ as

$$G = \frac{4\pi A_e}{\lambda^2}. \tag{2.4}$$

Antenna effective apertures are proportional to physical antenna apertures (A) in terms of the antenna aperture efficiency coefficient ρ as in equation 2.5.

$$A_e = \rho A, \quad 0 \le \rho \le 1 \tag{2.5}$$

When the radiated energy impinges on a target, the induced surface currents on that target radiate electromagnetic energy in all directions. The radiation is dependent on the target RCS, σ. RCS is related to the ratio between the power reflected back to radar system to the power density incident on target as provided in equation 2.6.

$$\sigma = \frac{P_r}{P_D}, \ m^2 \tag{2.6}$$

16

Here, P_r is the power arrived at the radar receiver. The radiated electromagnetic energy from the target travels the distance R and arrives at the radar receiver with the power

$$P_r = \frac{P_t G \sigma}{(4\pi R^2)^2} A_e = \frac{P_t G^2 \lambda^2 \sigma}{(4\pi)^3 R^4}. \tag{2.7}$$

Equation 2.7 is the main range equation for radar systems. By using that equation, some special metrics could be derived. For instance, maximum operational range (R_{max}) of a radar system can be expressed by introducing the minimum detectable signal power, S_{min}. With the consideration that S_{min} is the received power related to the maximum operational range, R_{max} is calculated by the formula

$$R_{max} = \left(\frac{P_t G^2 \lambda^2 \sigma}{(4\pi)^3 S_{min}} \right)^{1/4}. \tag{2.8}$$

In practical situations, returned signals received by radars will be corrupted with noise, which introduces unwanted voltages at all radar frequencies. Therefore, the noise is naturally introduced to the radar range equation via the metric noise figure, F. The SNR ratio between the input and output of the radar receiver gives the noise figure as

$$F = \frac{(SNR)_i}{(SNR)_o} = \frac{S_i/N_i}{S_o/N_o}, \tag{2.9}$$

where S_i and S_o denote the power at the input and output of the radar receiver, respectively. Similarly, N_i and N_o are the input and output noise powers. Input noise power can be obtained using the Boltzman's coefficient k, effective noise temperature T_e and the radar bandwidth B_w for a lossless antenna as given in equation 2.10.

$$N_i = k T_e B_w \tag{2.10}$$

In this instance, signal power of the radar receiver can be rewritten in terms of the SNR value at the output of radar receiver through

$$S_i = k T_e B_w F (SNR)_o. \tag{2.11}$$

By using the relation given in equation 2.11, radar range equation is defined in terms of the SNR at the output of the radar receiver. Relatingly, minimum achievable output SNR is as provided in equation 2.12.

$$(SNR)_{o\ min} = \frac{S_{min}}{kT_eB_wF} = \frac{P_tG^2\lambda^2\sigma}{(4\pi)^3kT_eB_wFR_{max}^4} \tag{2.12}$$

In general, radar losses denoted by L reduce the overall SNR, and hence, SNR formulation considering the losses becomes

$$(SNR)_o = \frac{P_tG^2\lambda^2\sigma}{(4\pi)^3kT_eB_wFLR^4}. \tag{2.13}$$

Hereby, we have completed the fundamental expressions about radar range equation with equation 2.13.

2.1.2 Radar cross section

Radar cross section, can be regarded as the measure of the electromagnetic (EM) energy intercepted and reradiated by an object. A more formal definition of the RCS (σ) of an object can be made as the following: "It is the equivalent area intercepting the amount of power that, when scattered isotropically, produces at the radar receiver a power density that is equal to the density scattered by the actual object" [36]. The unit of RCS is square-meters (m^2). This metric is generally used to categorize the objects' EM reflectivity or ability to scatter the EM energy for a particular direction and at a particular frequency.

RCS is the main parameter in detection of targets. The low observable targets are designed to give low RCS values so that it is not easy to detect those targets by radar systems. Special design features for low-observable targets include planar body surfaces that reflect the incoming wave to another direction and special radar absorbing material (RAM)-based coating or painting. Targets are likely to have high RCS features with their metallic surfaces that reflect almost all of the incoming energy, rounded shape design that scatters the EM wave almost in all directions, and canonical shapes and cavities that scatter the incident field in the backward direction. Furthermore, being larger in size also increases the possibility for a target to have higher RCS values [37].

The mathematical expression of RCS can be given in various forms or with different mertics such as electrical fields, magnetic fields, power and so on. As a widespread representation, general formulation of RCS for a target that is at range R away from the radar is given here as provided in equation 2.14

$$\sigma = \lim_{R \to \infty} \left(4\pi R^2 \frac{|E^s|^2}{|E^i|^2} \right), \tag{2.14}$$

where E^i and E^s are the incident and the scattered electrical fields, respectively. Detailed information about RCS calculations could be obtained from [38].

2.1.3 Radar classification

Radar systems can be classified into numerous categories based on the specific radar characteristics, such as the waveforms utilized, frequency band, antenna type, and so on. In terms of their location platform they can be classified as ground based, airborne, spaceborne, or ship based radar systems. Another classification is based on the mission and/or the functionality of the radar. This includes: air traffic control, weather, acquisition and search, tracking, track-while-scan, imaging, fire control, early warning, over the horizon, terrain following, and terrain avoidance radars [39]. Multifunction radars are the phased array radars utilizing phased array antennas. A phased array is a composite antenna formed from two or more basic radiators. Narrow directive beams are synthesized by array antennas and may be steered mechanically or electronically. Electronic steering is achieved by controlling the phase of the electric current feeding the array elements, and thus the name phased array is adopted.

Radars are most often classified by the types of waveforms they employ, or by their operating frequency. Considering the waveforms first, radars can be continuous wave (CW) or pulsed radars [40]. CW radars are those that continuously emit EM energy, and use separate transmit and receive antennas. Unmodulated CW radars can accurately measure target radial velocity (Doppler shift) and angular position. Target range information can not be extracted without utilizing some form of modulation. The primary use of unmodulated CW radars is in target velocity search and track, and in missile guidance. Pulsed radars use a train of pulsed waveforms (mainly with modulation). In this category, radar systems can be classified on the basis of the Pulse

Repetition Frequency (PRF) as low PRF, medium PRF, and high PRF radars. Low PRF radars are primarily used for ranging where target velocity is not of interest. High PRF radars are mainly used to measure target velocity. Continuous wave as well as pulsed radars can measure both target range and radial velocity by utilizing different modulation schemes.

2.1.3.1 Continuous wave radars

A continuous wave radar system with a constant frequency can be used to measure speed. However, it does not provide any range information. A signal at a certain frequency is transmitted via an antenna and then reflected by the target with a certain Doppler frequency shift. This means that the signal's reflection is received on a slightly different frequency. By comparing the transmitted frequency with the received one, speed can be determined. A typical application is radar for monitoring traffic. There are also military applications of CW radar systems.

FMCW radar: The disadvantage of CW radar systems is that they can not measure range due to the lack of a timing reference. However, it is possible to generate a timing reference for measuring the range of objects using what is known as "frequency-modulated continuous wave" (FMCW) radar [41]. This method involves transmitting a signal whose frequency changes periodically. When an echo signal is received, it will have a delay offset like in pulse radar. The range can be determined by comparing the frequency. It is possible to transmit complicated frequency patterns with the periodic repetition occurring at most at a time in which no ambiguous echoes are expected. However, in the simplest case basic ramp or triangular modulation is used, which of course will only have a relatively small unambiguous measurement range.

2.1.3.2 Pulsed radars

In pulsed radar systems, a sequence of modulated or non-modulated pulses are sent periodically and an echoe accumulation process is performed during a time that is dedicated to reception operation. Range information is provided for a target based on the timing difference between the transmitted and received pulses. These systems could be employed in coherent or non-coherent modes of operation. In the case of non-coherent operating mode, phase information is not preserved and therefore it is not possible to determine target radial velocity. The pulse width determines the range

resolution in this type of radar operation. In general, operation of a pulsed radar system is illustrated in Figure 2.1. The pulse repetition interval is the time between transmitted pulses and denoted by *PRI* in the figure, also the pulse-width is presented by τ and Δt is the elapsed time of the signal that is returned from the detected target.
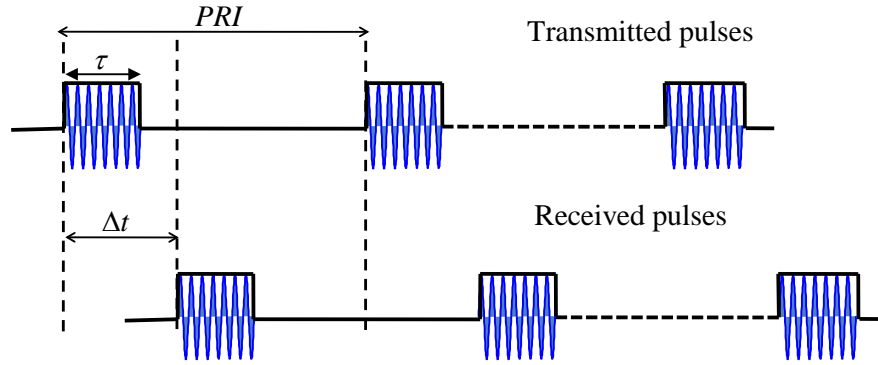
Figure 2.1 : Transmit and receive pulse trains.

The inverse of the *PRI* is the pulse repetition frequency which can be symbolized by *PRF*. There is an inverse relation between those two metrics as $PRF = 1/PRI$. During each *PRI* the radar radiates energy only for τ seconds and listens for target echoes for the rest of the *PRI*. Duration of the pulse is related to radar transmitting duty cycle which is defined as the ratio

$$d_t = \tau/PRI. \qquad (2.15)$$

This yields the average transmitted power to be as provided in equation 2.16.

$$P_{av} = P_t \ x \ d_t \qquad (2.16)$$

The range corresponding to two-way time delay (*PRI*) is known as the radar unambiguous range, R_u, and evaluated through $R_u = cT/2$ where c is the speed of the light. In a similar manner, the range corresponding to any detected target can be calculated by equation 2.17.

$$R = c\Delta t/2 \qquad (2.17)$$

In the case of using simple waveforms as illustrated in Figure 2.1, pulsed radars are subject of a dilemma between range resolution and maximum detectable range. By this

way, an increase in range resolution would decrease the maximum detectable range. Therefore, pulsed radars typically employ pulse compression waveforms one of which is the FMCW in order to achieve high range resolution and longer detection ranges at the same time.

2.2 Simulation Framework for the Implemented Pulse-Doppler Radar System

Pulse-Doppler radars are employed for several military and civilian applications such as reconnaisance, early warning, air surveillance, air traffic control and tracking. Due to having a widespread usage, they have remarkable potential to encounter WT deteriorations. Therefore, we mainly focused on the investigation of degrading WT effects on detection and tracking performances of PDRs. In this scope, simulation background of a typical 2-D PDR is realized initially.

2.2.1 Pulse-Doppler radar basics

A pulse-Doppler radar is a radar system that determines the range to a target using pulse-timing techniques, and uses the Doppler shift of the returned signal to extract targets' radial velocity. It combines the features of pulse and continuous-wave radars, which were formerly separate due to the complexity of the electronics.

Pulse-Doppler techniques find widespread use in meteorological radars, allowing the radar to determine wind speed from the velocity of any precipitation in the air. PDR is also the basis of synthetic aperture radar used in radar astronomy, remote sensing and mapping. In air traffic control, they are used for discriminating aircraft from clutter. Besides the conventional surveillance applications, PDRs have been successfully applied in healthcare, such as fall risk assessment and fall detection, for nursing or clinical purposes.

Simplified block diagram of a PDR is depicted in Figure 2.2. Local oscillator box generates the synchronization timing signals required throughout the system. A modulated signal is generated in waveform generator and sent to the antenna by the transmitter block. Switching the antenna between the transmitting and receiving modes is controlled by the duplexer. The duplexer allows one antenna to be used to both transmit and receive. During transmission it directs the radar electromagnetic energy towards the antenna. Alternatively, on reception, it directs the received radar echoes

to the receiver. The receiver amplifies the radar returns and prepares them for signal processing. Extraction of target information is performed by signal and data processor blocks. Finally, outputs of the processor blocks are sent to the display in order to inform system operators.

This dissertation considers an MTI based PDR system whose operational characteristics and algorithmic structures are detailed throughout this section to investigate the deteriorating WT effects on the detection and tracking performances of radar systems.
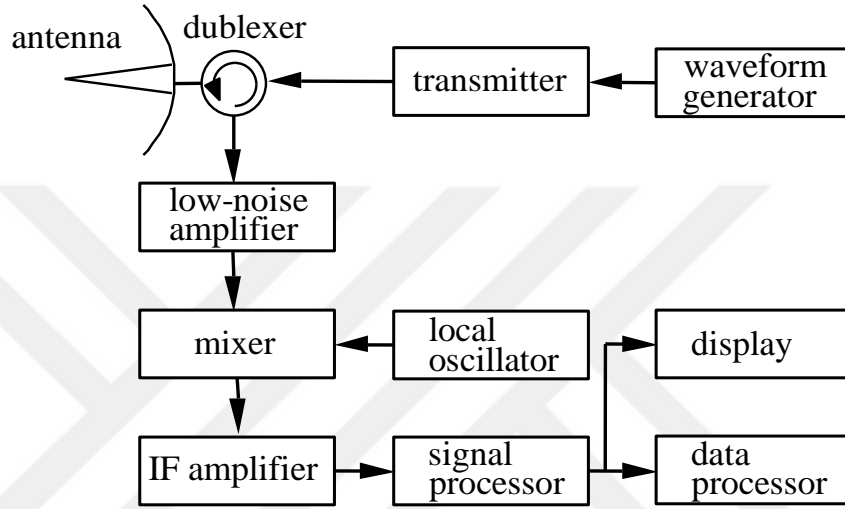
Figure 2.2 : Pulse-Doppler radar blocks.

2.2.1.1 Resolution

Resolution is the spacing (in range, Doppler, angle, etc.) in order to discriminate responses from two scatterers. Range resolution is proportional to the length of the pulse (τ) employed for the case in which simple pulse is used as signal waveform. Consider two point scatterers spaced by ΔR. In this instance, when the distance of the closer one to the radar is R, echoes will arrive radar receiver at times $2R/c$ and $2(R+\Delta R)/c$, respectively. Additionally, first echo ends at time $(2R/c)+\tau$. Echoes will just abut if the relation $(2R/c)+\tau = 2(R+\Delta R)/c$ satisfies. Hence, the range resolution requires the equation

$$\Delta R = c\tau/2. \tag{2.18}$$

On the other hand, when pulse compression waveforms are used as typically, the resolution in range dimension becomes as provided in equation 2.19.

$$\Delta R = c/2B_w \tag{2.19}$$

where B_w denotes bandwidth of the transmitted signal. Resolution for the dimension perpendicular to the radial direction is named as cross-range resolution and denoted by ΔCR. That resolution depends on the horizontal beamwidth of the antenna and varies according to the range from radar system. For the distance R from the radar and 3 dB beamwidth θ_a, cross-range resolution can be expressed as

$$\Delta CR = 2R\sin\left(\frac{\theta_a}{2}\right) \approx R\theta_a. \tag{2.20}$$

It can be extracted from the equation that the finer cross-range resolution gets worser proportional to the increase in the distance to the radar system.

2.2.1.2 Doppler effect

Radars utilize Doppler frequency shift to extract target radial velocity (range rate), as well as to distinguish between moving and stationary targets or objects such as clutter. The Doppler phenomenon describes the shift in the center frequency of an incident waveform due to the target motion with respect to the source of radiation. Depending on the direction of the target's motion, this frequency shift may be positive or negative. A waveform incident on a target has equiphase wavefronts separated by λ, the wavelength. A closing target will cause the reflected equiphase wavefronts to get closer to each other. Alternatively, a receding target (moving away from the radar) will cause the reflected equiphase wavefronts to expand (larger wavelength).

Mathematical derivation of the Doppler shift can be presented with the consideration of a monostatic radar transmitting at frequency f_t and a target moving towards the radar with radial velocity v ("closing" target). Special relativity predicts the received frequency (f_r) to be

$$f_r = \left(\frac{1+v/c}{1-v/c}\right)f_t. \tag{2.21}$$

Here, v/c is always accepted small due to the comparison of target's speed to the speed of the light. By expanding denominator in binomial series with first three term, f_r becomes

24

$$f_r = \left[1 + 2\left(v/c\right) + 2\left(v/c\right)^2\right] f_t. \tag{2.22}$$

Also, quadratic and higher-order terms of (v/c) can be discarded as in equation 2.23.

$$f_r = \left[1 + 2\left(v/c\right)\right] f_t \tag{2.23}$$

Finally, Doppler shift is the change in frequency as provided

$$f_d = f_r - f_t + \frac{2v}{c} f_t = +\frac{2v}{\lambda_t}. \tag{2.24}$$

As indicated in equation 2.24, moving targets cause Doppler shifts proportional to their radial velocities in the radar systems. Therefore, by performing spectral examinations over the target returns, it is possible to detect moving targets.

2.2.2 Simulation framework

Signal processing blocks for the implemented MTI-based pulse-Doppler radar system is demonstrated in Figure 2.3. The simulation concept seen in the figure consists of three main units; raw data generation, detection processing and multiple target tracking. Those processing units are introduced in detail throughout following subsections.
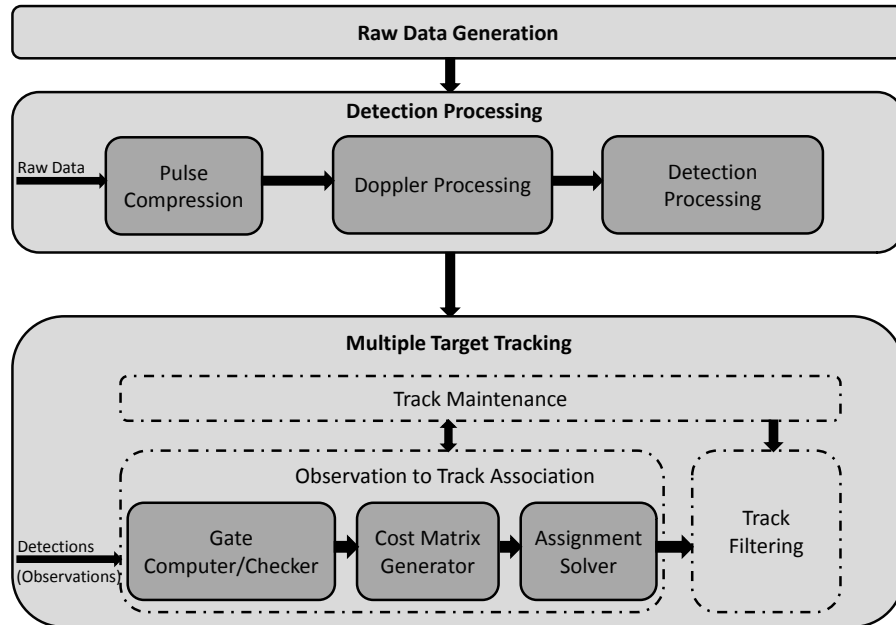
Figure 2.3 : PDR signal processing blocks.

2.2.2.1 Signal waveform and raw data generation

PDR systems typically take the advantage of pulse compression waveforms in order to meet the necessities about higher range resolution and longer detection distances. Mostly, linear frequency modulation (LFM or chirp) type waveform whose analytical expression is provided in equation 2.25 is employed for those considerations.

$$s_t(t) = rect\left[\frac{t}{T_p}\right] \exp(j2\pi(f_0 t + K\frac{t^2}{2})), -\frac{T_p}{2} < t < \frac{T_p}{2} \qquad (2.25)$$

Here, $rect\left[\frac{t}{T_p}\right]$ denotes the unit-amplitude rectangular pulse with the duration of T_p seconds, K is the chirp rate and f_0 is the center frequency of the signal. In Figure 2.4, real part of an exemplary LFM waveform is depicted.
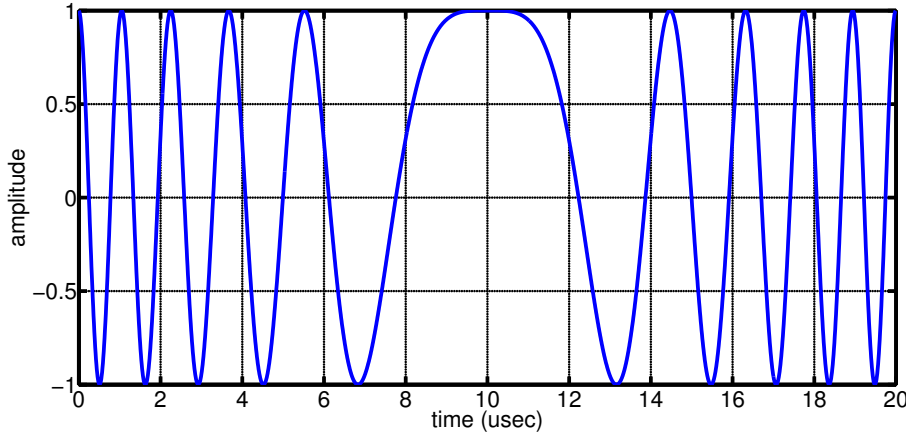
Figure 2.4 : Real part of an exemplary LFM signal.

When the radar illuminates an azimuthal sector, scaled and time-shifted versions of the transmitted waveform are reflected back to radar receiver from all scatterers residing on the illuminated sector. Thus, for each transmitted pulse in a coherent processing interval (CPI), fast-time series of radar raw data will be a cumulation of echoes from all contributing scattereres as

$$s_r(t) = \sum_{i=1}^{M} \sqrt{P_i} \exp(j2\pi(f_0(t - \frac{2R_i}{c}) + K\frac{(t - \frac{2R_i}{c})^2}{2})), \qquad (2.26)$$

where M is the total number of scatterers, P_i and R_i are the received power and distance (w.r.t. the radar) of ith scatterer. As can be inferred from the formula, amplitude and phase for a scatterer contribution is determined by scatterer's echoe power and radial distance, respectively. Note that, for the sake of simplicity and without the loss

of generality, we have used the flat Earth approximation for the computation of the distances. Moreover, in the scope of this study, as a scatterer-specific metric, RCS is used in case of received power when specifying the amplitude of instantaneous scatterer contributions. Therefore, equation 2.26 is transformed into the form as

$$s_r(t) = \sum_{i=1}^{M} \sqrt{\sigma_i} \exp(j2\pi(f_0(t - \frac{2R_i}{c}) + K\frac{(t - \frac{2R_i}{c})^2}{2})). \qquad (2.27)$$

In equation 2.27, σ_i presents the RCS value of the ith scatterer. Final radar raw data for a CPI is constructed in a matrix form via combination of received fast-time echoes for each pulse transmission instants. So, the raw data matrix will be constructed through:

$$s_r(p,t) = \sum_{i=1}^{M} \sqrt{\sigma_{p,i}} \exp(j2\pi(f_0(t - \frac{2R_{p,i}}{c}) + K\frac{(t - \frac{2R_{p,i}}{c})^2}{2})), \qquad (2.28)$$

where p denotes the pulse transmission instant (slow-time index) and takes the value from 1 to total transmitted pulse P.

2.2.2.2 Pulse compression

As an initial step throughout signal processing stages, pulse compression is performed in order to increase the signal to noise ratio of received data and achieve desired range resolution. The process is carried out on the fast time dimension of the constructed radar raw data.

Matched filters are employed to accomplish pulse compression operation with the consideration of maximizing SNR. Theoretical approach behind the construction of those filters could be demonstrated via some mathematical derivations. Initially, under the white noise interference assumption, the spectrum of the output signal $y(t)$ of a system in the case of input signal $x(t)$ and receiver frequency response $h(t)$ becomes

$$Y(\Omega) = H(\Omega)X(\Omega). \qquad (2.29)$$

Here, Ω denotes the continuous frequency, $Y(\Omega)$, $X(\Omega)$ and $H(\Omega)$ are representative for the spectrum of output, input and receiver filter, respectively. The aim of designing a matched filter is to find a $H(\Omega)$ that maximizes SNR at a particular time instant, say T_P. By utilizing Parseval's theorem, the power of the output signal can be rewritten as

$$|y(T_P)|^2 = \left| \frac{1}{2\pi} \int_{-\infty}^{\infty} X(\Omega) H(\Omega) e^{j\Omega T_P} d\Omega \right|^2 . \tag{2.30}$$

Moreover, noise power spectral density (PSD) is a white noise spectrum with density $N_0/2$, so the PSD at receiver output gains the form

$$N(\Omega) = \frac{N_0}{2} |H(\Omega)|^2 , \tag{2.31}$$

and total noise power for the receiver output at any time becomes

$$n_p = \frac{1}{2\pi} \frac{N_0}{2} \int_{-\infty}^{\infty} |H(\Omega)|^2 d\Omega . \tag{2.32}$$

Now, SNR observed at time T_P can be calculated by the ratio between the signal and the noise power expressions as

$$\chi = \frac{|y(T_P)|^2}{n_p} = \frac{\left| \frac{1}{2\pi} \int_{-\infty}^{\infty} X(\Omega) H(\Omega) e^{j\Omega T_P} d\Omega \right|^2}{\frac{N_0}{4\pi} \int_{-\infty}^{\infty} |H(\Omega)|^2 d\Omega} . \tag{2.33}$$

With the help of Schwarz Inequality, the equation above could be solved to find the maximizing $H(\Omega)$ as provided in equation 2.34.

$$H(\Omega) = \alpha X^*(\Omega) e^{-j\Omega T_P} \tag{2.34}$$

where α is the scale factor. Time domain version of that equation which holds for the impulse response is

$$h(t) = \alpha x^*(T_P - t) . \tag{2.35}$$

It could be extracted from the equation that the impulse response is the same shape, just phase conjugated and time reversed version of the input signal waveform. The scale factor is unimportant and T_P should be grater than the duration of input signal in order to satisfy causality conditions.

The mission and advantage of pulse compression is demonstrated with a sample simulation scenario in which there are four moving targets in the illuminated sector of the radar system. The targets are assumed to be 2.2 km, 3.8 km, 4.1 km and 4.4 km far from the radar. Fast-time series representation of such a scenario for single pulse case is given in Figure 2.5a. In the figure, it is obvious that the SNR is extremely low and it could be quite difficult or maybe impossible to discriminate those targets from clutter. On the other hand, SNR is seen to be significantly increased and the target echoes became visible after the matched-filter operation as depicted in Figure 2.5b. Note that the sample scenario is also used for the exemplary demonstrations about some of following processing stages such as Doppler processing or non-coherent pulse integration.
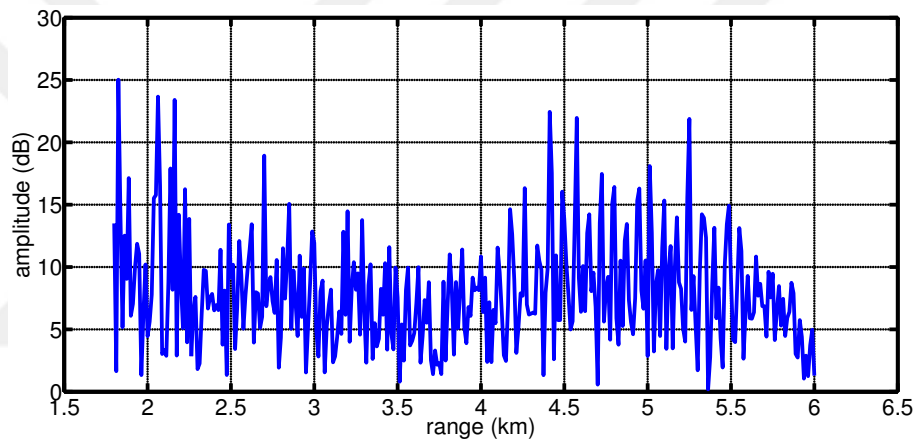
(a)
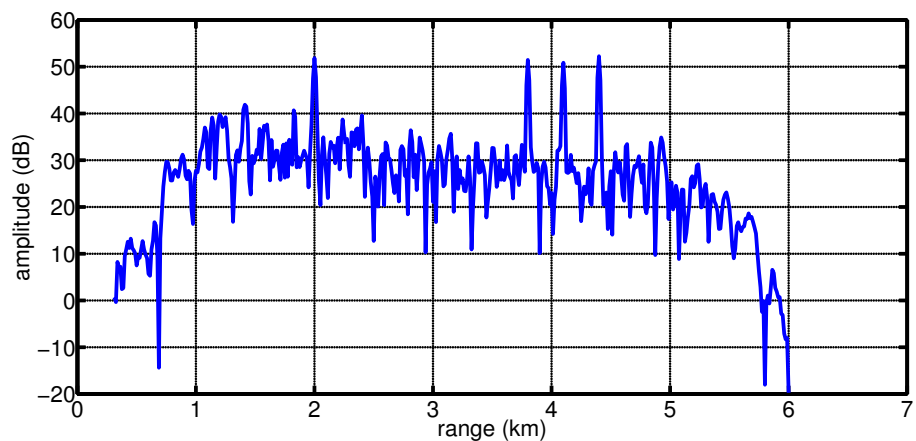
(b)

Figure 2.5 : Range profile representation of the sample scenario a) without pulse comression, b) with pulse comression.

Pulse compression process also makes the return echoes compressed and localized in range dimension. This can be extracted from Figure 2.6 by comparing range-Doppler

domain illustrations of radar raw data one of which is the pulse-compressed version while the other one is not.

(a)

(b)
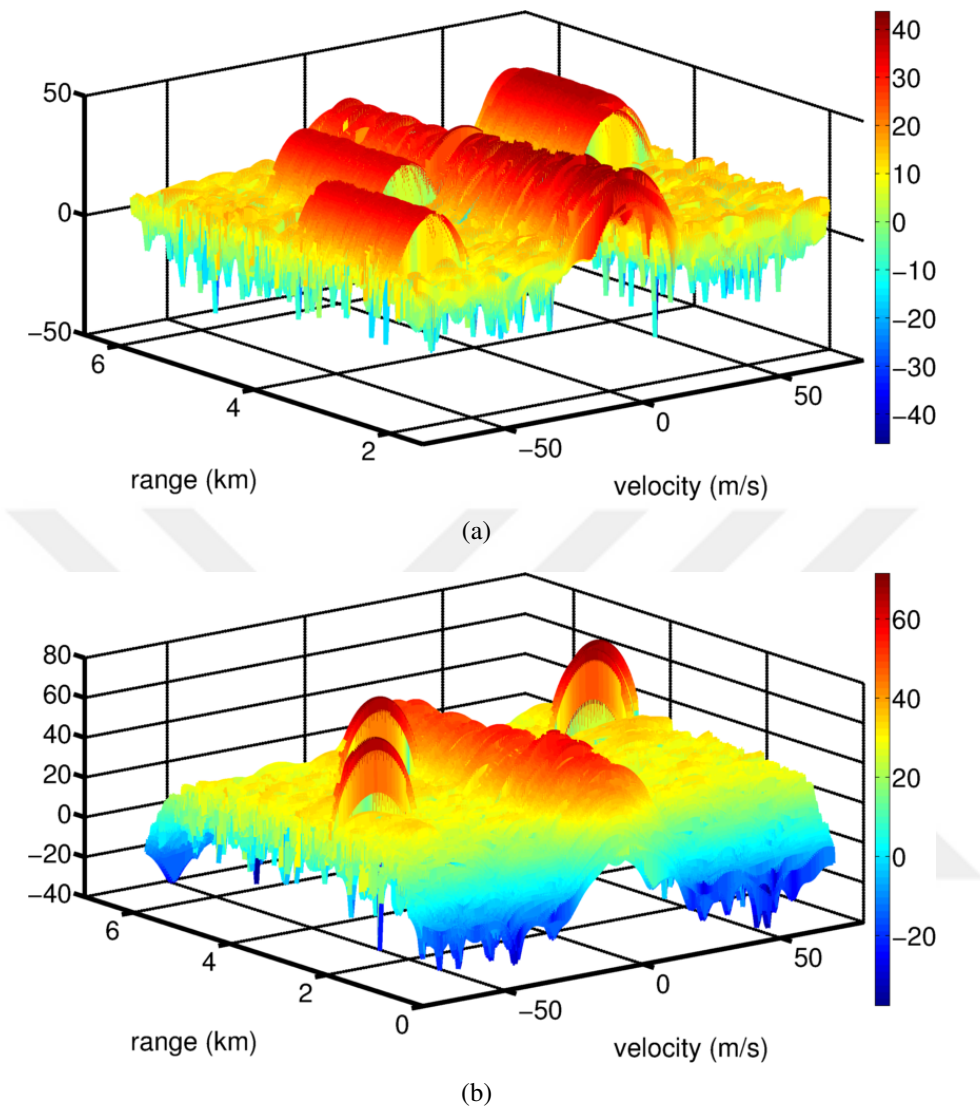
Figure 2.6 : Range-Doppler domain representation of the sample scenario: a) without pulse comression, b) with pulse comression.

2.2.2.3 Doppler processing

Doppler processing performs on slow time samples for each range bin and, provides discrimination and detection of moving targets. In the scope of this dissertation, an MTI-based Doppler processing scheme which is exactly equivalent to the MTI filtering followed by Fourier transform operation is employed.

For the case in which stationary scatterers are located over radar-illuminated area, slow time echoe samples for those scatterers are expected to be almost same. On the other hand, moving targets will induce some change to the phase of the echoes according

to their radial velocities. The change in the phase creates Doppler shift and makes possible the detection of moving targets.

In MTI-based processing frameworks, MTI filters are employed to cancel out stationary or slowly-moving targets or clutter as an initial stage of Doppler processing. That operation is accomplished mostly by using pulse-canceller filters. Those filters can be constructed as two-pulse cancellers (first-order forms) as the simplest case or more complex structures. PDR simulation framework in this study considers a three-pulse canceller that is formed via cascading two first-order forms. In Figure 2.7, spectral behaviour of a three-pulse canceller is depicted. As indicated in figure, pulse-canceller structures perform as low-pass filter and cancel out the frequency regions of zero-Doppler and neighborhood.
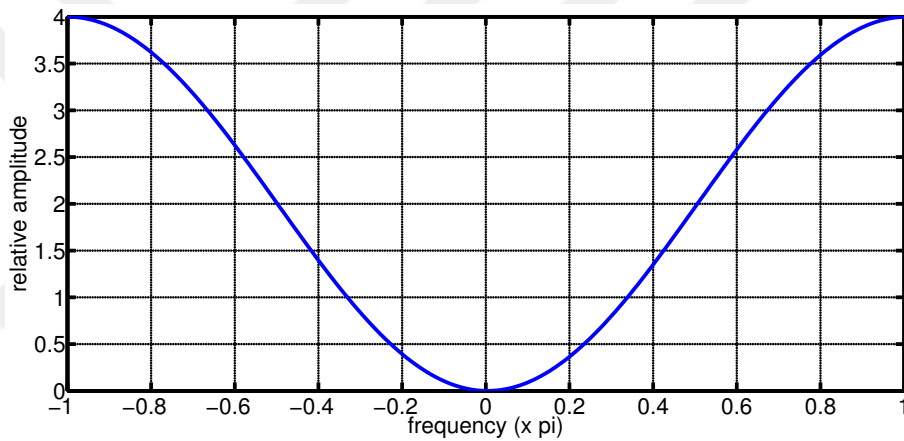
Figure 2.7 : Spectrum of three-pulse canceller.

Following the MTI filtering operation, Fourier transformation is applied to radar data on slow-time extent for each range bin. Hereby, spectral components of moving targets are specified. Following that operation, Doppler-processed data is passed to detection processing stage to determine the spectral components that are strong enough to exceed the detection threshold. Exemplary Doppler processing result for the sample scenario is demonstrated in Figure 2.8. It is clearly seen from the figure that, signal levels of four moving targets became dominant on range-Doppler space after Doppler processing operation.

2.2.2.4 Detection processing

Detection is one of the most significant steps of the PDR processing scheme. This procedure determines whether a target is present at a specific range bin
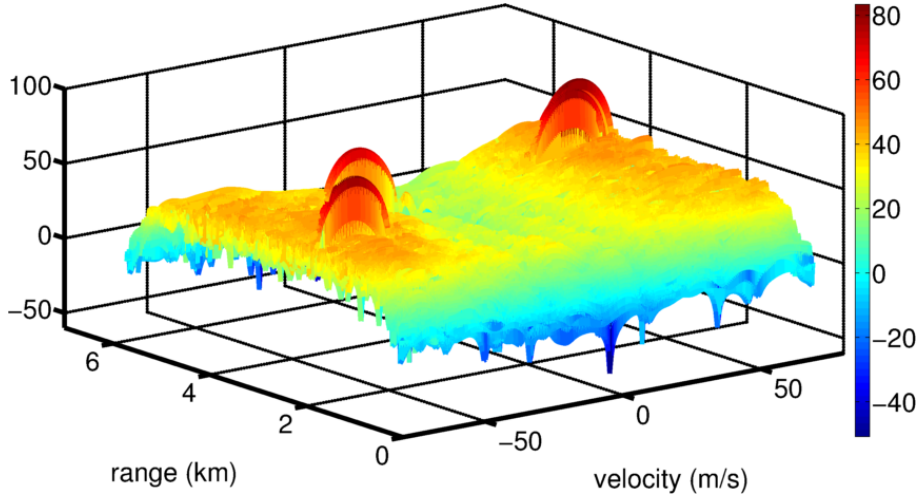
Figure 2.8 : Doppler processing result of the sample simulation scenario.

or not. Depending on the radar system essentials, various detector structures and detection rules might be employed for this operation. In this study, with the consideration of square law detector, detection procedure is completed via employing non-coherent integration followed by cell-averaging constant false alarm rate thresholding (CA-CFAR). Figure 2.9 demonstrates the general structure of employed square law-based detector concept.
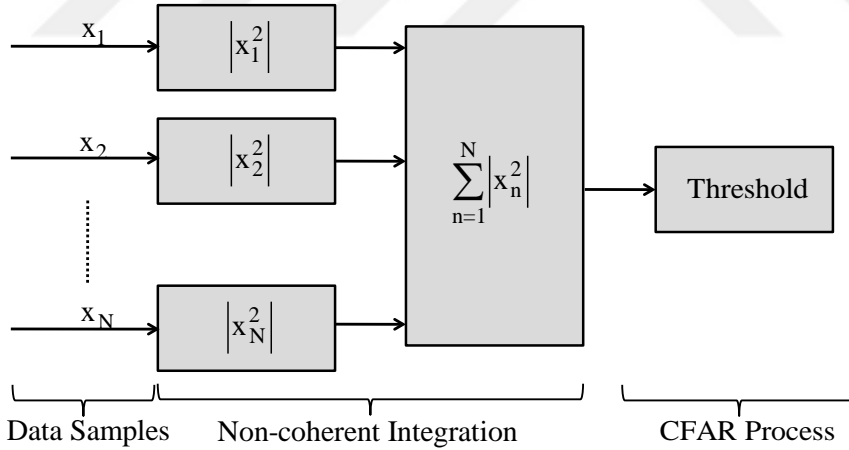
Figure 2.9 : Square law-based detector concept.

When a target is located within the radar beam during a single scan it may reflect several pulses. Radar sensitivity (in terms of SNR) can be increased by integrating all those echoes. The number of returned pulses to integrate depends on the antenna scan rate and the radar PRF as provided in equation 2.36

$$n_p = \frac{\theta_a T PRF}{2\pi} = \frac{\theta_a PRF}{\dot{\theta}_{scan}}, \tag{2.36}$$

32

where $\dot{\theta}_{scan}$ is the antenna scan rate in degrees per second, θ_a is the antenna azimuthal beamwidth and T is the radar scan-time.

The process of adding radar returns is called radar pulse integration. This process can be performed coherently or non-coherently. Coherent integration (CI) preserves the phase relationship between the received pulses while the other one not. Non-coherent integration (NCI) is often implemented after the envelope detector, also known as the quadratic detector. NCI is less efficient than CI and the gain in this type of integration is always smaller than the number of non-coherently integrated pulses. Acquired SNR by using NCI in the detection process as in this study can be expressed as

$$(SNR)_{NCI} = \frac{n_p (SNR)_1}{L_{NCI}} = n_p (SNR)_1 \frac{(SNR)_1}{1 + (SNR)_1}, \qquad (2.37)$$

where

$$(SNR)_1 = \frac{(SNR)_{NCI}}{2n_p} + \sqrt{\frac{(SNR)_{NCI}^2}{4n_p^2} + \frac{(SNR)_{NCI}}{n_p}}. \qquad (2.38)$$

Through the equations 2.37 and 2.38, $(SNR)_{NCI}$ denotes the SNR after NCI operation, $(SNR)_1$ represents the SNR achieved without pulse integration and L_{NCI} is the integration loss. Marcum and Swerling showed that this loss is somewhere between $\sqrt{n_p}$ and n_p [39].

Non-coherent integration results related to the sample simulation scenario is presented in Figure 2.10. It could be clearly observed from the figure that the pulse integration increases the detectability of targets in the vicinity of clutter.
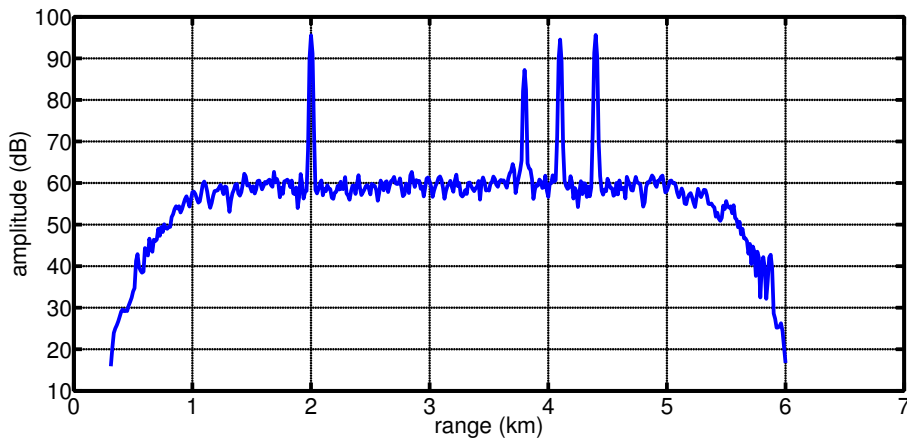
Figure 2.10 : Non-coherent integration result of the sample simulation scenario.

Next to the non-coherent pulse integration, CA-CFAR thresholding is applied to the integrated data to end detection process. The goal of CA-CFAR is to adaptively estimate a detection threshold for each resolution cell while maintaining a constant false alarm rate, P_{FA}. The detection threshold is evaluated by using the average interference power (β^2) of interfering cells (reference cells) neighbor to the cell under test (CUT). 1-D form of a CA-CFAR structure is demonstrated in Figure 2.11. Guard cells shown in the figure are excluded from evaluation of average interference with the consideration about the leakage of the target signal under test to those cells. The margin which is employed to regulate false alarms in detecton process is denoted by α in the figure.
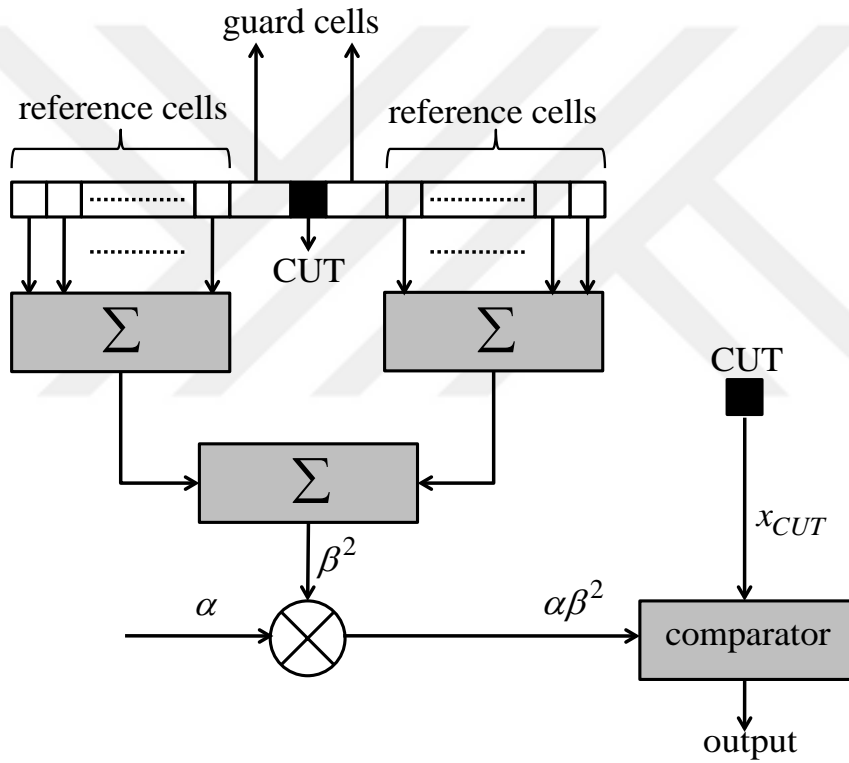
Figure 2.11 : 1-D CA-CFAR structure.

Under the assumption of square law detector and white Gaussian noise (WGN) interference, square-law detected interference will be exponentially distributed. Moreover, when the interference is i.i.d. in the I and Q signals with power $\beta^2/2$ in each (for a total power of β^2), then the pdf of an interference-only sample in cell x_i becomes

$$p_{x_i}(x_i) = \frac{1}{\beta^2} e^{-x_i/\beta^2}. \tag{2.39}$$

34

Then the joint pdf of N neighbouring samples which are considered to be i.i.d. with x_i has the form as provided in equation 2.40.

$$p_{\mathbf{x}}(\mathbf{x}) = \frac{1}{\beta^{2N}} \prod_{i=1}^{N} e^{-x_i/\beta^2} \equiv \Lambda \tag{2.40}$$

Maximum likelihood estimate of the interference β^2 could be evaluated via maximizing the log likelihood form of the joint pdf. This will be resulted as given in equation 2.41.

$$\widehat{\beta^2} = \frac{1}{N} \sum_{i=1}^{N} x_i \tag{2.41}$$

Final form of the detection threshold is commonly evaluated by multiplying the average interference with some multiplier (margin) in order to provide constant false alarm rate as:

$$\hat{T} = \alpha \widehat{\beta^2}. \tag{2.42}$$

Here, the multiplier α is the function of the amount of neighboring cells N and the P_{FA} in the case of square law detector and Gaussian interference.

$$\alpha = N \left((P_{FA})^{-1/N} - 1 \right) \tag{2.43}$$

When designing the detector structures in radar systems, the multiplier factor is generally specified according to the clutter characteristics that the radar is subject of together with the tolerable false alarm rates.

2.2.2.5 Multiple target tracking

In multiple target tracking (MTT) unit of the simulation framework, detections (or incoming observations) are received from the detection processing unit and used to accomplish entire MTT operations. Related operations such as initiation, continuation, termination and maintenance of tracks are handled throughout MTT operational blocks: Observation to Track Association (OTA), Track Filtering (TF) and Track Maintenance (TM).

Implemented MTT scheme considers the logic-based initiation procedure [42]. Moreover, primitive form of tracks are initiated with the detections occurred for the first time and not associated to any existing tracks. With an association to an observation in the following radar-scan, primitive tracks turns into tentative ones. Similarly, a confirmed track is constituted in the case of a successful association event for a tentative track. Association process is accomplished by coarse and fine correlation operations (i.e., gating and assignment procedures, respectively) in OTA block. Additionally, propagation and update processes of the tracks are handled using the well-known Kalman filters within the TF stage. Confirmed tracks are deleted in the case of association failure for three consecutive radar scans. In the TM block of the MTT unit, operations such as resource management of track files are considered.

Multiple target tracking is applied by using standard Kalman filter aided by an association algorithm in this study. Global nearest neighbor (GNN) and probabilistic data association (PDA) filters are the realized association methods which are extensively employed in radar systems.

Track filtering basics

Kalman filter is a set of mathematical equations that provides an efficient computational (recursive) means to estimate the state of a process, in a way that minimizes the mean of the squared estimation error. The filter is very powerful in several aspects: it supports estimations of past, present, and even future states, and it can do so even when the precise nature of the modeled system is unknown. The Kalman filter also has an ability to control noisy systems.

Kalman filters assume that the dynamic model of the considered system is known priorly. Therefore, system dynamics about the MTT operation are introduced here. First of all, this study considers the targets to move according to constant-velocity (CV) motion model [43]. However, the signal model and the related evaluations have taken the 3-D kinematics of WTs and geniune targets (GTs) into account, the detection and tracking signatures are mapped onto xy-plane due to the considered 2-D radar operation. Hence, target state vector includes range (or distance) and range rate (or velocity) values for *x* and *y* axes at time instant *k* as

$$\mathbf{x}_k = \begin{bmatrix} x & \dot{x} & y & \dot{y} \end{bmatrix}_k. \tag{2.44}$$

With the consideration of CV motion model, update process of the target state would be defined by a linear difference equation as provided in equation 2.45.

$$\mathbf{x}_{k+1} = \Phi \mathbf{x}_k + \mathbf{w}_k \tag{2.45}$$

where $\mathbf{x}_{k+1}$ is the target state at time instant $k+1$, Φ is the state transition matrix, and $\mathbf{w}_k$ is the system process noise. The state transition matrix is set consistent to 2-D radar operation and the employed motion model as in [44]:

$$\Phi = \begin{bmatrix} 1 & T & 0 & 0 \\ 0 & 1 & 0 & 0 \\ 0 & 0 & 1 & T \\ 0 & 0 & 0 & 1 \end{bmatrix}. \tag{2.46}$$

Here, T denotes the radar scan-time. The process noise which is assumed to be caused by target acceleration is modeled as zero-mean white noise process with the covariance matrix $\mathbf{Q}$ [44]:

$$\mathbf{Q} = \begin{bmatrix} \frac{T^4}{4}q_x & \frac{T^3}{2}q_x & 0 & 0 \\ \frac{T^3}{2}q_x & T^2 q_x & 0 & 0 \\ 0 & 0 & \frac{T^4}{4}q_y & \frac{T^3}{2}q_y \\ 0 & 0 & \frac{T^3}{2}q_y & T^2 q_y \end{bmatrix}, \tag{2.47}$$

where q_x and q_y are acceleration variances in x and y axes. The measurement state $\mathbf{z}_k$ in the system dynamic model is defined to be constructed from target state by utilizing the measurement matrix $\mathbf{H}$ and the measurement noise $\mathbf{v}_k$ as given in equation 2.48.

$$\mathbf{z}_k = \mathbf{H}\mathbf{x}_k + \mathbf{v}_k \tag{2.48}$$

Similar to the process noise, $\mathbf{v}_k$ is assumed to be zero-mean white noise process with the covariance matrix $\mathbf{R}$. The measurement and the measurement noise covariance matrices are given in equations 2.49 and 2.50, respectively.

$$\mathbf{H} = \begin{bmatrix} 1 & 0 & 0 & 0 \\ 0 & 0 & 1 & 0 \end{bmatrix} \tag{2.49}$$

$$\mathbf{R} = \begin{bmatrix} \sigma_x^2 & 0 \\ 0 & \sigma_y^2 \end{bmatrix} \tag{2.50}$$

In equation 2.50, σ_x and σ_y are the standard deviation of the measurement errors in x and y axes, respectively.

Kalman filters combine the information about state predictions and measurements in order to obtain a proper estimate of the track state. The predictions are performed in terms of apriory estimation of the state ($\mathbf{x}_k^-$) and the error covariance ($\mathbf{P}_k^-$) as:

$$\widehat{\mathbf{x}}_k^- = \Phi \widehat{\mathbf{x}}_{k-1}, \tag{2.51}$$

and

$$\mathbf{P}_k^- = \Phi \mathbf{P}_{k-1} \Phi^T + \mathbf{Q}. \tag{2.52}$$

Before completing the estimation about a posteriori state of the track, a decision on a measurement $\mathbf{z}_k$ should be made by using an association procedure. Besides, Kalman gain ($\mathbf{K}$) is calculated to balance the contributions of predicted apriory estimates and the measurements on final a posteriori state estimate. This gain is related to the error covariance through

$$\mathbf{K}_k = \mathbf{P}_k^- \mathbf{H}^T \left(\mathbf{H} \mathbf{P}_k^- \mathbf{H}^T + \mathbf{R} \right)^{-1}. \tag{2.53}$$

Here, $\left(\mathbf{H} \mathbf{P}_k^- \mathbf{H}^T + \mathbf{R} \right)$ represents the innovation covariance ($\mathbf{S}_k$) which is used for gating operation in measurement association process. Finally, a posteriori estimate of a track state is calculated via

$$\widehat{\mathbf{x}}_k = \widehat{\mathbf{x}}_k^- + \mathbf{K}_k (\mathbf{z}_k - \mathbf{H} \widehat{\mathbf{x}}_k^-), \tag{2.54}$$

where $(\mathbf{z}_k - \mathbf{H} \widehat{\mathbf{x}}_k^-)$ is called as innovation which is a special metric in Kalman filtering. Additional to the a posteriori state, a posteriori error covariance is also updated to be used for following iterations as

$$\mathbf{P}_k = (1 - \mathbf{K}_k \mathbf{H}) \mathbf{P}_k^-. \tag{2.55}$$

Measurement validation

Prior to the association process, valid measurements for each track are specified through a gating operation. When designing validation gates, measurements for each track are assumed to be distributed according to a Gaussian, centered at the measurement prediction ($\hat{\mathbf{z}}_k = \mathbf{H}\hat{\mathbf{x}}_k^-$) and with innovation covariance $\mathbf{S}_k$ as described in equation 2.56.

$$p(\mathbf{z}_k) = N(\mathbf{z}_k; \hat{\mathbf{z}}_k, \mathbf{S}_k) \tag{2.56}$$

Under the assumption of that distribution, the validation gate for a track at time k ($\mathbf{V}_k$) is defined using a threshold Υ for the Mahalanobis distance between predicted and observed measurements:

$$\mathbf{V}_k = \left\{ \mathbf{z} : (\mathbf{z} - \hat{\mathbf{z}}_k)^T \mathbf{S}_k^{-1} (\mathbf{z} - \hat{\mathbf{z}}_k) < \Upsilon_k \right\} = \left\{ \mathbf{z} : d^2(\mathbf{z}, \hat{\mathbf{z}}_k) < \Upsilon_k \right\}. \tag{2.57}$$

The specified threshold allows to quantify how likely measurements of a track are to fall within the validation gate. When gating operations for all tracks are completed, an observation-to-track association matrix $\mathbf{C}$ is constructed using all of tracks and measurements that fall in the validation gates of the related tracks. This association matrix is generally specified in a form as given in equation 2.58

$$\mathbf{C} = \begin{pmatrix} c_{11} & \cdots & c_{1N} \\ \vdots & \ddots & \vdots \\ c_{M1} & \cdots & c_{MN} \end{pmatrix}, \tag{2.58}$$

where rows and columns stand for the observations and tracks, respectively. For the association matrix, M denotes total amount of observation and similarly N represents the quantity of established tracks. The elements of the matrix $\mathbf{C}$ are named as association coefficients and determined according to the gating operation. Therefore, when the observation i is out of the validation gate for the track j, related association coefficient c_{ij} will be set to zero, otherwise, it will be stated as Mahalanobis distance between the observation and the predicted measurement value of the related track, d_{ij}^2. Constructed association matrix is passed to the Assignment Solver sub-unit to accomplish association process.

GNN based association process

The goal of GNN algorithm is to perform data association jointly and find the global optimum. It solves the assignment problem which is set through association matrix and, assigns one and only one measurement to a single track. The assignment problem is set as

$$\arg\min_{\mathbf{X}} \sum d_{ij}^2 x_{ij}, \tag{2.59}$$

where $x_{ij} \in \{0,1\}$ and $\sum_i x_{ij} = \sum_j x_{ij} = 1$. This assignment problem is proposed to be solved by using Hungarian or Munkres [45] algorithms for square and rectangular association matrice cases, respectively. At the end of the optimization process, tracks are allowed to associate with at most one measurement.

PDA based association

Contrary to the association through GNN procedure, PDA makes possible a track to associate with more than one measurement. Weighted combinations of measurements that fall in the validation gate of a track are utilized to determine associative measurement. Due to the association via multiple measurements, weighted combinations of innovations are considered when estimating the a posteriori track state. If we assume there are L measurements falling into the validation gate of a track at time k, individual innovations will be in the form:

$$\mathbf{v}_{k,i} = \mathbf{z}_{k,i} - \mathbf{H}\hat{\mathbf{x}}_k^-, i = 1, 2, ..., L. \tag{2.60}$$

Then the combined innovation is evaluated using the individual ones and weighting factors ($p_{k,i}$) as

$$\mathbf{v}_k = \sum_{i=1}^{L} p_{k,i} \mathbf{v}_{k,i}. \tag{2.61}$$

Here, the weighting factors are the conditional probabilities and calculated using Poisson clutter model with the formula:

$$p_{k,i} = \frac{e_i}{b + \sum\limits_{j=1}^{L} e_j}, i = 1, 2, ..., L \qquad (2.62)$$

$$p_{k,i} = \frac{b}{b + \sum\limits_{j=1}^{L} e_j}, i = 0. \qquad (2.63)$$

In the equations 2.62 and 2.63, $e_i = \exp(-0.5\mathbf{v}_{k,i}^T \mathbf{S}_k^{-1} \mathbf{v}_{k,i})$ and $b = \lambda \sqrt{|2\pi \mathbf{S}_k|} \frac{1 - P_D}{P_D}$ are the error terms, λ is false alarm probability and lastly P_D denotes the detection probability. Here, $i = 0$ holds for the case that there are no measurements falling into the validation gate.

PDA procedure evaluates the a posteriori state and error covariance metrics of a track in a different way than the GNN. By considering the combination of innovations, estimated track state will be in the form of

$$\widehat{\mathbf{x}}_k = \widehat{\mathbf{x}}_k^- + \mathbf{K}_k \mathbf{v}_k, \qquad (2.64)$$

while the updated version of error covariance is calculated through

$$\mathbf{P}_k = p_{k,0}\mathbf{P}_k^- + (1 - p_{k,0})\mathbf{P}_k^c + \mathbf{P}_k^s, \qquad (2.65)$$

where $\mathbf{P}_k^c$ is the covariance update with correct measurement and $\mathbf{P}_k^s$ is the spread of innovations. The mathematical expressions for those two covariance contributions are provided in the following equations.

$$\mathbf{P}_k^c = \mathbf{P}_k^- - \mathbf{K}_k \mathbf{S}_k \mathbf{K}_k^T \qquad (2.66)$$

$$\mathbf{P}_k^s = \mathbf{K}_k \left(\sum_{j=1}^{L} p_{k,j} \mathbf{v}_{k,j} \mathbf{v}_{k,j}^T - \mathbf{v}_k \mathbf{v}_k^T \right) \mathbf{K}_k^T. \qquad (2.67)$$

Special mathematical derivations about PDA association procedure are completed with those equations given above.

Throughout the simulations dealing with the adverse WF effects on PDRs' tracking operation, performances of the two association methods mentioned are investigated.

2.3 Simulation Framework for the Implemented Synthetic Aperture Radar System

2.3.1 Synthetic aperture radar

Synthetic aperture radar is a high-resolution remote sensing technique for imaging remote targets on a terrain or more generally on a scene. In 1951, it was realized that if the echo signal is collected when the radar is moving along a straight path, the Doppler spectrum of the received signal can be used to synthesize a much longer aperture, so that very close targets in the along-track dimension (cross-range) can be resolved [46]. The first SAR image was obtained by a C-46 aircraft through mapping a section of Key West, Florida in 1953 [47], [48]. In 1978, the first on-board satellite SAR system was developed by the National Aeronautics and Space Administration (NASA) researchers and put on Seasat. After Seasat, several satellites carrying SAR systems have been launched by different countries. Russian Almaz (1987), European ERS-1 (1991) and ERS-2 (1995), and Canadian Radarsat (1995) were among some of them. The first space-shuttle mission that has a SAR module was shuttle imaging radar A (SIR-A). After SIR-A was launched aboard the space shuttle Columbia in 1981, other spaceborne SAR missions were followed. SIR-B (1984) and spaceborne imaging radar-C/X-band synthetic aperture radar SIR-C/X-SAR (1994) acquired SAR images in multiple frequencies and polarizations for more advanced applications such as interferometric and polarimetric mapping of terrains [37]. Although SAR has been primarily utilized for surveillance applications such as detection of buildings, airplanes, and tanks, it has also found many real-world applications ranging from geophysics to archeology.

The modes of SAR operation can be divided into three according to the radar antenna's scanning operation. As illustrated in Figure 2.12, when the radar collects the electromagnetic reflectivity of the region alongside which it travels, observing a strip of a terrain parallel to the flight path, this mode is called side-looking SAR or strip-map SAR. When the radar tracks and focuses its illumination to a fixed, particular area of interest, this mode is named spotlight SAR. Another mode of SAR operation is called scan SAR, which is especially used when the radar is flying at high altitude and to obtain a swath wider than the ambiguous range [49]. This enhancement in
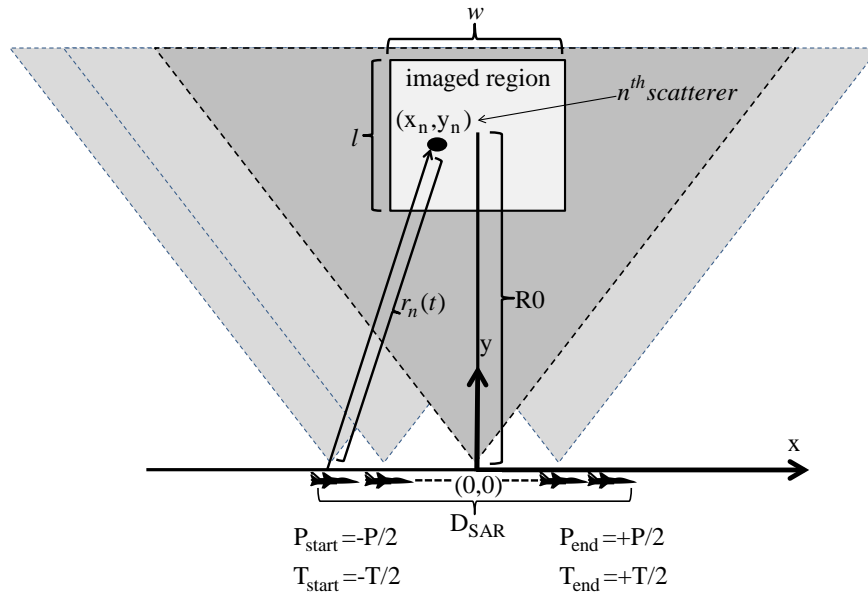
Figure 2.12 : SAR imaging geometry.

swath costs degradation in range resolution. For this mode, the illumination area is divided into several segments, and each segment is assigned to the observation of a different swath. As the radar platform moves, radar illuminates one segment for a time period and then switches to illuminate another one. This switching is accomplished in a methodology such that the desired swath width is covered and no empty segment is left as the platform progresses on its track.

Note that the geometry demonstrated in Figure 2.12 is used in the derivation of SAR signal and calculating SAR specific metrics.

2.3.1.1 SAR resolution

SAR systems provide images with high resolution especially in the cross-range dimension which is its superiority among radar systems. Similar to most of pulsed radar systems, range resolution (ΔR) in SAR images are proportional to the operated signal bandwidth B_w as provided in equation 2.68.

$$\Delta R = c/2B_w \tag{2.68}$$

Extremely high cross-range resolution (ΔCR) can be achieved in SAR systems thank to their operational properties. By synthesizing longer apertures, resolutions in cross-range dimension could be possible on the order of a few centimeters.

Mathematical expression of the cross-range resolution for a target at range R can be expressed as

$$\Delta CR = R\lambda/2D_{SAR}. \tag{2.69}$$

Here, D_{SAR} denotes the length of synthetic aperture and λ stands for the signal wavelength. Additionally, resolution in cross-range is limited by physical antenna size on azimuthal dimension (D_{az}) and has a lower bound as $\Delta CR = D_{az}/2$.

2.3.1.2 SAR signal basics

In this section, derivation and analysis of the SAR signal is presented only for the cross-range dimension. Signal characteristics and processing through range dimension such as pulse compression is similar to those in typical PDRs. Derivation for the SAR signal may be started by taking into account a CW transmit signal with the operational frequency f_c as

$$s_T(t) = \exp(j2\pi f_c t). \tag{2.70}$$

With the consideration of the geometry in Figure 2.12, the signal returned from the nth scatterer located at (x_n, y_n) in 2-D Cartesian coordinates becomes

$$s_{nRF}(t) = \frac{\sqrt{P_{Sn}}}{r_n^2(t)} s_T(t - 2r_n(t)/c) = \frac{\sqrt{P_{Sn}}}{r_n^2(t)} \exp(j2\pi f_c(t - 2r_n(t)/c)), \tag{2.71}$$

where $r_n(t) = \sqrt{y_n^2 + (x_n - d(t))^2}$ and $d(t)$ is the position of the aircraft on x axis at some time t. Additionally, P_{Sn} is the received power (normalized) from the nth scatterer on the imaged area. It is determined from the radar range equation without the R^4 term. If we assume that the aircraft is flying at a constant velocity of $V\,(m/s)$ and $t = 0$ occurs at $x = 0$, we get

$$d(t) = Vt. \tag{2.72}$$

We assume that the total time for the aircraft to travel a distance of P is T and that the aircraft starts at $-P/2$ when $t = -T/2$. Therefore, total distance that the platform travels is

$$P = VT. \tag{2.73}$$

We note that the area to be imaged has a cross-range width of w and a down range length of l. The region is centered in cross-range at $x = 0$ and in down-range at $y = R_0$. If we assume that w, l and P are small relative to R_0, we can replace $r_n^2(t)$ in the denominator of equation 2.71 by R_0^2 and write

$$s_{nRF}(t) = \frac{\sqrt{P_{Sn}}}{R_0^2(t)} \exp(j2\pi f_c t) \exp(-j4\pi r_n(t)/\lambda). \tag{2.74}$$

Since the information needed to form the SAR image is in the second exponential term we will eliminate the first exponential by heterodyning (which is done in the actual radar). We also eliminate the R_0^2 through normalization to yield the baseband signal as

$$s_n(t) = R_0^2 \exp(-j2\pi f_c t) s_{nRF}(t) = \sqrt{P_{Sn}} \exp(-j4\pi r_n(t)/\lambda). \tag{2.75}$$

If we have N_s scatterers in the region imaged, the resulting baseband signal would be

$$s(t) = \sum_{n=1}^{N_s} s_n(t) = \sum_{n=1}^{N_s} \sqrt{P_{Sn}} \exp(-j4\pi r_n(t)/\lambda). \tag{2.76}$$

The equation given in 2.76 indicates that the baseband SAR signal is a combination of phase histories of the scatterers weighted by their scattering properties.

Examination of the phase of the SAR Signal:

Since the information we seek is in the phase of $s_n(t)$, we should examine it in detail. Actually, time-varying range ($r_n(t)$) is the significant portion of the signal phase considered that cause Doppler shift effect to result in focused cross-range information. By exploiting Euclidean distance specifications, time-varying range between the SAR platform and the scatterer can be expressed as provided in equation 2.77.

$$r_n(t) = \sqrt{y_n^2 + x_n^2 - 2x_n Vt + V^2 t^2} = \sqrt{r_n^2 - 2x_n Vt + V^2 t^2} = r_n \sqrt{1 - 2x_n Vt/r_n^2 + (Vt/r_n)^2}$$

$$\tag{2.77}$$

We note that $r_n \approx R_0$, $x_n \ll R_0$ and $Vt \ll R_0, \forall Vt \in [-P/2, P/2]$. In this case, the second and third terms of the last square root in equation 2.77 are assumed to be small relative to 1. This, in turn, allows us to write the expression as

$$r_n(t) \approx r_n(1 - x_n Vt/r_n^2 + \frac{1}{2}(Vt/r_n)^2) = r_n - x_n Vt/r_n + \frac{1}{2}V^2 t^2/r_n. \quad (2.78)$$

If we substitute this into equation 2.75 we get,

$$s_n(t) = \sqrt{P_{Sn}} \exp(-j4\pi r_n/\lambda) \exp(j4\pi(x_n V/\lambda r_n)t) \exp(-j2\pi(V^2/\lambda r_n)t^2). \quad (2.79)$$

Here, it is clear to see that the phase of the baseband SAR signal is constituted of three exponential terms.

Linear Phase, or Constant Frequency Term:

The first exponential in equation 2.79 is a phase caused by range delay to the scatterer that we must live with. The second term is a linear phase term or a term that we associate with frequency. In fact, the Doppler frequency represented by this term is

$$f_{xn} = 2x_n V/\lambda r_n. \quad (2.80)$$

This tells us that $s_n(t)$ has a constant frequency term that depends upon the scatterer cross range position, x_n. f_{xn} also depends upon the aircraft velocity, V, and the radar wavelength, λ. However both of these are known (and fixed). Finally, the related frequence term depends on r_n. With the assumption that all of the scatterers are at the same $y_n = R_0$ (which we can do since we are only concerned with the cross-range problem in SAR imaging here) and considering $x_n \ll R_0$ we could express the range of a scatterer as

$$r_n = \sqrt{y_n^2 + x_n^2} \approx R_0. \quad (2.81)$$

Now, it is possible to write the equation that describes the relation between the induced Doppler frequency and cross-range for a imaged target as

$$x_n = \frac{\lambda f_{xn} R_0}{2V}.\tag{2.82}$$

Consequently, this discussion tells us that, if we can determine f_{xn} through spectral examinations, we can also construct the cross-range information.

Quadratic Phase, or LFM Term:

The third exponential in equation 2.79 is a quadratic phase, or linear frequency modulation term and might cause deteriorations in SAR imaging. Quadratic phase contribution is in the form of

$$\phi_Q(t) = -2\pi\left(\frac{V^2}{\lambda r_n}\right)t^2.\tag{2.83}$$

With the previous assumption that $r_n \approx R_0$, $\phi_Q(t)$ is approximately the same for all scatterers. This means that we can remove it by a mixing or heterodyning process. If we do this we will be left with only the magnitude, constant phase term and the x_n-dependent frequency term. This is sufficient condition to come up with focused images.

Other Considerations:

Some critical constraints should be satisfied when designing a SAR imaging simulator. Constraints about range or slant range dimension such as swath length (l) are determined similar to the procedure applied in PDRs. Unlike those systems, swath width (w), PRI and PRF are related to each other and should be clearly stated in SAR systems. With the consideration of swath width initially, an ambiguity region can be defined where all of scatterers are in the region imaged reside as

$$x_{amb} - x_n = \pm\frac{\lambda R_0}{2V}\frac{1}{PRI}.\tag{2.84}$$

In this equation, $\frac{1}{PRI}$ stands for the Doppler bandwidth. Additionally, it can be inferred from the equation that, we must choose a PRI value such that all scatterers lie within $\pm 1/2$ ambiguity. Therefore, by employing a proper PRI, x_n will satisfy

$$x_n \leq \frac{1}{2}\frac{\lambda R_0}{2V}\frac{1}{T}.\tag{2.85}$$

Since all scatterers of interest lie within the imaged area, equation 2.85 could be rewritten in terms of the swath width as provided in equation 2.86.

$$w \leq \frac{\lambda R_0}{2V} \frac{1}{T} \tag{2.86}$$

In fact, in practical applications we usually choose the PRI such that

$$w \ll \frac{\lambda R_0}{2V} \frac{1}{T} \tag{2.87}$$

so as to be sure that the SAR antenna beam adequately attenuates targets outside of the imaged region. After forming larger images by using a larger effective w, truncation operation is applied to get only the region of interest.

There are two main constraints about the operated PRF one of which can be derived from the equation 2.86 utilizing the relation between PRI and PRF. With the substitution of $PRF = 1/PRI$ relation to that equation, PRF constraint becomes

$$PRF \geq w \frac{2V}{\lambda R_0}. \tag{2.88}$$

A second constraint on the PRF is related to platform velocity and the antenna length on azimuthal dimension (D_{az}) as

$$PRF \geq \frac{2V}{D_{az}}. \tag{2.89}$$

Hereby, fundamental derivations about SAR signal is completed. With the consideration of those fundamentals, a simulation framework for SAR imaging whose details are given in the following subsection is prepared and used to investigate WF effects on SAR imaging.

2.3.2 SAR simulation framework

In this dissertation, a SAR simulation setup which regards the stripmap mode of SAR operation is prepared. The geometry for this type of operation is demonstrated in Figure 2.12. Similar to the procedure performed for PDRs, SAR raw data related to each platform position is formed with the collection of scaled and time-shifted versions

of the transmitted pulse-compression waveform as given (2.27). Amplitude and phase information of the collected signal contributions are evaluated by instantaneously calculating the RCS and distance of all scatterers residing on the imaged area. When generating raw data matrix, considerations for SAR imaging such as limitations about aperture time and PRF which are mentioned in the previous section are naturally taken into account.

There are a variety of stripmap SAR image formation algorithms such as range-Doppler, chirp scaling, range migration, Doppler beam sharpening, etc [41]. They typically differ from each other in terms of computational complexity, resolution capability and so on. In order to process the constructed SAR raw data, Doppler beam sharpening (DBS) algorithm is employed due to its simplicity. It is the original form of SAR imaging and the simplest among SAR processing algorithms. It uses a constant aperture time for all ranges, so that the cross-range resolution is proportional to the range. DBS algorithm is mostly suitable for relatively coarse resolution imagery.

There are three main operational blocks in DBS procedure as depicted in Figure 2.13.
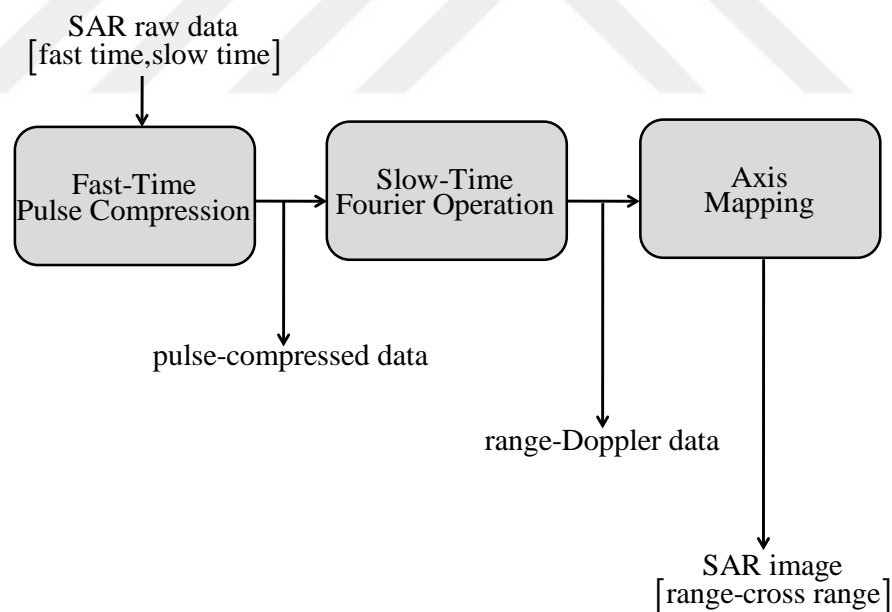
Figure 2.13 : Doppler beam sharpening algorithm flow.

Initially, pulse compression is applied to the SAR raw data throughout fast-time dimension conventionally. This operation is accomplished as described in Section 2. It is pointed out by equation 2.82 that point targets cause Doppler frequency related to their cross-range position. Therefore, a spectrum analysis is required along slow-time dimension to extract targets' cross-range information. This is achieved in the

second operational block via Fourier operation for each range bin. Final focused SAR images are constructed by axis mapping in the third processing block. The mapping process converts range-Doppler data matrix $S[l, F_D]$ to range-cross range image $S[R, x]$ via transforming the parameters l and F to R and x, respectively. The transformation is performed by the equations (2.90) and (2.91).

$$R = R_0 + cT_s l/2 \tag{2.90}$$

$$x = -\lambda R F_D/2V \tag{2.91}$$

In (2.90), T_s denotes sampling time for fast-time dimension. Moreover, F_D denotes Doppler frequency component in (2.91).

3. WIND TURBINE SIGNAL MODELLING APPROACH AND SCATTERING CHARACTERISTICS

WT signal modeling has much significance in determining deteriorating WT effects. It provides dealing with the problem under consideration in an efficient and low-cost way. When examining the related literature, it would be possible to see the signal models considering the rotating blades of WTs as cylindrical segments by also disregarding the contribution of WT mast [27], and considering the rotational motion of the WT blades without including the scattering characteristics [28]. The inclusion of scattering characteristics of masts, which are the components of WTs with the highest scattering contribution in the signal model plays a critical role in WT scattering signal evaluation. With this deliberation, a signal model considering the time-varying scattering properties of WT mast and blades are modeled as the assembly of cylindrical and rectangular segments in order to satisfy the far-field conditions [29]. In this chapter, proposed signal model which constitues a base about WT effect analyses for PDR and SAR systems is introduced in detail.

3.1 Wind Turbine Signal Modeling Approach

By examining the signal waveform employed, it is clear to see that the evaluation of a scatterer's instantaneous signal contribution requires two calculations one of which is it's RCS and the other one is the distance to radar system. Those calculations determine the amplitude and the phase. When the scatterer is a WT, distance calculations could be performed similar to the ones for any target or scatterer. On the other hand, calculation of a WT's RCS has some difficulties due to electrically large dimensions together with the consideration about far-field conditions. RCS calculations can be performed via computational methods. However, especially at UHF bands and above, dimensions of a modern WT might be electrically large. Thus, computational requirements of these methods such as method of moments (MoM) dramatically increase [50]. To overcome this, high-frequency techniques such as Physical Optics (PO) or Geometrical Optics (GO) can be used to compute RCS of a WT [51]. Even if these techniques work well

51

for a stationary WT, they are relatively time consuming and computationally expensive since they need three dimensional (3D) computer-aided design models which must be modified for every broadside angle and rotation instance of the blades. Consequently, a scattering procedure based on an analytical method would be more suitable for the RCS calculation of an electrically large WT since it would be faster than any numerical approaches, it needs very low computer resources, works at different broadside angles of WT without making extra modification on model, easily determines the effects of blade rotation and could be expanded to model WFs [8]. Accordingly, a WT is modeled as a composition of plate- and cylinder-shaped perfectly electrical conducting (PEC) canonical segments which are considered as point scatterers in order to satisfy far-field conditions. The proposed model is demonstrated in Figure 3.1. This model does not contain nacelle and nosecone for the sake of simplicity, due to the fact that tower and blades are the largest contributing sources for scattering. The nacelle can be considered to be significant scatterer for 90° broad side angle and nosecone is usually insignificant at all angles [52]. As shown in Figure 3.1, blades and tower are modeled by M plates and N cylinders, respectively which are small enough to achieve realistic far-field conditions. In this figure, $\alpha = \theta_{rot}$ is the rotation angle in xy-plane, $\beta = \theta_{yaw}$ is the yaw angle in yz-plane. In the proposed canonical model for WT, the tilt back angle of the blades has been assumed as zero in order to provide simplicity.

By using the segmented WT model introduced, received echo signals from a WT could be composed synthetically as the function of fast time as provided in equation 3.1

$$s_r(t) = \sum_{i=1}^{S_T} \sqrt{\sigma_i} \exp(j2\pi(f_0(t - \frac{2R_i}{c}) + K\frac{(t - \frac{2R_i}{c})^2}{2})), \qquad (3.1)$$

where $S_T = N + 3M$ is the total number of WT segments, σ_i and R_i are the RCS and distance (w.r.t. the radar) of ith segment. Here, N and M denote the number of segments of the tower and each blade of the WT, respectively.

For each pulse transmission instance in a radar operation, RCS and range values of all canonical segments that are treated as point scatterers are computed by also considering their orientations to the radar system. Thus, time-varying amplitude
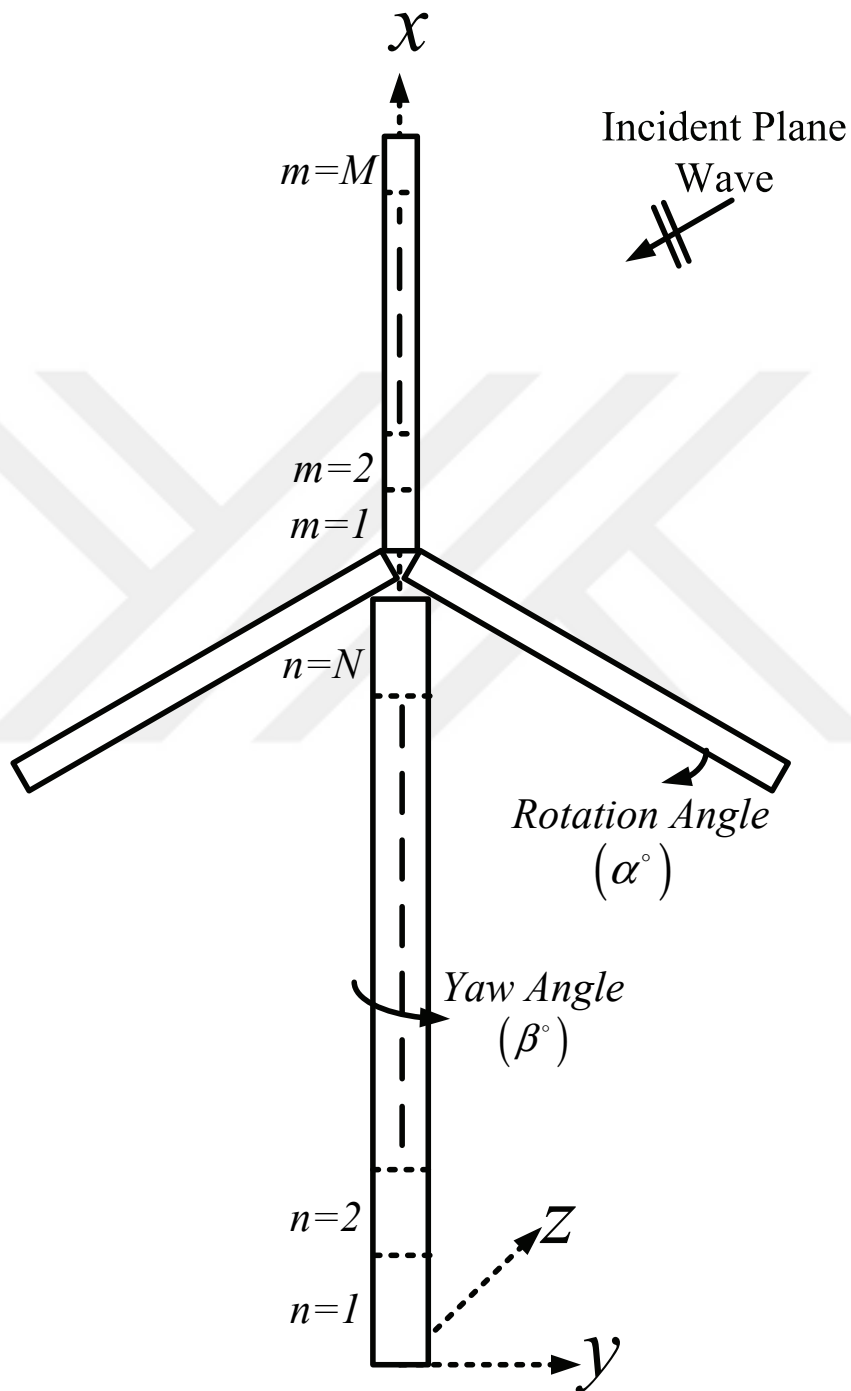
Figure 3.1 : WT model segmented by canonical structures.

and phase information are computed and contributed to the received signal. Those calculations are considered in the following subsections.

3.1.1 Analytical expressions for WT signal amplitude

The WT model introduced is a combination of rectangular and cylindirical segments, therefore, geometrical represantations and analytical RCS expressions for those geometrical structures are provided here. Initially, geometry of a conducting plate that is the constituent of WT blades is depicted in Figure 3.2.
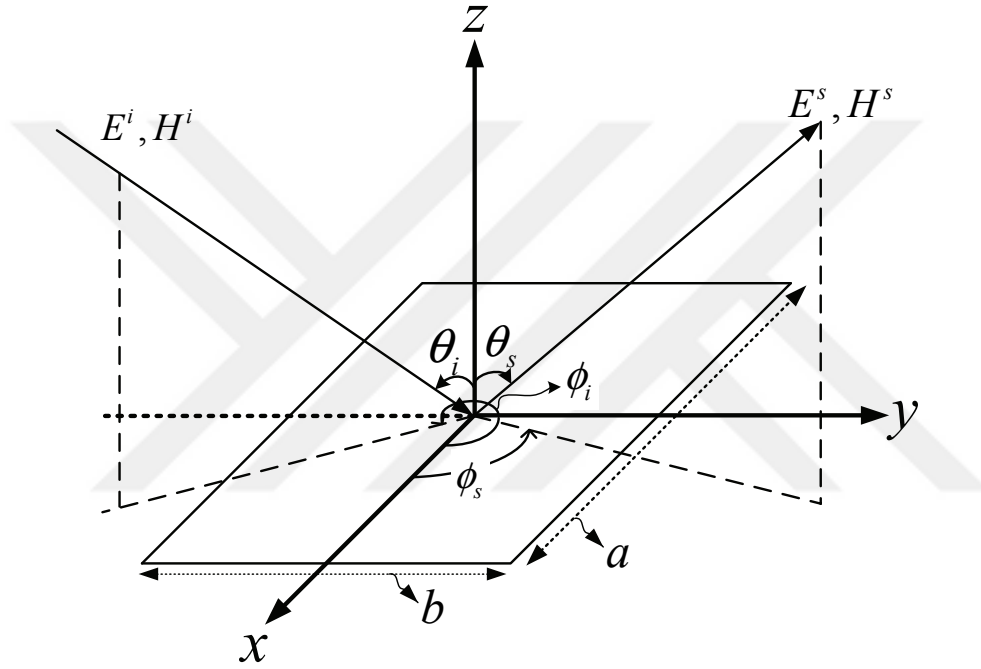
Figure 3.2 : Geometry of conducting rectangular plate.

In the figure, a and b are the length and width of the rectangular plate, E^i and H^i are the incident electrical and magnetic fields, respectively. Similarly, E^s and H^s denote scattered fields. Additionally, θ is representative for the angle on yz-plane and ϕ is the angle on xy-plane. The subscripts i and s are also stand for the incident and scattered field cases, respectively. Due to the considerations for radar operation, θ_s is equal to θ_i and ϕ_s is equal to ϕ_i for mono-static RCS calculations.

Bi-static RCS calculations of such a finite length PEC plate could be evauated as in the equation 3.2-equation 3.6 [53]:

$$\sigma_p = 4\pi \left(\frac{ab}{\lambda}\right)^2 (K_1{}^2 + K_2{}^2) \left(\frac{\sin(X)}{X}\right)^2 \left(\frac{\sin(Y)}{Y}\right)^2 \qquad (3.2)$$

54
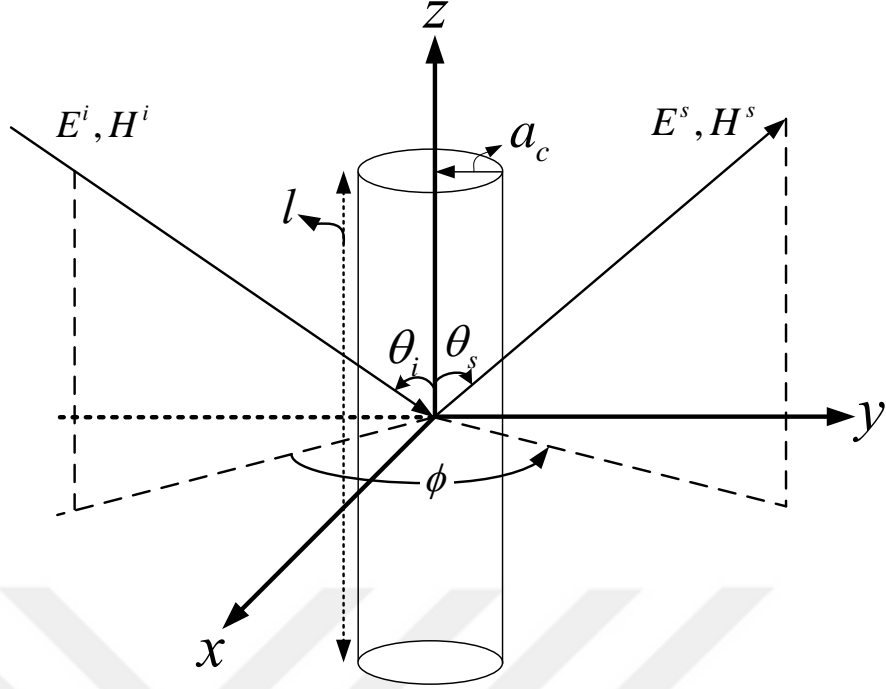
Figure 3.3 : Geometry of conducting cylinder.

$$K_1 = \cos{(\theta_i)}\cos{(\theta_s)}\sin{(\phi_s - \phi_i)} \tag{3.3}$$

$$K_2 = \cos{(\theta_i)}\cos{(\phi_s - \phi_i)} \tag{3.4}$$

$$X = \frac{kb}{2}\left(\sin{\theta_s}\sin{\phi_s} + \sin{\theta_i}\sin{\phi_i}\right) \tag{3.5}$$

$$Y = \frac{ka}{2}\left(\sin{\theta_i}\cos{\phi_i} + \sin{\theta_s}\cos{\phi_s}\right). \tag{3.6}$$

RCS calculations for the other WT constituent, finite length PEC cylinder that in shown in Figure 3.3, is given in equation 3.7-equation 3.11 [54]. In the figure related to the finite length cylinderical segment, a_c is the radius and l is used for the height of the cylinder.

$$\sigma_c = \frac{4l^2}{\pi k^2 \sin^2{\theta_i}}\left(\frac{\sin{(Z)}}{Z}\right)^2\left\{(K_3)^2\left|\sum_{n=-\infty}^{\infty}(-1)^n n e^{jn\phi} a_n\right|^2 + (K_4)^2\left|\sum_{n=-\infty}^{\infty}(-1)^n e^{jn\phi} b_n\right|^2\right\} \tag{3.7}$$
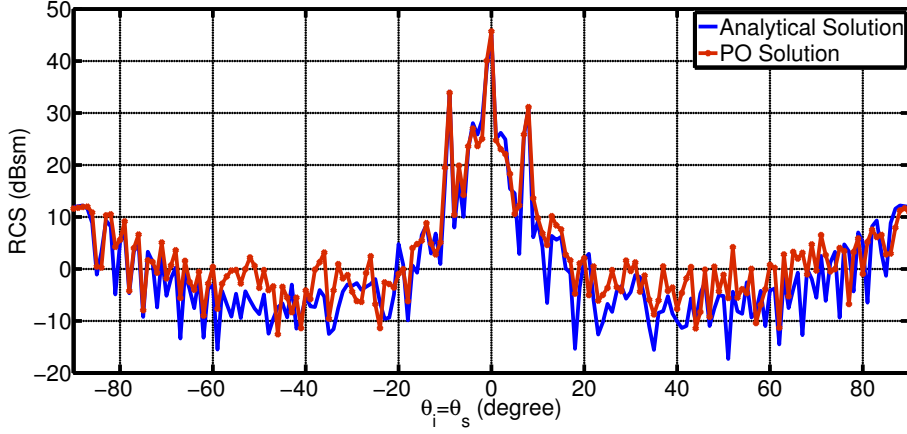
Figure 3.4 : Mono-static RCS of a WT for $f = 1$ GHz, $a_c = 2$ m, $l = 30$ m, $a = 20$ m, $b = 4$ m, $M = 10$, $N = 10$, $\phi_i = \phi_s = 10°$, $\theta_{rot} = 10°$, $\theta_{yaw} = 5°$

.

$$K_3 = \frac{\sin(\theta_i)\cot(\theta_s) + \sin(\theta_s)\cot(\theta_i)}{a_c} \qquad (3.8)$$

$$K_4 = k\sin(\theta_i) \qquad (3.9)$$

$$a_n = \frac{J_n(ka_c\sin\theta_s)}{H_n^{(2)}(ka_c\sin\theta_i)} \qquad (3.10)$$

$$b_n = \frac{J'_n(ka_c\sin\theta_s)}{H_n^{(2)'}(ka_c\sin\theta_i)}. \qquad (3.11)$$

It is possible to calculate total RCS of a WT (σ_T) by coherent summation of the reflected fields from the individual WT segments [55], [56] via

$$\sigma_T = \left| \sum_{n=1}^{(N+3M)} \sqrt{\sigma_n}\exp\{-i\psi_n\} \right|^2, \qquad (3.12)$$

where σ_n is the RCS of the nth scatterer segment and ψ_n is the relative phase of that particular contribution due to its physical location in space. With the formulation given in equation 3.12, RCS of the WT modeled through combinations of relatively small canonical segments is evaluated. Obtained analytical results are validated by comparing with the ones that are calculated through PO method. Analytical and PO solutions are seen to be in a good agreement according to the validation result given in Figure 3.4.

3.1.2 Analytical expressions for WT signal phase

Phase of the echo signal depends on the instantaneous range of canonical segments to the radar system. Time-varying range of a canonical segment can be obtained as

$$R_i(t) = R_0 + v_i t, \tag{3.13}$$

where R_0 is initial range and v_i is the radial velocity of ith canonical segment. The cylindrical segments of the WT tower yield zero radial velocity. However, because of the blades' rotation the rectangular segments of the WT blades possess radial velocity causing Doppler frequency shift which is significative for radar systems. Radial velocity of a plate segment can be expressed as

$$v_i = (\Lambda) l_i \frac{2\pi(RPM)}{60} \sin(\theta_{yaw}) |\cos(\pi - \theta_{rot})|, \tag{3.14}$$

where l_i is range of the plate segment from turbine nacelle, Revolutions Per Minute (RPM) is the turbines' rotational velocity, θ_{yaw} and θ_{rot} are the turbines' yaw and rotational angle, respectively. In equation 3.14, Λ is the sign defining parameter of the velocity function which has the value $'-1'$ when the rotation angle varies between $90°$ and $270°$ and $'+1'$ for the other rotation angle values.

3.2 Scattering Characteristics of Wind Turbines For Various Aspect Angles

In PDR systems, targets having radial velocity higher than the cutoff velocity of the MTI filter might result in target detections when satisfying detectable signal amplitude level. The canonical segments on WT blades are likely to be detected by the radar in the case of the WT has a yaw angle to produce enough radial velocity. However, blade segments could not produce moving target signature due to not satisfying signal amplitude enough to be detected even when the WT has a yaw angle that has the potential of producing Doppler components. Stationary tower of the WTs generally has large RCS values which affects the dynamic range of the returned signal and might be the reason for the blade segments to be desensitized and not to be detected. Therefore, the RCS value difference between the tower and the blade segments has an important role in the detectability of the blade segments.

As previously mentioned, in SAR systems, cross-range information of the targets are constructed according to their Doppler signatures. For that reason, despite being in the same location physically, blades and the tower might be seen in different cross-range positions depending on their instantaneous Doppler characteristics. Actually, this is the main reason lying under the problem of WT-SAR interaction which will be investigated in the following chapters. Having complicated motional properties, WT blades might cause blurring or other deteriorations in the case of high scattering conditions. However, generally the WT towers have the potential to suppress deteriorating blade effects with their large RCS values. Therefore, similar to the case in PDRs, RCS levels between the blades and the tower again have much importance in terms of SAR systems.

RCS levels of the WT parts strongly depend on the instantaneous position with respect to the radar system. Due to their horizontal or vertical rotation capability, the aspect angle through WT and at the same time the scattering characteristics of WT segments change instantaneously while the radar is in operation. In order to characterize instant WT scatterings, some theoretical and experimental analyses are performed. The analyses are presented in this section with the aim of forming priory knowledge about WT deteriorations on the detection, tracking and the imaging performances of radar systems.

3.2.1 Theoretical analyses

Theoretical analyses of WT scattering start with the investigation of WT segments' RCS variation in terms of the horizontal rotation. In this case, WT blades rotate according to a vertical plane of rotation with some yaw angle. WTs perform a proper rotation in the case of a change in the wind direction to benefit from wind power efficiently. Figure 3.5 depicts the RCS variation of tower and blade tip segments with respect to the radar illumination angle (i.e., θ) which is obtained using the range and altitude difference between radar system and the WT nacelle height (h_{nac}).

The RCS characteristics in Figure 3.5 have been given for the variation of θ within the range $[0°, 10°]$ (corresponding to altitudes within $[h_{nac}, h_{nac} + 5290]$ in meters). $\theta = 0^o$ represents the case that the radar altitude is about h_{nac} and θ is about $5°$ when the radar altitude is 3000 m. RCS calculations are performed for $\theta_{rot} = 0^o$. In Figure 3.5a, it can
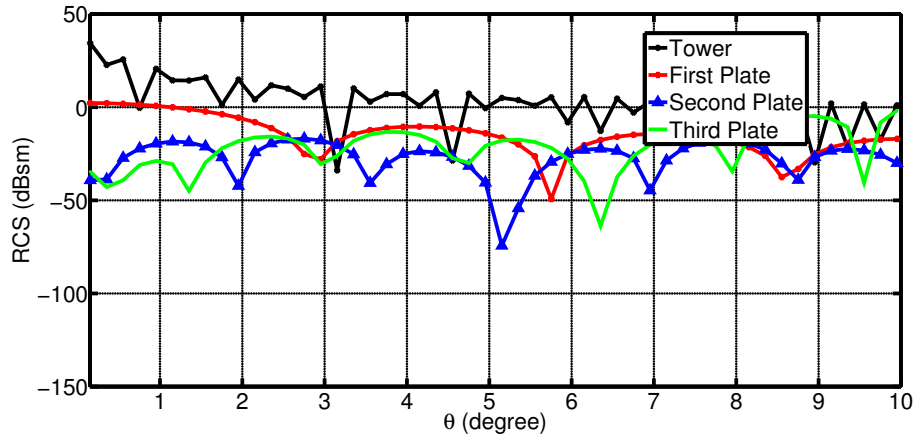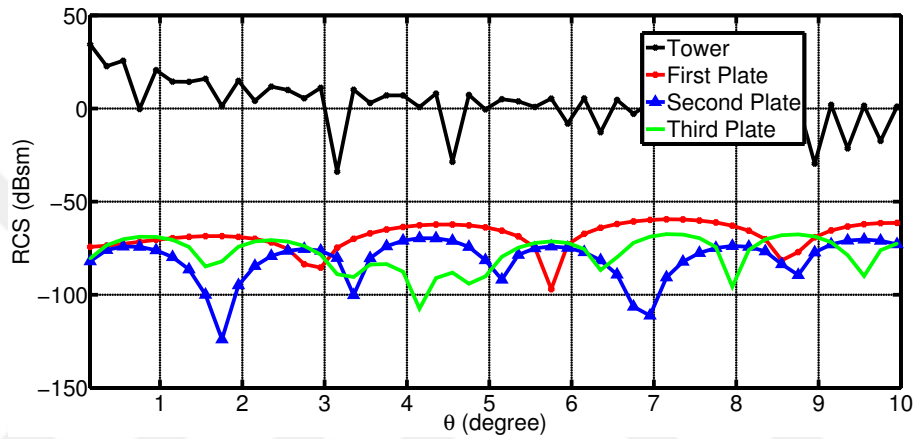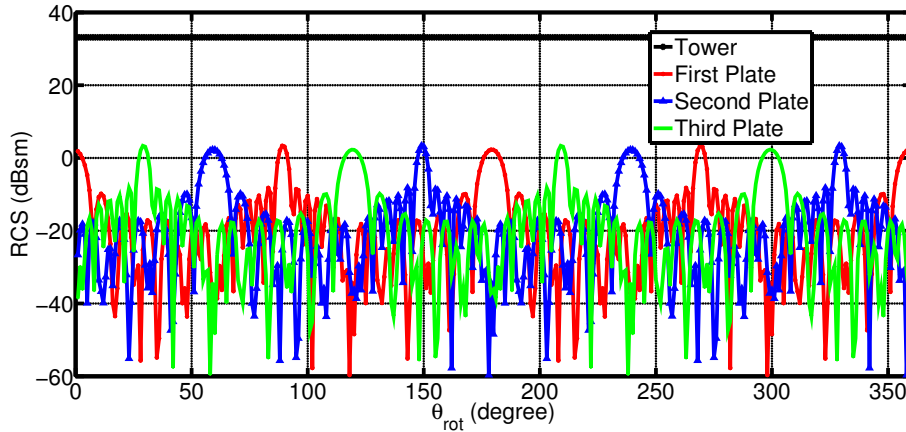
Figure 3.5 : RCS variation of tower and blade tip segments (plates) for: a) $\theta_{yaw} = 20^o$, b) $\theta_{yaw} = 89^o$.

be observed that the RCS difference between the tower and the first blades' tip segment is about 35 dBsm for $\theta_{yaw} = 20^o$ and $\theta = 0^o$, and decreases while the radar altitude increases. On the other hand, in Figure 3.5b, there are large RCS differences which are on the order of 100 dBsm for $\theta_{yaw} = 89^o$ and $\theta = 0^o$, whereas the difference is about 75 dBsm for the radar altitude 3000 m. According to the RCS variation graphics, in spite of producing lower radial velocities, rotational blade tip segments are more likely to be deteriorating when the turbine has lower yaw angle values due to the smaller RCS difference with the tower. At higher yaw angle values, proportional to the large RCS difference, high Doppler-shifted returns from blade segments could not produce significant signatures in radar systems.

Scattering characteristics of a WT might be also significantly variable according to the WT blades' rotation angle. Due to the radar system's and the WTs' non-stationary nature, radar system coincides the WTs with different rotation angles in different pulse

transmission instances. Figure 3.6 exhibits RCS levels of WT segments in terms of the rotation angle.

(a)
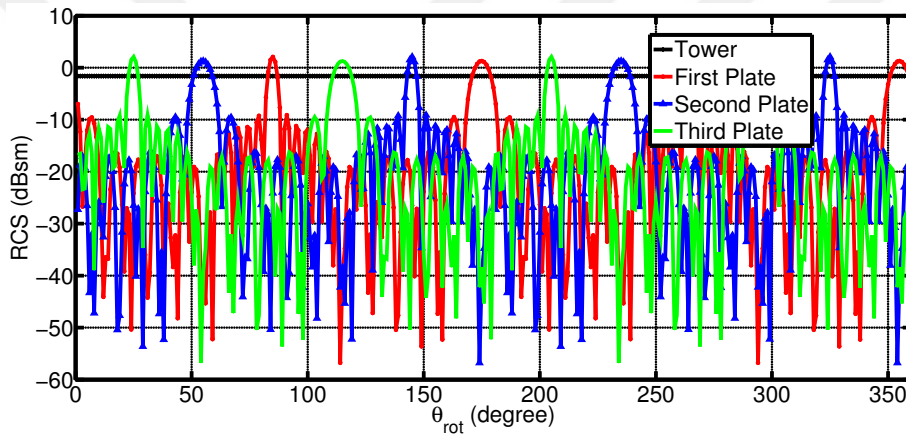
(b)

Figure 3.6 : RCS variation of tower and blade tip segments (plates) with respect to θ_{rot} for $\theta_{yaw} = 20^o$ for radar altitude: a) 200 m, b) 1000 m.

In Figure 3.6, RCS variations of the tower and the blade tip segments with respect to θ_{rot} are depicted for $\theta_{yaw} = 20^o$. As seen clearly from the figures, the blade scattering characteristics seriously differ for various rotation angle values. Different blades are seen to cause flashes at different rotation instances. One another information that can be inferred from the figures that the effect of altitude difference between the radar system and the WT to the segments' RCS levels. When the mentioned altitudes are close to each other, WT tower dominates the blade signals with it's large RCS.

3.2.2 Experimental analyses

Additional to the theoretical ones, experimental scattering analyses of a model WT are also performed in order to put forth the scattering properties of WTs in terms of

practical point of view. In Figure 3.7, experimental time-frequency analysis results of a WT is depicted. In the experiments, a low cost C band radar [57] and a model WT with 48 cm hub height and 40 cm blade length is used. Moreover, the WT was positioned with $0°$, $60°$ and $90°$ yaw angle values, and the radar system was operated in spotlight working mode. When investigating the results, it could be exposed that there are strong signal contributions at zero frequency region due to the ground-based clutter and the stationary parts of the WT. Additionally, it could be captured from the figure that, WT blades cause higher Doppler frequencies but lower RCS with respect to stationary tower at high yaw positions proper to the theoretical results.

As a summary, theoretical and experimental studies present that the RCS of WT blade segments vary quite significantly depending on the blade yaw angle, blade rotation angle and the altitude difference between the turbine and the radar system. On the other hand, RCS of stationary tower is seen to be same for variable yaw and rotation angles. Moreover, it is clearly demonstrated by the analyses that RCS difference between the stationary and rotational parts significantly vary with respect to the mentioned parameters. The effects of that difference in deteriorating WT effects are vital and would be felt throughout deterioration investigations.
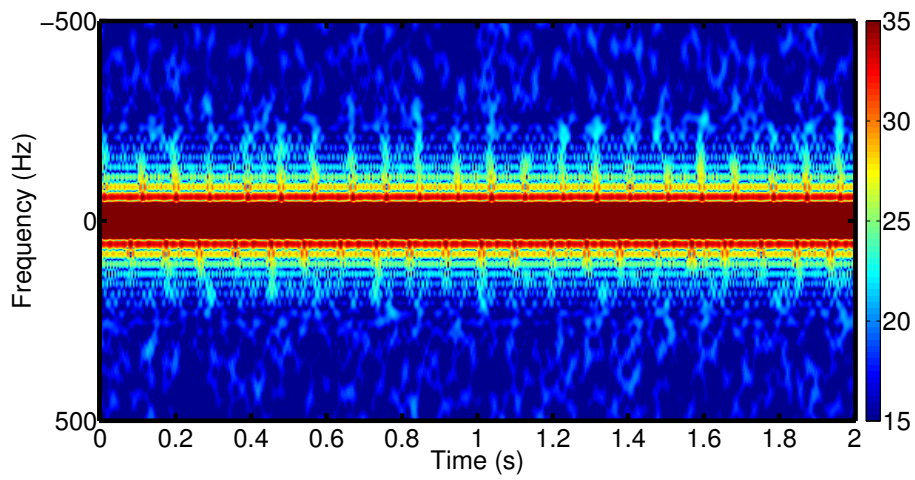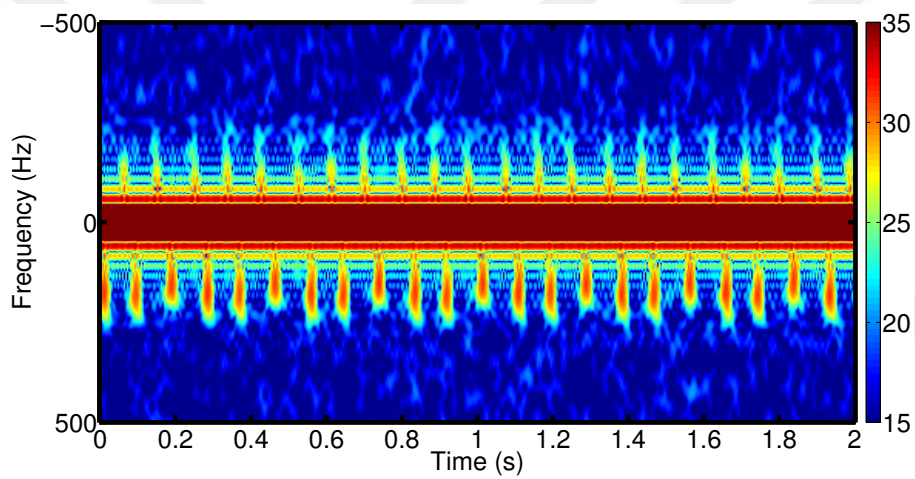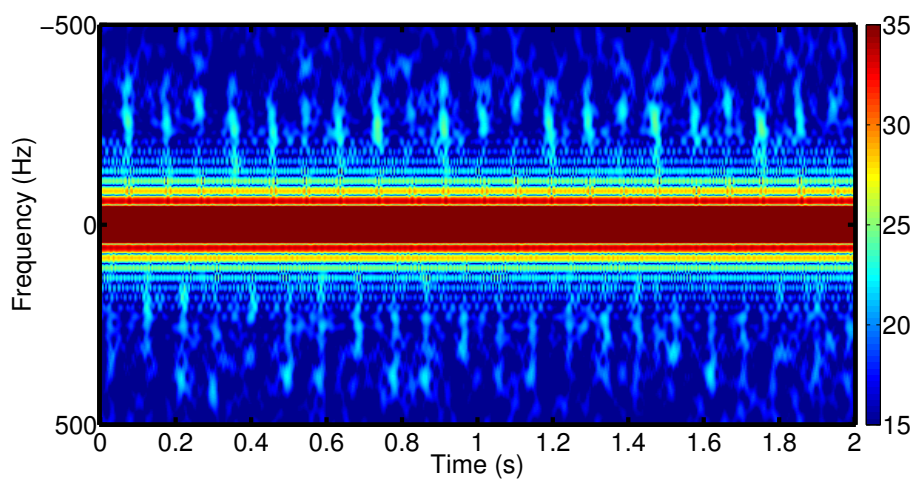
Figure 3.7 : WT detection experiment for yaw angle: a) 0°, b) 60°, c) 90°.

4. INVESTIGATION OF WIND TURBINE EFFECTS ON RADAR DETECTION AND A MITIGATION APPROACH

Throughout this chapter, first of all, detection characteristics of WTs on 2-D pulse-Doppler radar systems are investigated. By using the processing baseline introduced previously, various simulations are performed considering different radar-to-WT aspect scenarios. Simulation results related to the analyses of WT detection made possible to construct charts about WTs' probability of detection. Additionally, by using these results, an analytical clutter model for WTs (namely Wind Turbine Clutter, WTC) is modelled. WTs might strongly effect the detection performance of realistic or genuine targets (GT) on radar systems. Therefore, this situation is also investigated with assigning various aspect properties to a WT in the manner of yaw angle. At the end of this chapter, proposed mitigation approach about minimizing the WT effects on radar detection performance is described.

4.1 Wind Turbine Detection Characteristics

Simulation studies dealing with the WTs' detection in different radar-WT orientations are performed using the signal model proposed in Chapter 3. In the simulations, assuming the existence of LoS between the radar and the WT and assuming that the all segments of the WT are located in the same radar resolution cell, 2-D raw data matrix representing the radar-scan data for one azimuthal sector is constructed using the signal model as a first step. Then, the prepared data matrix is processed using conventional PDR signal processing scheme that is previously explained and composed of matched-filtering, moving target indicator (MTI) filtering with 3-Pulse Canceller MTI filter, Doppler processing with 256 lengths FFT followed by 20 dwells non-coherently integrated and finally constant false-alarm rate (CFAR) detection. Note that the detection process is a cell-averaging CFAR with a total window of 23 range cells and a guard region of 5 range cells. The propagation and antenna pattern effects are not included in the simulations due to being out of scope of this study.

In terms of the radar system, analyses about the WTs' detection take an S-band air surveillance radar system that has the operational parameters summarized in Table 4.1 into account.

Table 4.1 : Operational parameters of the radar system.

| Radar Parameters	Value	Unit
Frequency	3	GHz
Chirp Bandwidth	1	MHz
Sampling Frequency	2	MHz
PRF	2000	1/s
Number of Integrated Pulses	20	-
MTI Filter Type	3 Pulse Canceller	-
FFT Length	256	-
CFAR Window Size	23	-
CFAR Guard Region Size	5	-

Physical properties of the tower and the blades play a critical role in detection of WTs. Among a variety of models, a typical turbine model with teschnical specifications given in Table 4.2 is considered in this study. Beside those physical features; as will be investigated via various simulations, yaw, rotation and the radar illumination angles are the other effective parameters in the detection of WTs.

Table 4.2 : Physical parameters of WT.

WT Parameters	Value	Unit
Nacelle Height	80	m
Blade Length	50	m
Number of Blades	3	-
Blade Segment Length	1	m
Blade Segment Width	2	m
Tower Segment Length	1	m
Tower Segment Radius	2	m
Blade Rotation RPM	10	-
Distance to the Radar	30	km

Analysis results about the WT's detection due to the variation of the yaw angle (i.e., θ_{yaw}) and the rotation angle (i.e., θ_{rot}) are presented in Figure 4.1 and Figure 4.2, respectively. In these figures, the blue line represents the Doppler spectrum (or radial velocity) for the range-bin under consideration, and the green line represents the threshold level that is determined by CFAR processing. Also, the red line demonstrates the amplified threshold that is calculated as the sum of the median value of the investigated Doppler spectrum and a threshold-offset of 7 dB which has been chosen

arbitrarily to regulate the false alarm rates. The sub-clutter visibility (SCV) of the simulation framework is experienced at a level of 35 dB for the considered parameters and processing scheme employed. In the simulations, altitude of the WT is specified as zero meters.
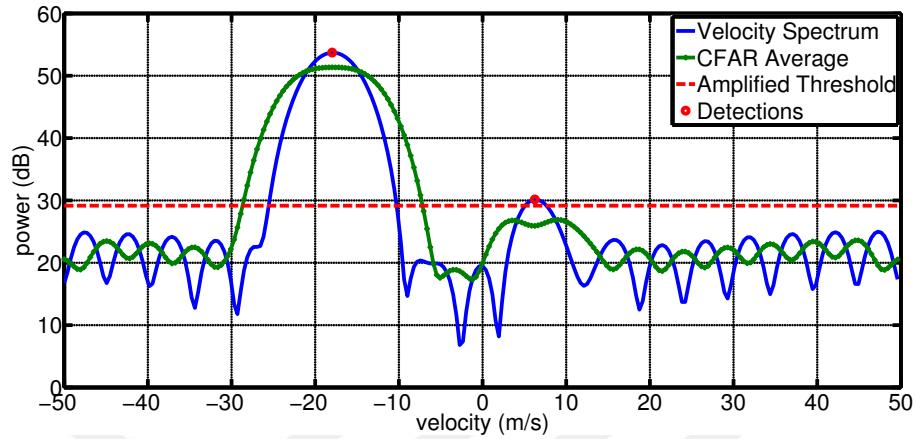
(a)
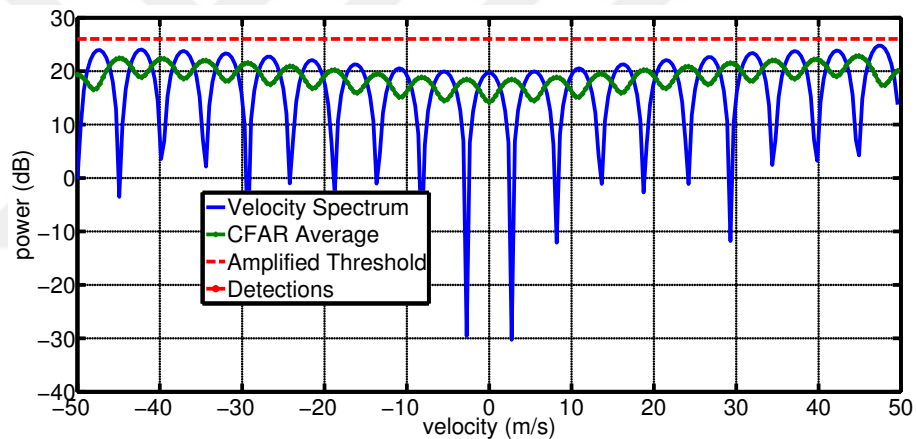
(b)

Figure 4.1 : Detections of WT for $\theta_{rot} = 60^o$ and radar altitude 1000 m for: a) $\theta_{yaw} = 20^o$, b) $\theta_{yaw} = 89^o$.

The effect of the yaw angle on the WTs' detection is clearly depicted through Figure 4.1. It was pointed out in the previous chapter that the WT blades could reflect back strong echoes in the case of low yaw angle values due to their scattering properties. Consistently, two spectral peaks that will pave the way the related WT to be detected by the radar system are seen on the detection processing result presented in Figure 4.1a. Here, one of the spectral peaks is caused by the blade 1 (receding one) and the other one is by the blade 2 (approaching one). On the other hand, despite causing larger Doppler frequency shift, WT with the yaw angle $\theta_{yaw} = 89^o$ could not result in detections in the radar system as seen in Figure 4.1b. The reason for that situation can

be explained by considering the weak scattering properties of the blades at high yaw values. Obviously, signals from the blades could not exceed the SCV level in this case and desensitized by the strong echoes of the stationary WT tower.

Instantaneous rotation angle have the potential to diversify the detection characteristics of WTs as presented in Figure 4.2. It was also previously expressed that different WT blades cause flashes at various observation instants. This can be exposed by analyzing the simulation results depicted in Figure 4.2a and Figure 4.2b. In the first one where $\theta_{rot} = 0^o$, only one approaching target signature caused by the first blade is seen. However, two detections one of which is related to the approaching blade (i.e., blade 1) and the other related to the receding one (i.e., blade 2) are observed when $\theta_{rot} = 70^o$.

(a)
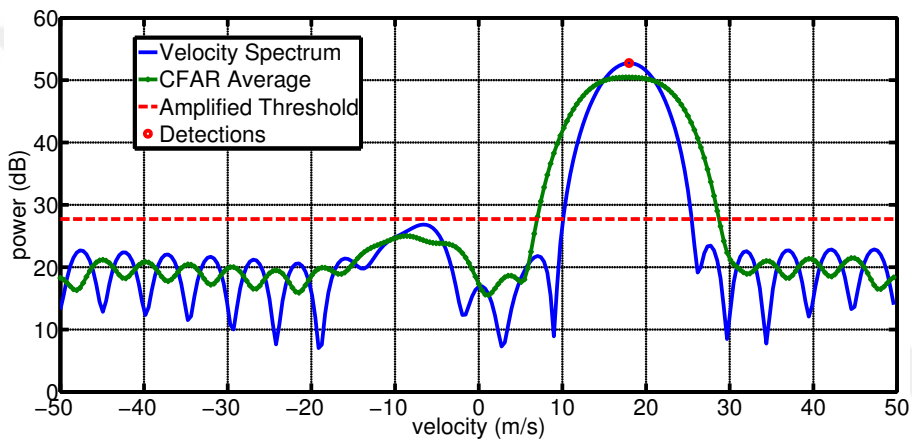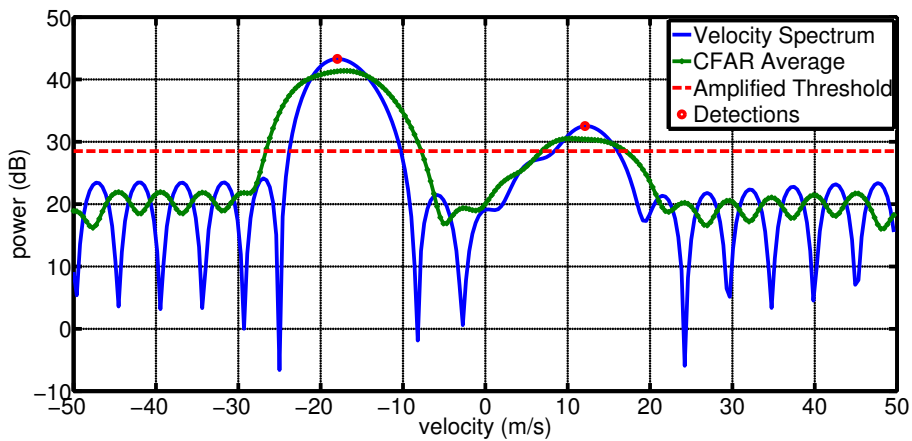

(b)

Figure 4.2 : Detections of WT for $\theta_{yaw} = 20^o$ and radar altitude 1000 m for: a) $\theta_{rot} = 0^o$, b) $\theta_{rot} = 70^o$.

Various simulation results about WTs' detection are presented in this section. It can be observed from the simulations that, WTs are likely to yield uncorrelated moving target signatures for the successive radar scans due to the radar-WT orientation and

66

Table 4.3 : Detection results for a few radar scans.

	Scan #1	Scan #2	Scan #3	Scan #4	Scan #5
WT Rotation Angle (^{o})	0	70	330	20	170
Detected Velocities (m/s)	18	$-18, 12$	$-14, 16$	$-15, 16$	-18

related scattering characteristics of the WT parts. Even if θ_{yaw} is assumed to be fixed and known according to the wind direction, radar system would coincide the WT with different rotation angle in successive scans due to the unsynchronized rotational motions of radar system and the WT.

In Table 4.3, turbine orientation in terms of the rotation angle and the related detection results are given for a sample radar scan. Simulations are performed for $\theta_{yaw} = 20^o$ and the radar altitude 1000 m.

It is clear to see that the detections presented in the table are occured for different radial velocities in successive radar scan instants. Therefore, those results describe the probabilistic nature of the WT detection process.

Other than the blades' rotation angle, WTs' orientation, rotational speeds of the radar and the WT and the scattering characteristics are some other factors that determine the value of the radial velocity for which a spectral peak occurs to cause a detection. By considering all of those factors, detection behaviour in a radial velocity bin is expected to be random. Hence, each radial velocity bin within the unambiguous velocity range could be assumed as independent random variables and detection statistics for those bins can be constructed. Simply, by keeping some of the factors as constant, distributions about the probability of WTs' detections in each velocity bin can be obtained. These distributions will give information about long term effects of WTs on a radar system. Therefore, such an analysis could help to interpret the need or the methodology for WTC mitigation.

In Figure 4.3, probability distributions about the WT's detections which are obtained by realizing 36000 rotation angles from the uniform distribution and running detection algorithms for each rotation angle are depicted. Detection distributions are generated for $\theta_{yaw} = 80^o$ and two radar altitudes. Figure 4.3, depicting the probability distributions point out that, for the simulated scenarios there would be WT detections for almost all the velocity range except the velocities close to the zero velocity with the

probabilities below 0.1 for the radar altitude 500 m, and below 0.2 for the radar altitude 3000 m. Furthermore, probability of detection for the velocities tends to increase as the radial velocity value increases from zero to unambiguous velocity.

Constructed probability distributions given in this section provide the information about the long term WT effects on the radar system and might be useful when determining the WT mitigation requirements. For instance, for the case given in Figure 4.3a, there might be no need for the mitigation since the detection probability of the WT is below than 0.1 for all radial velocities.

(a)

(b)
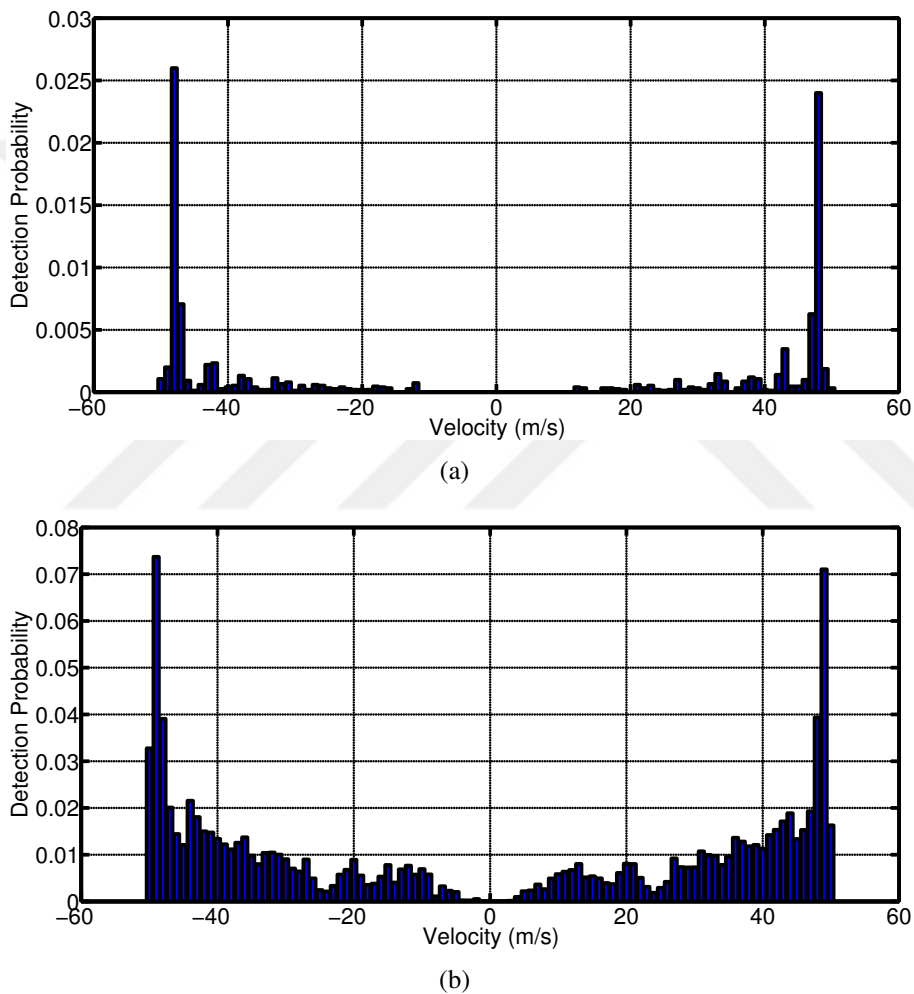
Figure 4.3 : WT detection distributions for $\theta_{yaw} = 80^o$ for: a) Radar altitude 500 m, b) Radar altitude 3000 m.

4.2 Wind Turbine Clutter Modelling Approach

Detections of WTs are considered as clutter (WTC) due to being undesired target plots in radar systems. By taking the WTs' detection results into account for various

simulation scenarios, it is possible to construct an analytical and probabilistic WTC model in terms of the motion and scattering characteristics of the WTs. Mathematical expressions related to the WTC could be defined with the help of the instantaneous RCS and velocity formulations which are used in the proposed signal model previously. Assuming a fixed yaw angle related to the wind direction and a rotation angle which is considered as uniformly distributed between $0°$ and $360°$, the WTC model of a WT blade which is composed of RCS ($\sigma_{WTC,b}$) and radial-velocity information ($v_{WTC,b}$) might be defined as provided in equation 4.1.

$$v_{WTC,b} = \mathrm{mod}\,(v_{tp}, PRF) f_{MTI\_3PC}(v_{tp}) u(\sigma_{tp} - (\sigma_h - SCV)) \qquad (4.1)$$

$$\sigma_{WTC,b} = \sigma_{tp} \qquad (4.2)$$

Here, σ_{tp} and v_{tp} defines RCS and the radial velocity of the blades' tip segments, and $u(.)$ stands for unit step function. Moreover, $f_{MTI\_3PC}(\cdot)$ is the velocity spectrum of the MTI Three Pulse Canceller whose function is to filter out stationary and slowly moving targets and has an analytical definition as

$$f_{MTI\_3PC}(v) = \left| \Im\{h[n]\}_{f=\frac{v}{\lambda}} \right| = 4\sin^2\left(\frac{2\pi v}{\lambda N_{FFT}}\right) \qquad (4.3)$$

where $h[n] = [1 \quad -2 \quad 1]$, $\Im\{\cdot\}$ denotes the Fast Fourier Transform (FFT) operator, N_{FFT} is the FFT size, v is the value of radial velocity in m/s and λ is the wavelength. In equation 4.1, σ_h is the RCS of the WT tower and can be calculated through as described in the previous chapter considering the segments found on the tower of the WT. Additionally, $\mathrm{mod}\,(\cdot, \cdot)$ is the modulo operator which controls the unambiguous velocity range while the step function controls the signal level of the WTC considering the scattering properties of the blade, stationary part (i.e., tower) of the WT and SCV value. The yaw and the probabilistic rotation angles of the blades determine the initial observation angle values in the RCS definitions and are inputs to the blade segments' velocity definitions.

From Figure 4.4 to Figure 4.7, performance of the proposed WTC model is demonstrated for four simulation scenarios. In those figures, distributions about the
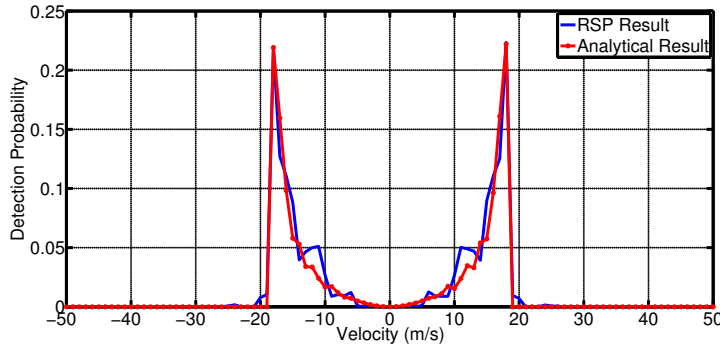
Figure 4.4 : WTC model performance evaluation for radar altitude 1000 m - $\theta_{yaw} = 20^o$.
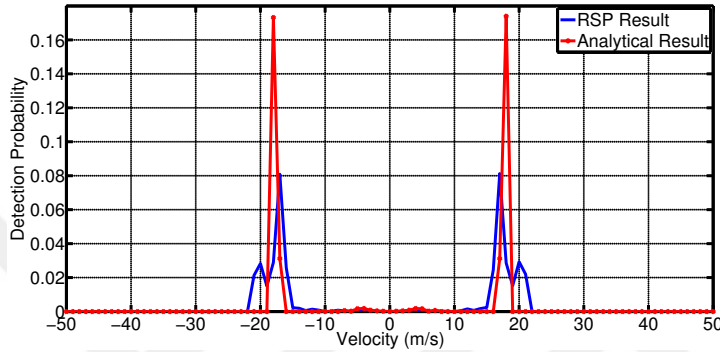
Figure 4.5 : WTC model performance evaluation for radar altitude 500 m - $\theta_{yaw} = 20^o$.

detections occured for radial velocity bins are presented for both of PDR processing scheme and the introduced clutter model. Analytical model is seen to be in a good agreement with the PDR processing scheme for the cases in which RCS difference between the tower and the rotational blade segments are close to each other. Related results are exhibited in the Figures 4.4 and 4.6. On the other hand, when the RCS difference is quite large especially in lower radar altitude or higher yaw angle cases, variations between two distributions draw the attention as depicted in Figure 4.5 and Figure 4.7. The reason of the variations originates due to the false target detections in the PDR processing scheme in the related cases. The correlation values between the distributions obtained through PDR scheme and the analytical model is evaluated as 0.9759, 0.4101, 0.8573 and 0.7707, respectively for the scenarios considered here.

4.3 Detection Characteristics of Genuine Targets in the Vicinity of Wind Turbine Clutter

It would be clearly interpreted according to the WTs' scattering and the detection characteristics that the detection of the GTs is inevitable effected in the vicinity of

70
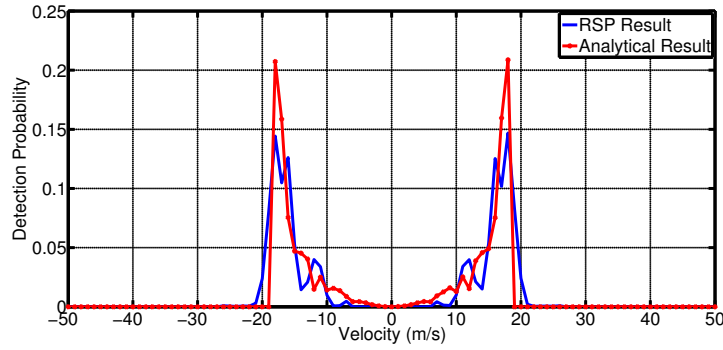
Figure 4.6 : WTC model performance evaluation for radar altitude 2000 m -
$\theta_{yaw} = 20^o$.

Figure 4.7 : WTC model performance evaluation for radar altitude 1000 m -
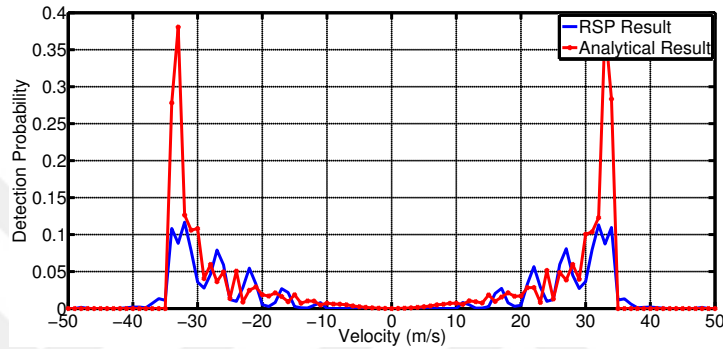$\theta_{yaw} = 40^o$.

WTs. This could be demonstrated via again constructing probability distribution of radial velocity bins in the case of a simulation scenario in which a GT with known RCS and radial velocities inserted in. By using such a scenario, detection performance of a GT could be tested through examining probability of the radial velocity bin related to the GT.

Assuming a genuine target of 0 dBsm RCS and -24 m/s radial velocity, considered simulations are performed for the radar altitude 200 m. Figure 4.8 depicts the probability distributions for two cases in which $\theta_{yaw} = 20^o$ and $\theta_{yaw} = 80^o$, respectively. According to the figure, it can be inferred that the detection performance of the target is adversely effected for the case where WT blades demonstrate strong scattering characteristics. The decrease in the target's detection performance is presented in Figure 4.8a. On the other hand, due to weaker blade reflections, target is effected slightly in the manner of detection on the radar system as depicted in Figure 4.8b.

Using the procedure introduced here, the evaluation of the detection performance of targets could be performed for various scenarios and targets with different scattering characteristics.
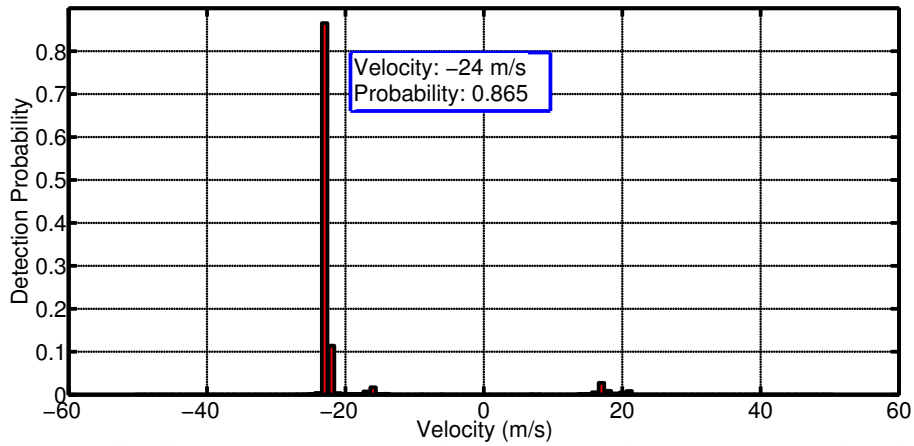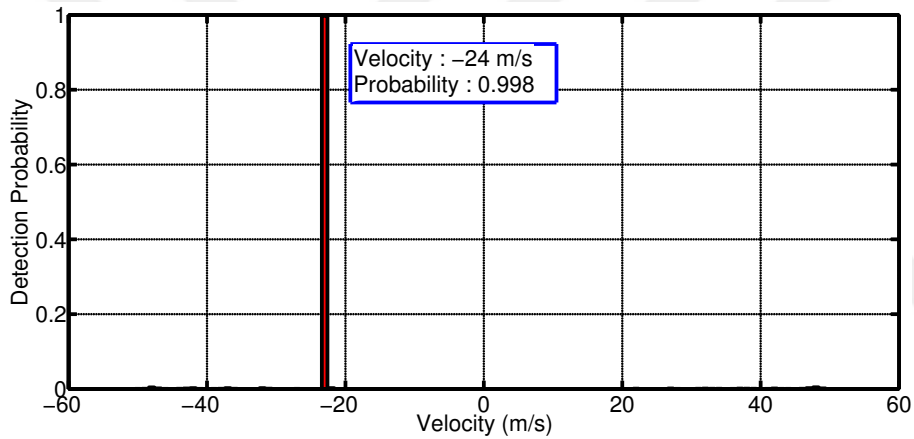
Figure 4.8 : Detection performance of a target for radar altitude 200 m for: a) $\theta_{yaw} = 20^o$, b) $\theta_{yaw} = 80^o$.

4.4 Wind Turbine Clutter Mitigation Approach for Radar Detection Stage

Up to now, scattering and detection characteristics of the WTs are investigated in terms of several points of view. By using those investigation results, it is possible to determine the necessities or develop insights about the newly problem of the radar systems, WTC mitigation phenomena. When investigating the related literature, it could be observed that so many researchers and radar engineers have been consuming intensive effort to minimize or mitigate the WT effects. In this scope, auxiliary gap-filler radars are employed in order to overcome the WT-based shadowing effects [9]. Additionally, some of approaches such as blocking the LoS between the radar and

WTs, implementing the procedures related to stealth technology [52] or improving processing schemes have been applied in order to mitigate the effects that are closely related to the clutter, missed detections or problems in target tracking. Due to the considerations about WF areas in terms of wind-power efficiency, blockage of the LoS could not be feasible generally. Moreover, stealth technology brings about covering the WTs with lesser reflective dielectrical materials or shaping. However, higher expenses in covering materials and complication with the shaping due to aerodynamical considerations obstruct the usage of stealth technology. The most effective WTC mitigation procedures which takes the advances in the signal processing scheme into account are described in [25] and [20]. Adaptive clutter mapping process to identify range cells where the WTs found followed by blanking those cells is suggested in [25]. Besides, in [20], a group of procedures including beam processing during pre-detection interval, Doppler-based clutter mapping and enhanced CFAR during detection interval, and the adaptive tracking logic during the post-detection interval are proposed to mitigate WTC.

The most effective methods in eliminating the WT effects are probably the ones that are applied at the detection stage of radar processing procedures. The elimination of WTC at this stage would account for minimized deteriorations on the detection and tracking performances of GTs. Some of the approaches propose raising the detection thresholds up in radar systems for WF areas, however, those give rise to creation of blind zones where no detection could be achieved. One another method about mitigating WTC at the detection stage [25] suggests to identify WT locations using adaptive clutter mapping and perform mitigation via blanking those locations at the CFAR processing step. In [20], WTC mitigation is applied using the priory information of WT locations and ignoring them at the CFAR stage. It is obvious that both of [25] and [20] apply blanking or ignoring only the range cells where the WTs are found. On the other hand, after matched-filtering operation over fast time data, point scatterers are placed in the range profiles with a Point Spread Function (PSF), hence, they might spread over several range cells depending on the duration of employed signal waveform. In the case of LFM signal as considered throughout this study, matched filtering outputs result in sincs with the duration of two times the transmitted pulse. Consequently, there would not be an effective WTC mitigation through blanking or ignoring only the range cells

73

where the WTs are found. PSFs contributed by WTs have to be suppressed in order to reach a succesful mitigation. Under these considerations, a novel WTC mitigation approach [58] which take the advantage of CLEAN algorithm is proposed. According to that method, range cells housing the WTs are detected by thresholding the average adaptive clutter map initially. Then, PSFs representing the WT contributions are subtracted from the range profiles according to the CLEAN algorithm before CFAR processing to reach WT free range profiles. Finally, WT free target detections are performed via employing CFAR processing on those range profiles.

4.4.1 WTC detection stage

It is possible to find out the locations of interfering WTs by exploiting their spectral and reflective characteristics mentioned in detail in previous chapters. In the case of illuminating an azimuthal sector in which a WT found, radar systems would receive time-varying and high reflective echoes from the range bins where PSF of the WT spreads. On the other hand, such echoe characteristics would not be observed for the range bins that are not related to the WT. Therefore, an averaging process over Doppler filter outputs for multiple radar scan instants paves the way of detecting interfering range bins in MTD based PDR systems [25]. Similar process can be accomplished in MTI-based systems through adaptive clutter mapping for zero and non-zero filter outputs. Detection of the interfering range cells is completed via applying CFAR processing over the averaged clutter maps along the range direction, and thresholding by a margin in order to control false alarm rate. Introduced WTC detection stage is schematized in Figure 4.9 with a block diagram.
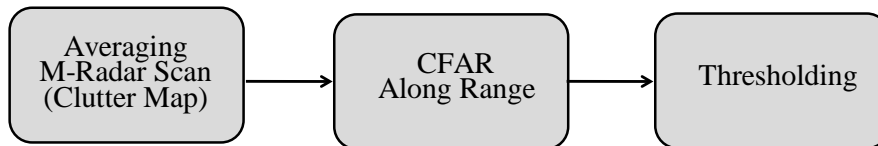

Figure 4.9 : Block diagram for identification of WT locations.

4.4.2 WTC mitigation stage

Proposed WTC mitigation scheme mainly deals with the subtraction of PSFs related to interfering WTs from matched-filtered radar data. Matched-filtering over a fast time data series would result in a range profile consisting of PSFs which are centered at the

74

scatterer locations and weighted in amplitude with the scatterers' echoe power. As an exemplary, Hamming-windowed PSF of LFM waveform is depicted in Figure 4.10.
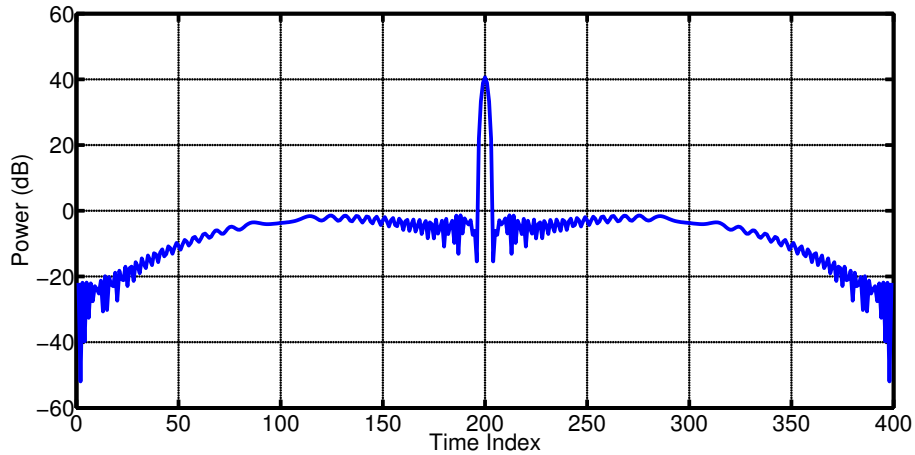
Figure 4.10 : PSF for Hamming windowed LFM.

According to the considered mitigation approach, if one could remove the PSFs belonging to WTs from matched-filtered radar data, WTC free range profiles would be reached and relatingly WTC can be mitigated. At this point, the CLEAN algorithm [59] is utilized. It has been used commonly in radioastronomy and image processing areas to extract or subtract dominant scatterer locations. The CLEAN algorithm which exploits PSFs to extract or subtract the scatterer points in an image is also employed for radar processing applications [60].

Similar to the usage in image processing applications, the CLEAN algorithm is employed to remove the PSFs caused by WTs. The processing procedure based on CLEAN is presented throughout the Figure 4.11. As can be inferred from the figure, an auxiliary range profile which includes the combinations of WT-based PSFs is constructed initially. Those PSFs are centered at the range bins related to detected WT locations and weighted by the signal amplitude of the corresponding range cells in the main range profile. Afterwards, in order to obtain WTC-free range profile, auxiliary profile is subtracted from the main range profile. Possible target locations are determined by applying CFAR operation to the WTC-free range profiles. Consequently, WTC free target detection process is completed with the Doppler processing on those candidate target locations.

Performance of the proposed WTC mitigation approach is examined for two different simulation scenarios by using the PDR processing scheme, radar and WT models
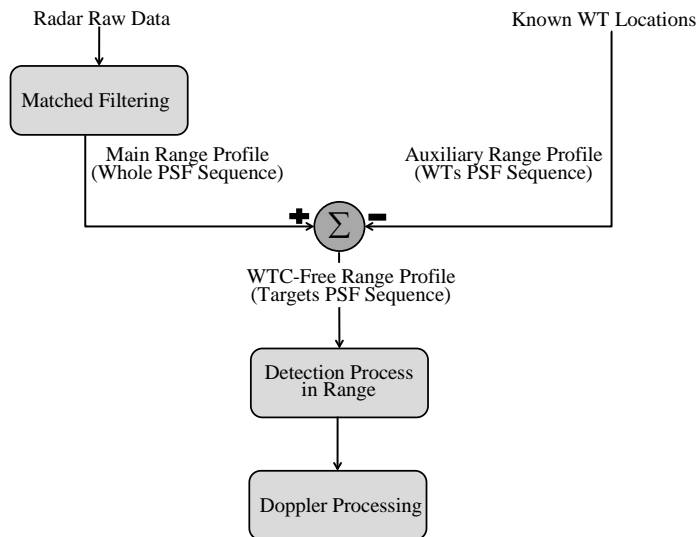
Figure 4.11 : Block diagram for WTC mitigation steps.

described previously. In the simulations, the WT is located as 30 km far from the radar system. Besides, in order to investigate the detection performance of a GT close to the WT, a target model with 0 dBm^2 RCS and 24 m/s radial velocity is inserted to the same azimuthal sector with the WT. The distances for the GT with respect to the radar are set as 30.5 km and 32 km, respectively for two simulation scenarios. With the assumption of having the knowledge about WT location, only the mitigation stage of the proposed approach is performed.

Simulation results for WTC Mitigation Scenario 1 in which the GT is settled as 30.5km far from the radar system are presented in Figure 4.12. According to the main range profile given in Figure 4.12a and obtained by matched-filtering operation, it will be quite difficult or even impossible for the radar system to discriminate the target and the WT in such a scenario. However, the contribution of the WT in the main range profile is seen to be significantly eliminated by applying the proposed mitigation approach. WTC-free range profile obtained after mitigation procedure and the main profiles are presented together in Figure 4.13b. Similar mitigation achievements are also acquired for the second scenario where the WT and the radar system are settled relatively sparse and the related simulation results are exhibited through the Figure 4.13.
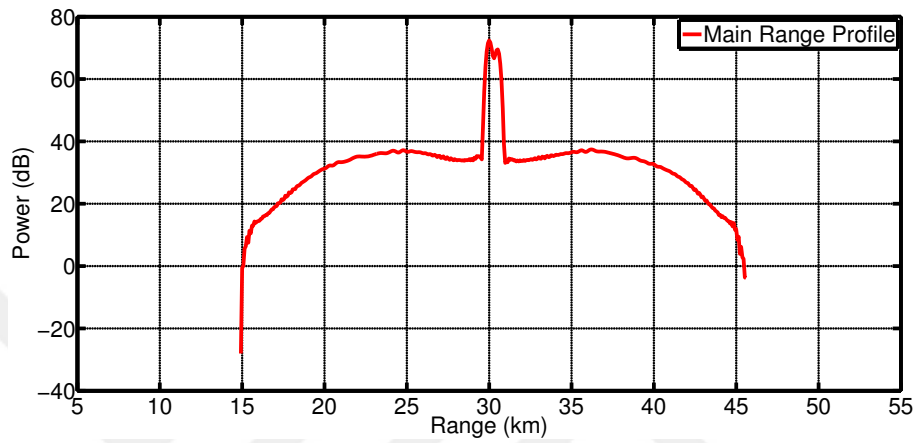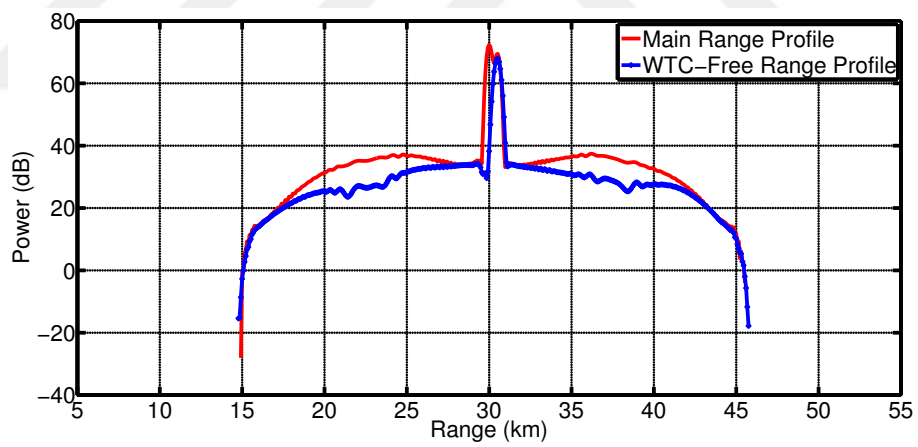
Figure 4.12 : WTC mitigation results for Scenario 1: a) Main range profile, b) Comparison of main and WTC-free range profiles.

(a)

(b)

Figure 4.13 : WTC mitigation results for Scenario 2: a) Main range profile, b)
Comparison of main and WTC-free range profiles.

5. INVESTIGATION OF WIND TURBINE EFFECTS ON RADAR TRACKING AND A MITIGATION APPROACH

It was clearly demonstrated in Chapter 4 through various simulations that, WTs might cause quite different and unpredictable detect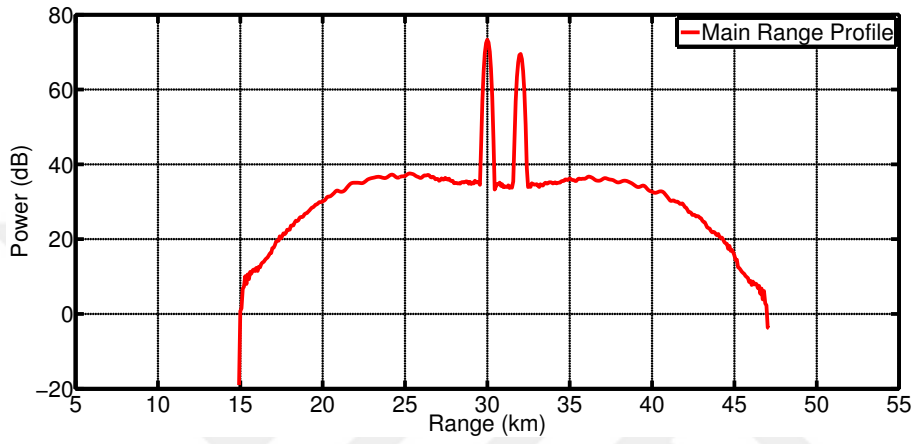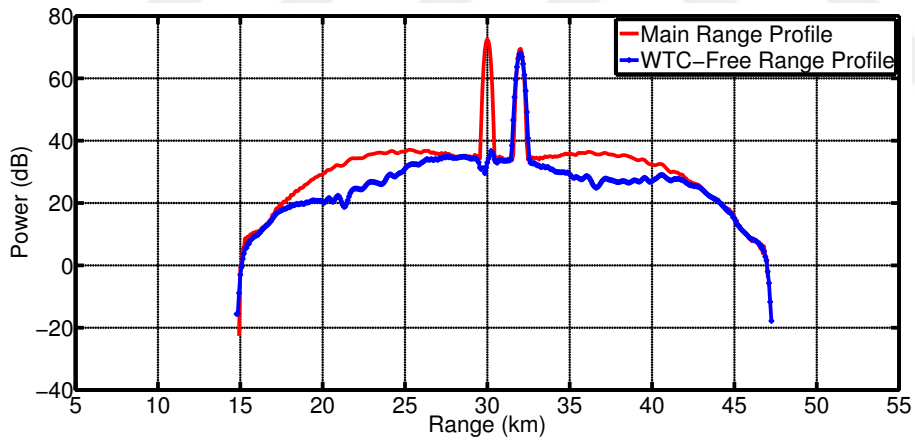ion characteristics in radar systems because of their structural, motional or orientation parameters. Sizes of the WTs, blade length, tower height, rotation RPM, and instantaneous rotation and yaw angles make the WTs such complicated and problematic objects in terms of the radar systems. When considering the WF case with multiple WTs, detection behavior of a WT in the WF is subject to a new challenge: detection shadowing. This occurs due to other WTs and/or GTs which are closely settled and raising up the average CFAR threshold in the detection stage.

The detection shadowing phenomenon and its complication in the detection of a WT is pointed out in Figure 5.1. In this figure, simulation results related to the detections (in range axis) of four WTs and a GT which are located in the same azimuthal sector are given for three radar scan-time instances. It is clearly observed from the figure that the CFAR threshold becomes higher in the vicinity of closely-located WTs, and detections of different WTs occur in different scan-time instances due to the time-variable scattering characteristics. Furthermore, it could be inferred that, detection of the GT would be affected by detection shadowing while passing close to the WTs. In addition to the detection shadowing effect, GTs' detection might be also adversely effectd in the case of being under SCV due to the strong reflections caused by WTs.

Since the WTs' and GTs' detections have random-like nature, one could expect from the radar tracking unit to experience various tracking events for a WF area in different time instances. Those events which will be investigated througout the following sections might arise in the form of false track generation and seduction or breakage of the GT tracks [61].
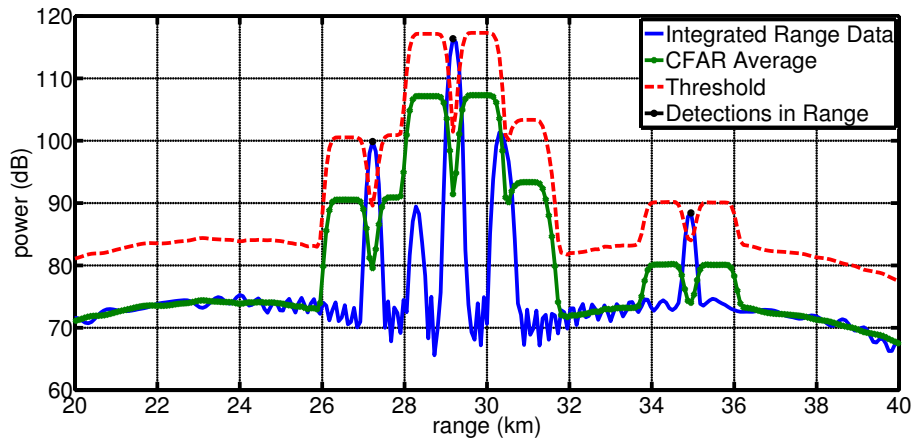
(a)
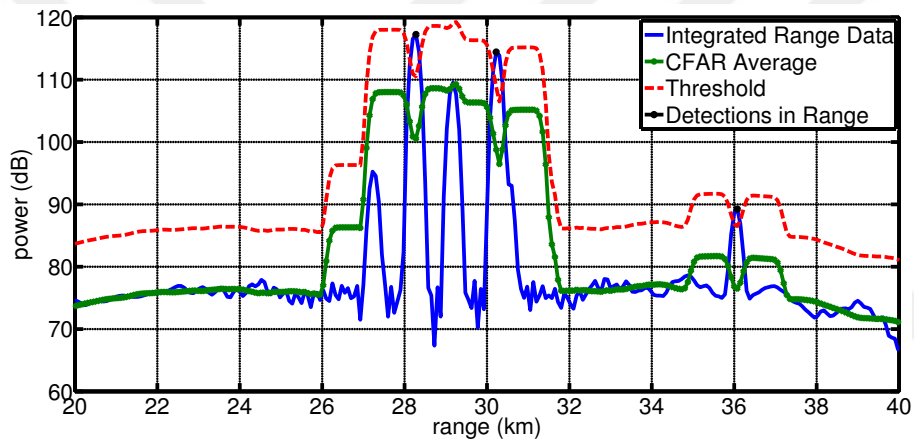
(b)
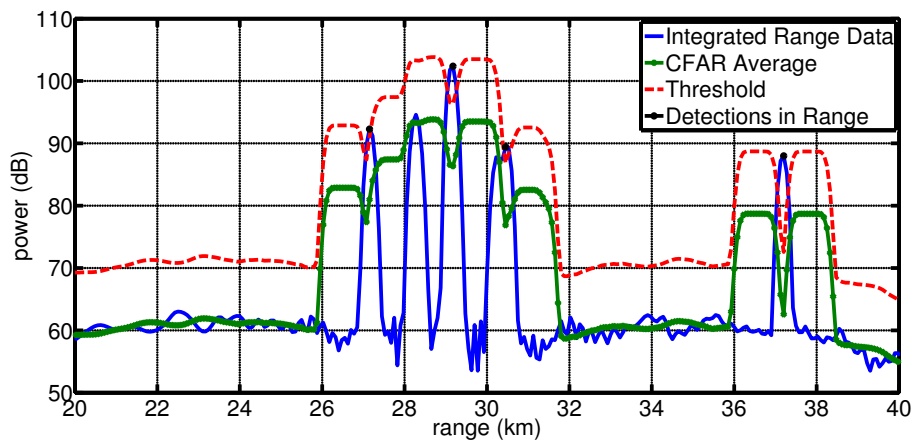
(c)

Figure 5.1 : Detection shadowing phenomenon in: a) Radar scan 1, b) Radar scan 2, b) Radar scan 3.

5.1 Wind Farm Effects on Radar Multiple Target Tracking

By paying careful attention on scattering and detection characteristics of the WFs, one could easily realize that the WFs have the ability to cause deteriorating effects on radar MTT performance through some WF-based phenomena such as

- detection shadowing of WTs or GTs,

- detection suppression of rotational blades or moving GTs due to the domination of radar sub-clutter visibility by stationary WT towers,

- disassociation between the tracks of the WTs and GTs.

WF-based deterioration level is highly dependent on lots of scenario parameters related to the WFs, GTs and the radar systems. In this chapter, effects of some major portion of these parameters such as the WT yaw angle, WF settlement, GT type and the threshold of the tracking velocity filter are analyzed. Furthermore, MTT analyses are performed for the cases in which the MTT procedure is based on GNN or PDA methods in order to provide performance comparisons of these methods in the vicinity of WFs.

5.1.1 MTT simulation initials

In order to investigate WF-based deteriorations in the MTT performance of radar systems, PDR processing scheme is employed with the turbine model whose parameters are summarized in the previous chapter together with the radar and GT models introduced below. According to [17], 2-D surveillance or ATC radars are crucially affected by WTs due to employing single and broad vertical beam-widths. Moreover, in 3-D radar systems, those beams that illuminate the WTs are affected. Therefore, in order to simulate the WT effects on the tracking performance of severely-affected radar systems, a typical 2-D air surveillance radar system operating in S-band is considered. The operational parameters of the radar system are listed in Table 5.1.

Different GTs might have quite different scattering properties that determine their detectability in the radar systems. In the simulations, glider and jet-type target models are used to investigate the WF effects on different GTs' tracking on the radar system. The employed GT models and their scattering patterns in xy-plane are depicted in

Table 5.1 : Operational parameters of radar system.

Radar Parameters	Value	Unit
Frequency	3	GHz
Chirp Bandwidth	2	MHz
Sampling Frequency	3	MHz
PRF	2000	1/s
Chirp Length	100	μs
Number of Integrated Pulses	25	-
MTI Filter Type	3 Pulse Canceller	-
FFT Length	256	-
CFAR Window Size	29	-
CFAR Guard Region Size	5	-
Scan time	5	s
Horizontal Beam Width	1	Degree
Sub-clutter Visibility	35	dB

Figure 5.2. It can be inferred from the figure that the jet-type aircraft presents stronger scattering characteristics than the glider according to the RCS values which are evaluated for the elevation angle interval $[0° - 90°]$ and the azimuthal angle interval $[0° - 360°]$.
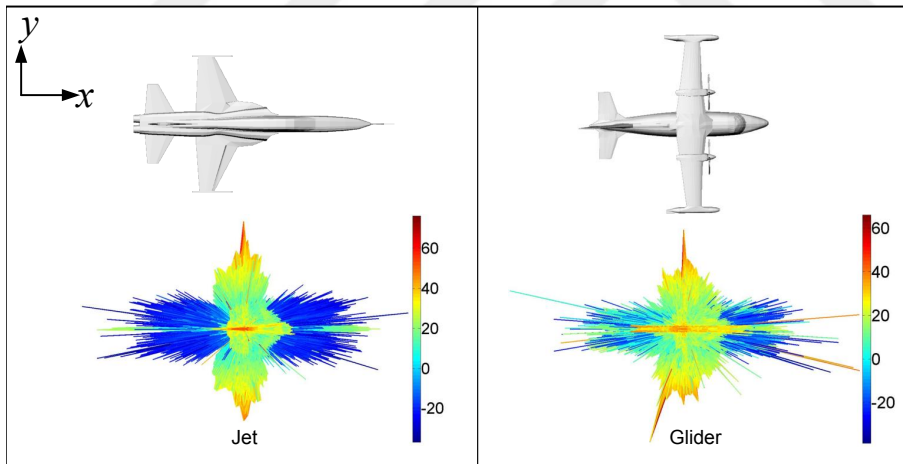
Figure 5.2 : GT models and scattering patterns for Jet and Glider.

To be consistent with the operational parameters of the chosen radar model, some slight changes are made in the PDR processing scheme. Processing of raw data includes pulse compression (matched-filtering), moving target indicator (MTI) filtering, Doppler processing via $256-$length Fast Fourier Transform followed by non-coherent integration of 25 pulses and finally cell-averaging CFAR detection. Note that, at the CFAR detection stage, a threshold is used in order to regulate the false

alarm control and is evaluated by the summation of the CFAR average and a margin of 12 dB that is selected to keep the probability of false alarm at about 10^{-6}.

In terms of the MTT unit of the processing scheme, coordinates of the detections are evaluated in polar space and then converted to Cartesian space before tracking processing. Moreover, targets are assumed to move according to constant-velocity model. When initiating the tracking filters, the variance of the process noise which is assumed to be caused by accelerative target motion is set as $q_x = q_y = 1$ (Km/s^2)^2 while the standard deviation of the measurement noise is predefined as $\sigma_x = \sigma_y = 100$ m. At the track initiation stage, logic-based initiation method is used. Hence, three interrelated detections are required to constitute a confirmed track. Similarly, coasted tracks are broken and deleted in the case of lacking three related detections.

5.1.2 MTT simulation results

For the simulations performed in this section, first three WF configurations of those listed in Table 5.2 are used, and the radar system is settled as (0 m, 0 m, variable altitude) on Cartesian-plane. Simulations, whose parameters are listed in Table 5.3, are run for 40 radar-scan instances, and some useful statistics such as total number of tracks, false tracks, and probability of detection (PD) of the GT track over WF area are recorded. The initial position of the GTs coursing in the radial route that are considered in the scenarios is (35000 m, 35000 m, 1750 m). Additionally, the gradient per receiver position index in x and y axes is predefined as (-160 m, -160 m). PD of the GT tracks is calculated using mid 20 radar-scan results corresponding to the GT locations that are close to the WF as in [19]

$$PD = \frac{N_{hit}}{N_{hit} + N_{miss}} \times 100 \qquad (5.1)$$

where N_{hit} and N_{miss} denote the total assigned and missed detections, respectively. Cumulative detection and track signatures for all radar-scan instances are depicted in the figures for each simulation scenario. In the figures, red dots represent the detection signatures, blue squared markers denote the track signature of the GT, and the green circled markers denote the false tracks caused by the WTs.

Table 5.2 : WF configurations.

WT ID	WF Configuration 1 (m)	WF Configuration 2 (m)	WF Configuration 3 (m)	WF Configuration 4 (m)
T1	(20000,20000,380)	(20000,20000,380)	(20000,20000,380)	(20000,20000,380)
T2	(22314,19794,388)	(22754,23496,338)	(21216,20944,304)	(20210,19828,310)
T3	(18656,20104,376)	(18750,23726,438)	(20396,21240,298)	(19884,19766,350)
T4	(20894,20620,358)	(24990,23166,288)	(20140,19334,470)	(19778,20154,460)
T5	(22438,19336,286)	(19308,17368,448)	(18972,21394,474)	(21683,18161,380)
T6	(22066,21925,438)	(16228,18864,462)	(19956,21370,440)	(21893,18287,290)
T7	(18808,17992,346)	(20906,16822,442)	(19764,18924,462)	(21919,17959,344)
T8	(18182,20898,424)	(24858,17610,368)	(21046,18606,466)	(21595,18385,474)
T9	(20768,18032,378)	(16846,17252,418)	(20772,20536,428)	(18161,21683,380)
T10	(21074,21394,460)	(22688,23750,332)	(20466,19676,314)	(18003,21489,382)
T11	(19170,21954,418)	(15440,24856,348)	(18594,20618,334)	(18327,21479,294)
T12	(17652,18488,428)	(15566,21730,290)	(18790,18638,444)	(17949,21887,454)
T13	(20588,20548,450)	(21508,20648,326)	(19450,20584,470)	(22687,22687,380)
T14	(20382,21526,316)	(20300,21268,382)	(19816,18602,356)	(22887,22899,416)
T15	(21932,18698,284)	(18736,22016,402)	(20884,20796,316)	(22867,22491,286)
T16	(18338,19948,474)	(15928,18072,412)	(20464,20538,312)	(22577,22895,466)
T17	(20002,21062,374)	(18844,15284,294)	(20254,19520,324)	(24423,20806,380)
T18	(20908,17798,288)	(17130,17918,424)	(19264,20752,380)	(24203,21010,386)
T19	(20108,17856,298)	(22150,22050,352)	(21172,20596,470)	(24639,20998,312)
T20	(21586,21590,424)	(18578,20464,468)	(21172,20596,470)	(24639,20998,312)
T21	(20744,22364,440)	(16108,19446,452)	(21022,19272,330)	(20806,24423,380)
T22	(19660,19768,444)	(17232,15354,306)	(19088,19548,330)	(20594,24643,320)
T23	(18164,17916,314)	(17540,18024,426)	(19918,20348,350)	(20582,24187,360)
T24	(21656,19454,440)	(24752,21376,346)	(20254,20992,388)	(20892,24181,318)
T25	(19496,17802,384)	(19804,19206,460)	(19356,21250,430)	(25374,25374,380)
T26	(20784,19582,404)	(19248,20720,370)	(19640,20760,392)	(25224,25614,442)
T27	(19658,18958,282)	(20828,24512,358)	(19288,20304,410)	(25620,25374,310)
T28	(18334,22420,300)	(24864,20580,436)	(19186,18750,462)	(25200,25186,414)
T29	(18490,19362,376)	(18784,15882,432)	(20976,18956,386)	(27162,23451,380)
T30	(22258,19196,464)	(18530,16994,322)	(18734,21488,368)	(27370,23257,452)

Table 5.3 : MTT simulation parameters.

Scenario ID	Radar Altitude (m)	GT Type	GT Elevation (m)	GT Route	GT Velocity ()m/s)	WTs' Yaw Angle (North Referenced) (°)	Min. Track Velocity (m/s)	WF Config. ID
S1	1500	Glider	1750	Radial	225	140	0	1
S2	1500	Glider	1750	Radial	225	190	0	1
S3	1500	Jet	1750	Radial	225	140	0	1
S4	2500	Glider	1750	Radial	225	190	50	1
S5	1500	Glider	1750	Radial	225	140	0	2
S6	1500	Glider	1750	Radial	225	140	0	3

Table 5.4 : MTT simulation parameters for the novel WF settlement case.

R_{sd}	N_{CFAR}	Δr	D_{SWF}	θ_{hbw}	N_{hb}	R_{SWF} For First SWF
1500 m	24	75 m	500 m	1°	1	20000 m

Simulation results of six different scenarios which are obtained through GNN association procedure are demonstrated in Figure 5.3 and Figure 5.4. Most of the deteriorating WF effects on radar MTT such as false track occurrence as well as seduction and breakage of GT track could be observed from Figure 5.3a that presents the result for scenario S1. Due to the higher scattering levels of the WTs and the WF-based detection and tracking phenomena, it could be easily inferred from the figure that the flight of the glider would be unsecured in case of such a scenario. WF-based deteriorating effects occurred in this scenario are highly dependent on the scattering and detection characteristics of the WTs and the GTs. For scenario S2 whose result is depicted in Figure 5.3b, lower scattering levels of the WT blades due to the higher yaw angle when compared to scenario S1 are resulted in reduced-rate false tracks and more robust GT flight. Providing relatively higher scattering levels of the GTs during their flight would increase the probability of establishing robust tracks as exemplified in scenario S3. Unlike the scenario S1, by operating a target type with higher reflective characteristics (jet), GTs' scattering level could be guaranteed to be relatively higher when compared to the WTs, therefore, secured GT tracks are established. Result for the related scenario is given in Figure 5.3c. Radar systems generally employ track velocity filters to eliminate slowly moving or irrelevant targets. Benefits of using such a filter could be observed through examining the scenario S4. When comparing the results of scenario S4 in Figure 5.4a (where the minimum track velocity is set as 50 m/s) with the previous scenarios, it is clearly observed that the stationary false tracks are eliminated. Conversely, appeared non-stationary false tracks demonstrate the weakness of the track velocity filters on eliminating WF-based adverse effects. WT density in a WF is another important parameter in terms of the impact level of WFs on GTs' tracking performance. For a given number of WTs, due to the intense scattering characteristics of closely-spaced multiple WTs, detection probability of the GTs would degrade severely over the denser WFs than the larger ones where the WTs are settled sparsely. In spite of the excess in false track rate, success in the tracking performance of the glider over larger WF settlement could be clearly observed by examining Figure 5.4b and Figure 5.4c related to scenarios S5 and S6, respectively.
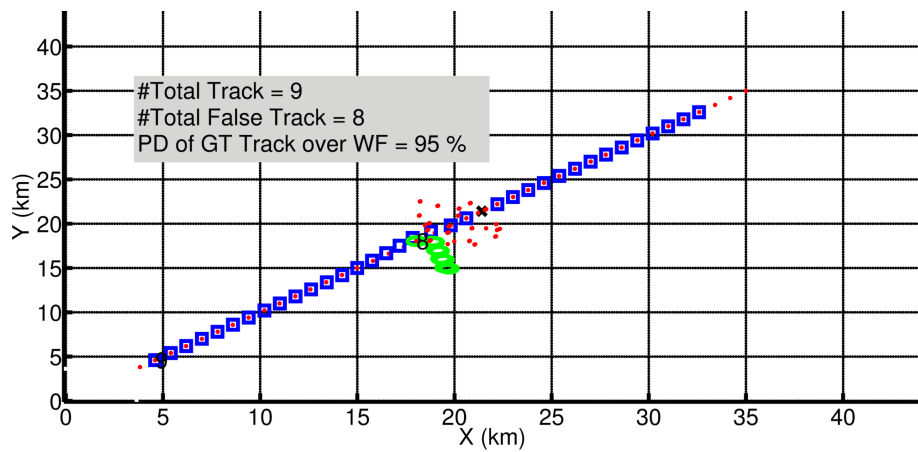
In Figure 5.5 and Figure 5.6, simulation results corresponding to the PDA tracking method are presented for the same scenarios considered for the GNN case. By carefully
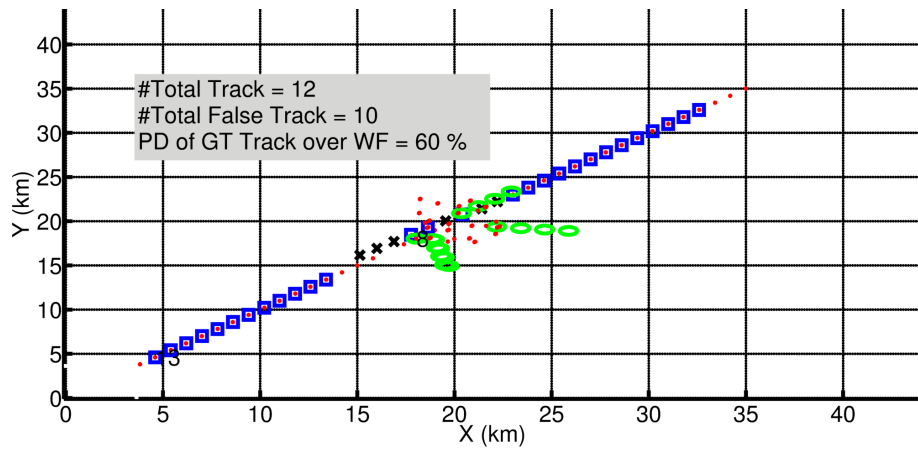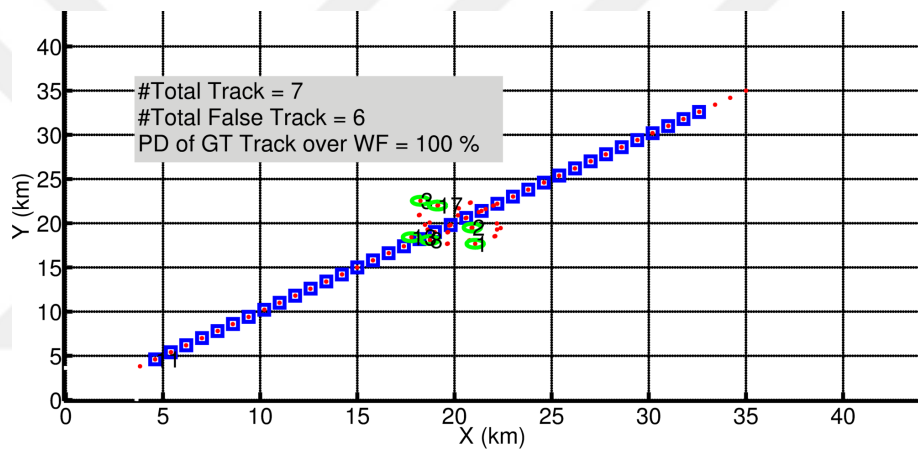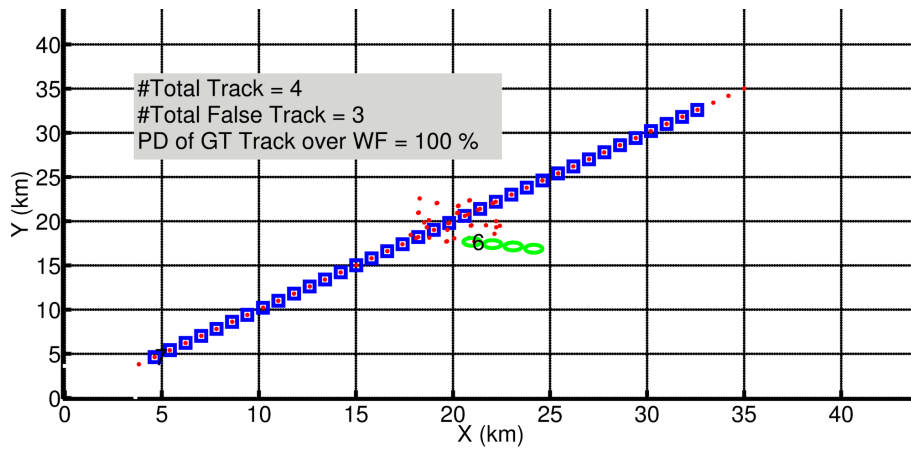
Figure 5.3 : MTT simulation results related to GNN method for the scenarios: a) S1, b) S2, c) S3.

Figure 5.4 : MTT simulation results related to GNN method for the scenarios: a) S4, b) S5, c) S6.

examining the results and comparing with the ones related to the GNN, decreased rate in the deteriorating effects of the WFs on the MTT procedure could be easily realized. Simulation results especially for scenarios S1, S2, S3 and S4 point out that using the PDA tracking method would effectively decrease the rates of the occurrence of the WF-based false tracks. Results for these scenarios are given in Figure 5.5a, Figure 5.5b, Figure 5.5c and Figure 5.6a, respectively. Additionally, when analyzing the result of the scenario given in Figure 5.6c and comparing with the one given in Figure 5.4c, PDA method is seen to be more robust in terms of breakage of the GTs' tracks. On the other hand, simulation results presented in Figure 5.5a and Figure 5.6b demonstrate that the PDA method would be also vulnerable to significant WF effects such as breakage of GTs' tracks and non-stationary false tracks.

5.2 Wind Farm Design Approach for Mitigating Adverse Wind Farm Effects on Radar Tracking

In the previous section, effects of the WFs on radar MTT are demonstrated through several scenarios for GNN- and PDA-type association procedures. Simulation results indicate that the WF effects on radar tracking operation are scenario-dependent, and radar systems employing GNN or PDA methods both have the possibility to face degradations in the tracking performance of the GTs.

The related literature includes some efforts [20], [30], [31] that proposed similar approaches in order to improve the detection and tracking performance of GTs in the vicinity of WFs. These works proposed excluding WTs in CFAR processing and several other modifications in radar systems to minimize WT effects. In the case of denser WF areas containing a great number of WTs, masking out the WT locations is likely to cause larger radar blind zones where the detection of the GTs would also be suppressed. In this section, an alternative proposal that focuses on configuring WT locations in order to minimize WF-based degrading effects on tracking operation is introduced. The main focus of the proposed method is to increase the detection probability of GTs while passing over WFs. Schematic presentation of the proposed WF design approach is given in Figure 5.7. According to this approach, WFs should be divided into many sub-WFs (SWFs) which are separated from each other with the consideration of a predefined criteria. SWF formation and separation criteria
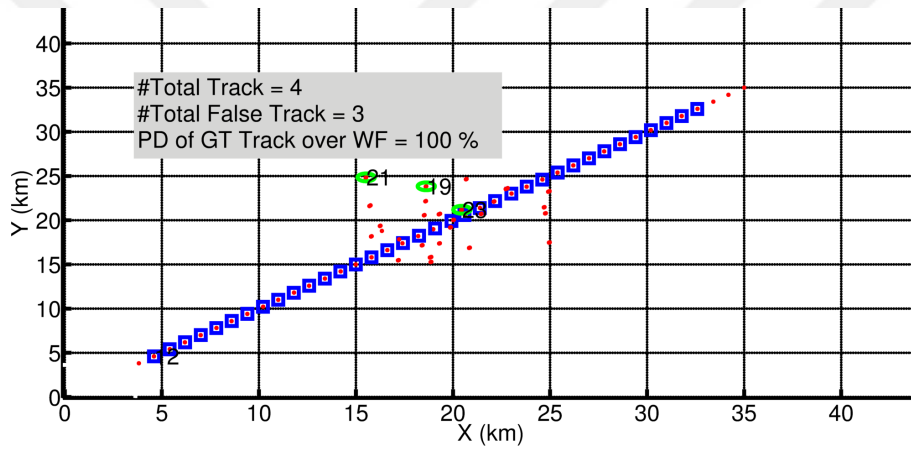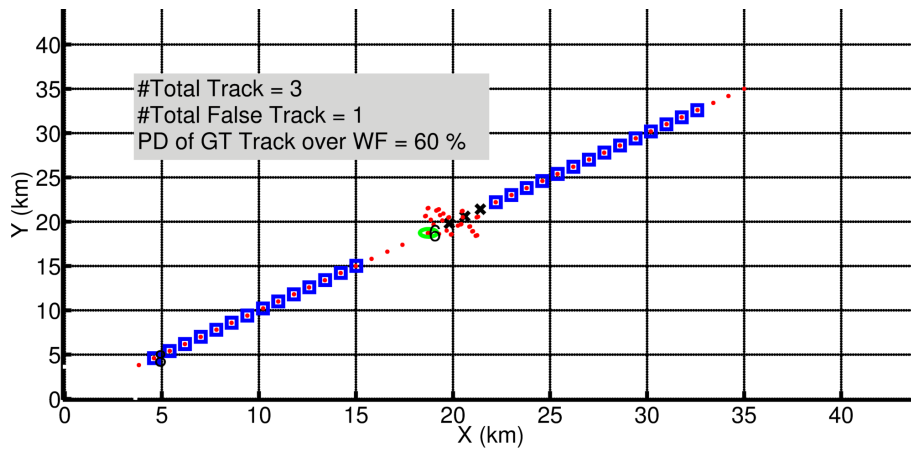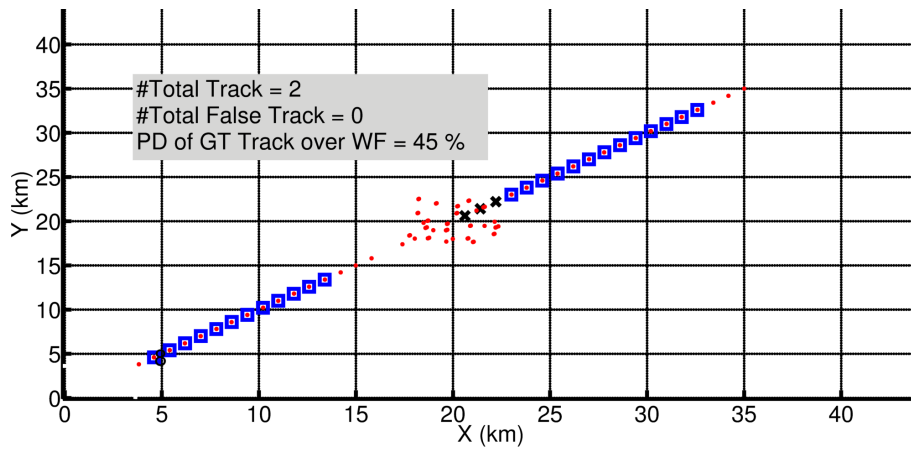
(a)
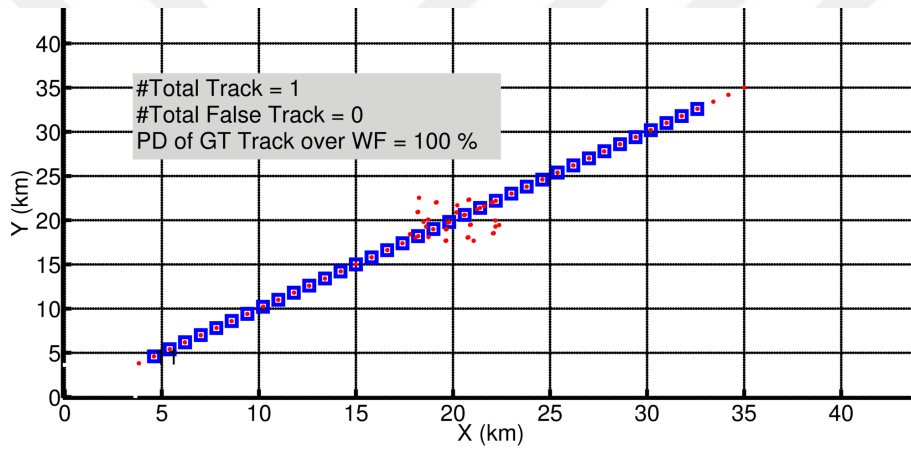
(b)
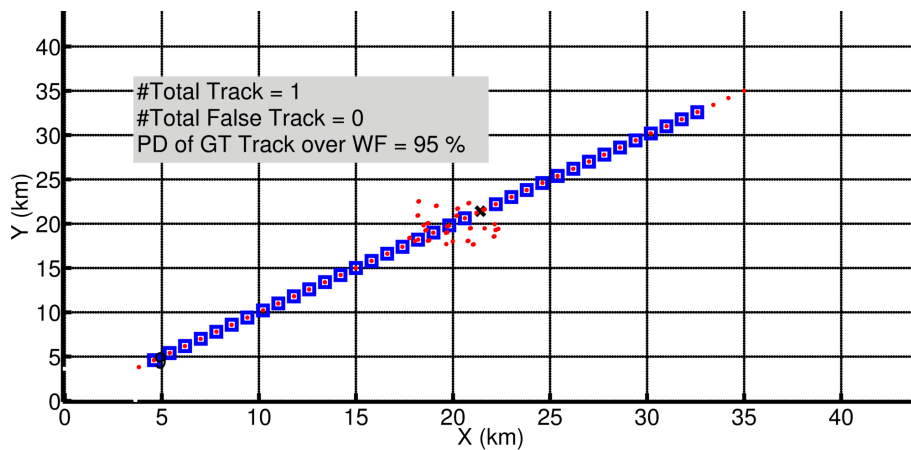
(c)

Figure 5.5 : MTT simulation results related to PDA method for the scenarios: a) S1, b) S2, c) S3.
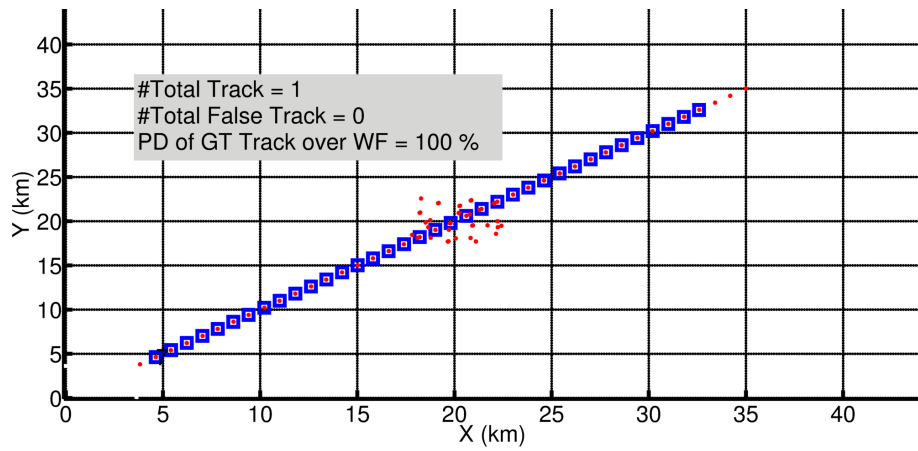
(a)
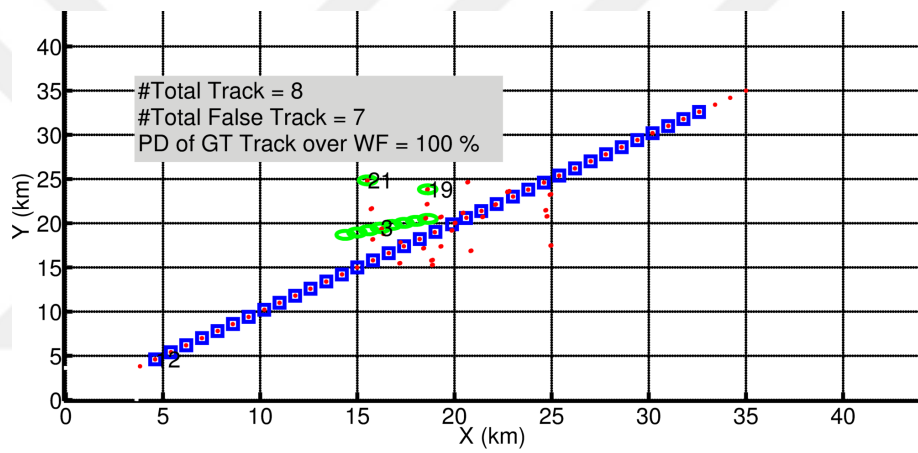
(b)
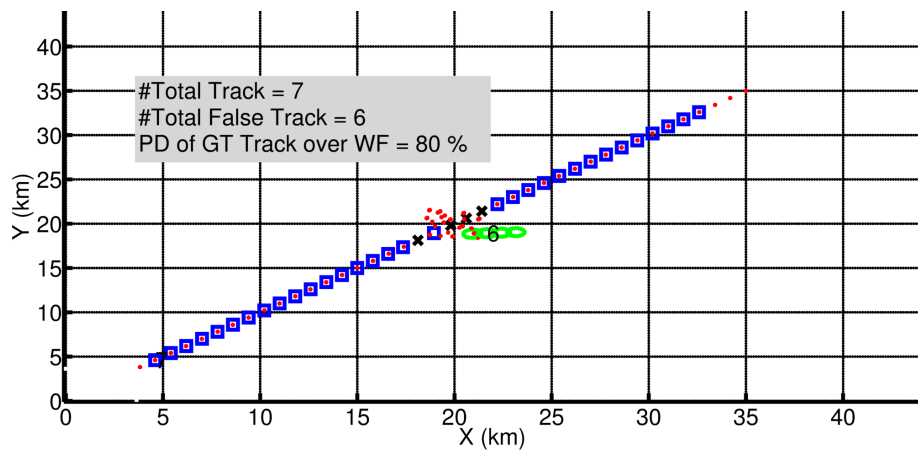
(c)

Figure 5.6 : MTT simulation results related to PDA method for the scenarios: a) S4, b) S5, c) S6.

91

are prepared by taking the WF-based deteriorating effects, radar parameters and GT characteristics into account as explained in detail below.
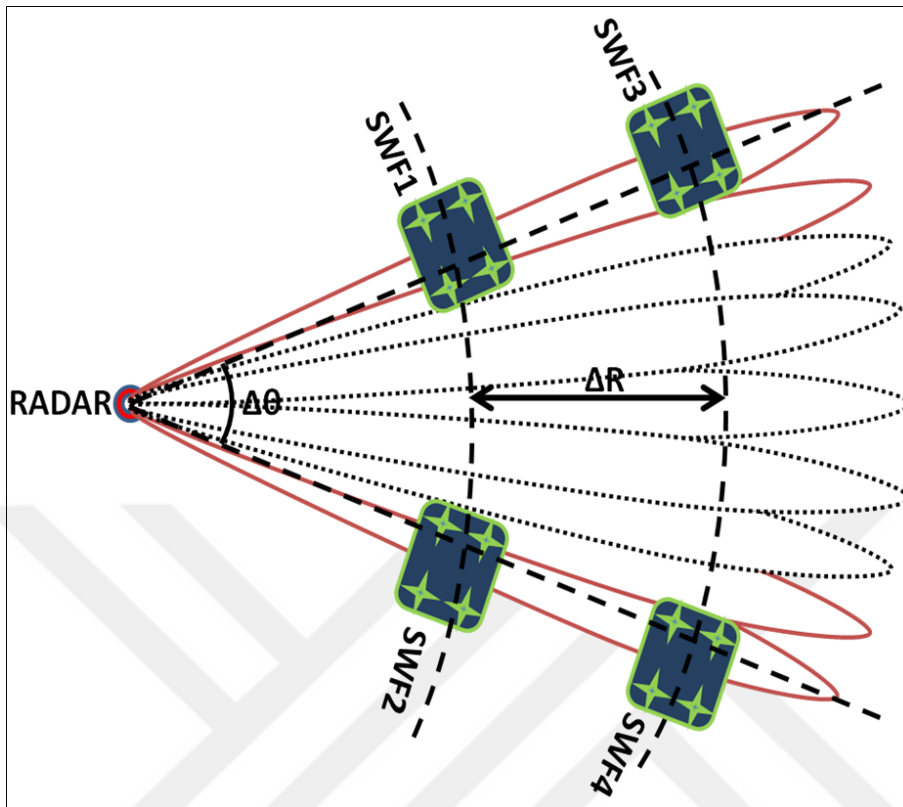
Figure 5.7 : Schematic representation of novel WF design approach.

Determining the size of SWFs as well as the number of WTs residing on a SWF is the initial point to be considered within the WF design. In order to minimize the interaction duration between the WTs and the GTs in terms of radar detection process, sizes of the SWFs should be as small as possible. Additionally, generation of false tracks in a SWF could be prevented by properly defining the number of the WTs. With the consideration of WT dimensions and the track initiation logic, SWFs are designed as to include four WTs which are located in a squared area of 500 m widths in both directions and with a 250 m displacement from each other, as seen in Figure 5.7. In the range and azimuthal directions, SWFs are located by relying on the spacing in terms of the radial and azimuthal resolutions (ΔR and $\Delta \theta$), respectively, in order to provide safe regions where the GTs would be detected at least during one radar scan without experiencing adverse WT effects.

Range intervals could be evaluated by using the SWF size, CFAR averaging cell size and a guard zone which is a distance interval where the GT could be securely detected without WF interference at least for one radar scan time as

$$\Delta R = R_{sd} + N_{CFAR}.\Delta r + D_{SWF} \qquad (5.2)$$

where R_{sd} is the guard zone that is calculated as the product of target mean-velocity and radar scan-time, N_{CFAR} is the CFAR averaging cell size whose half of the contribution is related to one SWF, Δr is the radar range resolution and finally D_{SWF} is the edge length of a SWF area. In addition to the range interval implementation, range side-lobe suppression should also be applied as suggested in [31], in order to reduce the side-lobes of matched-filtered WT signals to noise level. In the azimuthal direction, angular spacing is evaluated by using the antenna horizontal beam-width, SWF size and the guard zone as provided in equation 5.3.

$$\Delta\theta = \left(\frac{R_{sd} + D_{SWF}}{R_{SWF}.\sin(\theta_{hbw})} + N_{hb} \right).\theta_{hbw} \qquad (5.3)$$

Here, R_{SWF} is the distance of the center of SWF to the radar system, N_{hb} is the additional factor for horizontal spacing in terms of horizontal beam-width for safe region adjustment and θ_{hbw} is the antenna horizontal beam-width. As seen in equation 5.3, number of horizontal beams which are the dashed ones in Figure 5.7 are multiplied with antenna horizontal beam-width to calculate the angular spacing. In addition to the SWF design and determination of radial and azimuthal spacing, some part of the tracking logic related to the track initiation and coasted state settings could also be modified. By using the procedure introduced here, WFs consisting of numerous WTs could be configured as a combination of many SWFs in order to minimize the deteriorating effects of WFs and to establish secured GT tracks. Note that the design approach presumes that all WTs are in the electromagnetic LoS of the radar system. Therefore, there would be no need to design such a configuration for the WF areas that are not in the electromagnetic LoS of the radar systems.

In order to examine the performance of proposed WF design in radar MTT, scenario S1 is considered for two GT routes with WF Configuration 4 given in Table 5.2 (which is determined according to the novel design approach). Simulation parameters used for the WF design are listed in Table 5.4. Simulations are performed for the GNN- and PDA-type tracking methods, and the tracking performances are depicted in Figure 5.8 for both cases. In Figure 5.8, dashed circles symbolize the SWF locations. Comparing the results depicted in Figure 5.8a to those in Figure 5.3a and Figure

5.5a, respectively, would evidently point out the significant enhancement in the radar tracking performance. The results which are identical for the GNN and PDA methods show that, together with the detection losses for only SWF locations as expected, the new WF design paves the way of more robust GT tracks over WF areas. Furthermore, the considerable decrease in false track rate is seen to be another improvement. Due to passing over many possible SWFs in radial direction, the scenario depicted in Figure 5.8a could be considered as the worst case for the GTs where they are subject of WF interference for longer times during their flight. For the GTs' cross-radial flight route with respect to the radar, simulation results are expected to be similar with the ones given in Figure 5.8a depending on the similarity in the configuration of GTs' flight path and SWF locations. Therefore, another scenario is configured in which the GT experiences WF interference for shorter instances during its flight and, the related simulation result is presented in Figure 5.8b. From Figure 5.8b, increased tracking performance over the WF area could be easily observed according as the better flight path for the GT compared to the one handled in radial flight path scenario. The promising results of the simulations performed for different scenarios clearly indicate the efficiency of the proposed WF design approach.
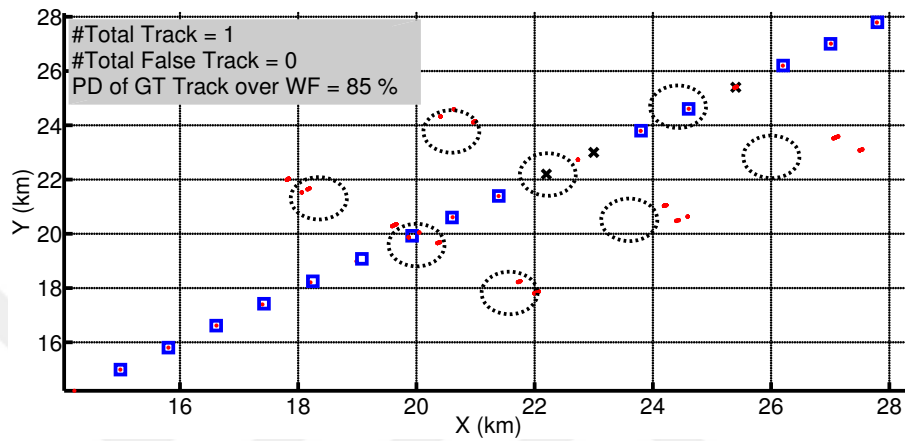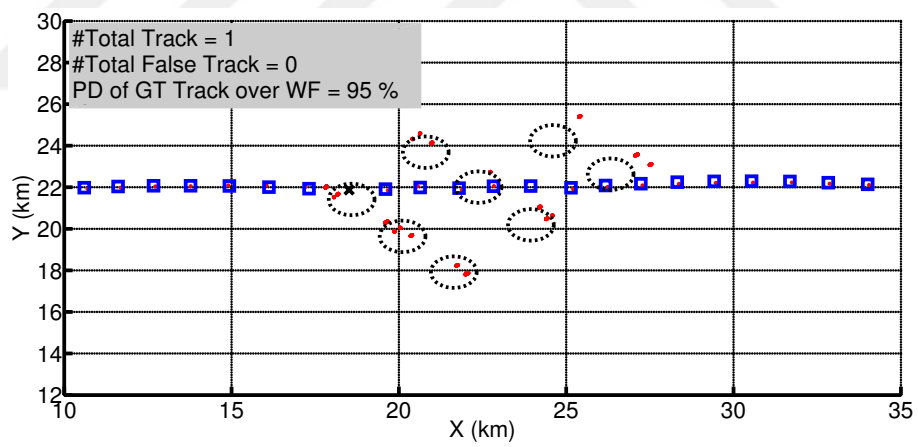
Figure 5.8 : GNN/PDA simulation results for the novel WF approach for the routes
a) Radial, b) Parallel to x-axis.

6. INVESTIGATION OF WIND TURBINE EFFECTS ON RADAR IMAGING

In this chapter, deteriorating WF effects on radar imaging is investigated by using the SAR simulation framework introduced in Chapter 2 and the wind turbine signal model proposed in Chapter 3. WTs and WFs could be problematic objects in terms of radar imaging due to their complicated scattering and motional characteristics. With their large reflective structure together with variable motion in two different rotation of plane, they have the ability to cause some problems such as suppression of real targets or generation of ghost targets via producing overspread target signature along cross-range dimension [62], [63]. Therefore, the topic under consideration is worthwhile to research and handled throughout this chapter.

6.1 Problem Background

For the sake of simplicity, theoretical examination of WFs' deteriorations on SAR imaging is investigated through dealing with the problem by considering the single WT case. Investigations over adverse WF effects can be performed straightforward. First of all, stripmap mode SAR imaging geometry depicted in Figure 6.1 is taken into account. According to that geometry, an aircraft (as a SAR platform) moves with the instantaneous positions in Cartesian coordinates as (Vt (m), 0 (m), Z_p (m)) where V is the platform velocity and t indicates the time. Moreover, a WT with the rotational velocity Ω_t and a yaw angle θ_t is settled to the center of an imaged region. The distance (from the origin) and the altitude values of the WT is defined as $R0$ and $Z_{WT} = 0$ (m), respectively.

In order to accomplish SAR imaging of the scenario depicted in Figure 6.1, it is necessary to calculate time-varying RCS ($\sigma(t)$) and radial distance $r(t)$ values of all scatterer points according to the implemented SAR simulation framework introduced in Chapter 2. Here, with the consideration of proposed canonical WT model, $N + 3M$ RCS and radial distance calculations are needed for each platform position.
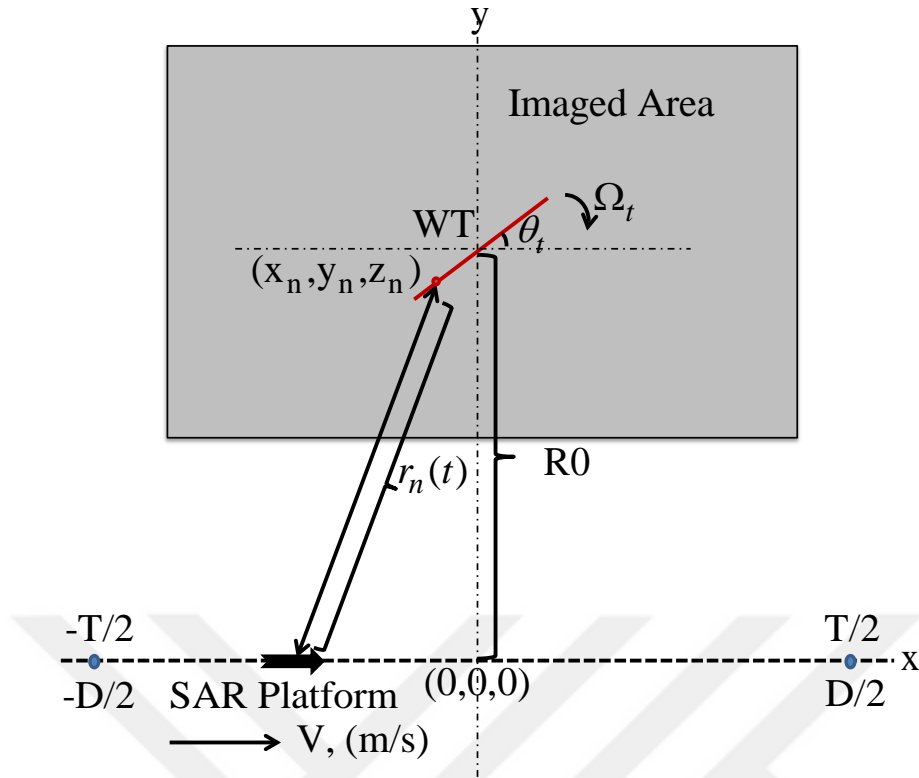
Figure 6.1 : SAR problem geometry (top view).

It was mentioned several times and analyzed in detail in Chapter 3 that, WTs might cause strong reflections especially due to their high reflective tower parts. This can desensitize targets with weaker scattering characteristics. For this reason, reanalysis on the RCS calculations of the WTs is unnecessary in this section. However, actually what is mainly interesting and deteriorating about WTs is their parts' time-varying radial distance in terms of the SAR imaging. Those calculations affect the phase (relatingly the Doppler information) of the SAR signal which is exploited to construct cross-range values of detected targets. Time-varying distance of a scatterer differs for the cases of locating on the tower or the blade of the WT. The distance examinations are given in the following subsections.

6.1.1 Time-varying distance of a scatterer on the WT tower

Tower is the stationary part of WTs, therefore, position of a cylindrical segment (as a point scatterer) on the tower does not change with the time. If we define the position of the segment as (x_t, y_t, z_t) in Cartesian coordinates, time-varying distance of the segment to the SAR platform becomes

$$r_{tp}(t) = \sqrt{(x_t - Vt)^2 + (y_t)^2 + (z_t - Z_p)^2} = \sqrt{x_t^2 + y_t^2 + (z_t - Z_p)^2 - 2x_t Vt + V^2 t^2}.$$

(6.1)

With a definition as $R_{tp} = \sqrt{x_t^2 + y_t^2 + (z_t - Z_p)^2}$ which is constant during the platform flight time and performing derivations on equation 6.1 similar to the ones considered in Chapter 2, the distance equation for the segment on WT tower can be rewritten as

$$r_{tp}(t) = R_{tp} - \left(\frac{Vtx_t}{R_{tp}}\right) + \left(\frac{V^2 t^2}{2R_{tp}}\right).$$

(6.2)

As was already mentioned, the first and third terms in the equation 6.2 can be compensated in SAR processors and therefore, with such radial distance characteristics, stationary tower segments generate a phase component in received signal as

$$\Phi(t) = -4\pi x_t V / \lambda R_{tp},$$

(6.3)

where λ denotes the signal wavelength. Derivative of that phase function results in the Doppler shift as provided in equation 6.4.

$$f_{Dt} = \frac{1}{2\pi} \frac{d(\Phi(t))}{dt} = 2x_t V / \lambda R_{tp}.$$

(6.4)

As can be inferred from that equation, scatterer points on the tower would reside on cross-range positions related to Doppler frequency they cause. We are familiar with the result reached for stationary tower segments since it is valid for any stationary targets to be imaged.

6.1.2 Time-varying distance of a scatterer on the WT blade

Apart from the ones located on WT tower, blades' segments could rotate on horizontal and rotational plane of rotations. According to the considered imaging geometry, the instantaneous position of a segment on a rotational blade could be defined in terms of the yaw angle (θ_{yaw}) which denotes the angle over $xy - plane$, and the rotation angle (θ_{rot}) that indicates the angle over $z - xy - plane$. If the height of the WT tower (distance from ground to the nacelle level) is Z_0 and and distance

of the blade segment from the nacelle is L_b, then the time-varying positions of that segment become as $(L_b cos(\theta_{yaw})sin(\Omega t), R0 + L_b sin(\theta_{yaw})sin(\Omega t), Z_0 + L_b cos(\theta_{yaw}))$ in Cartesian coordinates. Then the distance between the SAR sensor and the blade's segment can be expressed as given in equation 6.5.

$$r_{bp}(t) = R_{bp} + \left(\frac{L_b C_b}{R_{bp}}\right) + \left(\frac{V^2 t^2}{2R_{bp}}\right) \tag{6.5}$$

$$R_{bp} = L_b{}^2 + [R0^2 + (Z_0 - Z_p)^2] \tag{6.6}$$

$$C_b = R0sin(\theta_{yaw})sin(\Omega t) + (Z_0 - Z_p)cos(\Omega t) - Vtcos(\theta_{yaw})sin(\Omega t) \tag{6.7}$$

With a similiar process performed for the segment on the tower, Doppler frequency shift caused by the blade's segment could be derived as

$$f_{Db}(t) = \frac{2L_b}{R_{bp}}(cos(\Omega t)(R0sin(\theta_{yaw}) + Vtcos(\theta_{yaw})) - sin(\Omega t)((Z_0 - Z_p) + Vcos(\theta_{yaw}))).$$
$$\tag{6.8}$$

According to equation 6.8, each segment on WT blades have the ability to produce time-varing Doppler frequencies. Therefore, this will cause them to spread over multiple cross-range positions in SAR images. Thereby, in the case of having strong scattering characteristics, they might desensitize or suppress the targets located on the same cross-range position with the WTs.

6.2 Simulation Results

SAR imaging of a WF consisting of three WTs is performed for two different scenarios in the simulations. As a SAR sensor, an X band radar system which is operated in stripmap mode is employed. WF area imaging is realized by using the WT signal model and the simulation framework that are described previously. In order to investigate the adverse WT effects on radar imaging in terms of the scattering and Doppler characteristics, both of RCS and distance of individual segment on a WT is evaluated and contributed to the constructed SAR raw signal.

As was mentioned previously several times, WTs' scattering and Doppler characteristics are variable considerably depending on many factors such as the yaw angle, WTs' dimensions, material properties and so on. For this reason, investigations about each of those parameters are impossible, and only some exemplary scenarios as considered here.

Simulation parameters for two scenarios are summarized in Table 6.1. The difference between two scenarios is defined as the altitude value of the SAR sensor. Additional to the parameters given in the table, locations of the WTs are stated as (0 km, 0 km, 0 km), (1 km, 3 km, 0 km) and (-0.5 km, 3 km, 0 km) in terms of the range, cross-range and altitude, respectively.

Table 6.1 : Simulation parameters.

Simulation parameters	Value
SAR - Frequency	10 GHz
SAR - Range resolution	5 m
SAR - Cross-range resolution	5 m
SAR - $R0$	50 km
SAR - V (Platform velocity)	150 m/s
SAR - Antenna's cross-range length	0.2 m
SAR - LFM bandwidth	30 MHz
SAR - PRF	4.5 kHz
WTs - Tower height	80 m
WTs - Blade length	50 m
WTs - RPM	15
WTs - Initial rotation angle	0°
WT1 - Yaw angle	0°
WT2 - Yaw angle	45°
WT3 - Yaw angle	85°
Scenario 1 - Platform altitude	3000 m
Scenario 2 - Platform altitude	300 m

In Figure 6.2, SAR imaging results of the WF including 3 WTs are given for two different scenario cases. Figure 6.2a presents the result obtained for Scenario 1 for which the platform altitude is set as 3000 m. Variations about the scattering and Doppler characteristics of WTs are clearly demonstrated through the figure. According to the result, WT1 is seen to be the strongest scatterer among the WTs due to having lower yaw angle value for which the WTs generally present stronger RCS characteristics. It can be also inferred from the figure that WT1 is spread over multiple cross-range positions because of the Doppler band caused by the motion of blades.

When examining the figure in terms of the WT2, broader spread over cross-range due to higher yaw angle attracts the attention. Besides, weak scattering properties of WT2 decreased it's deterioration level in the image. Finally, despite having the highest yaw angle which might cause maximal deteriorations in terms of spreading over cross-range, WT3 is seen as a point target due to it's blades with scatterings scarcely any.
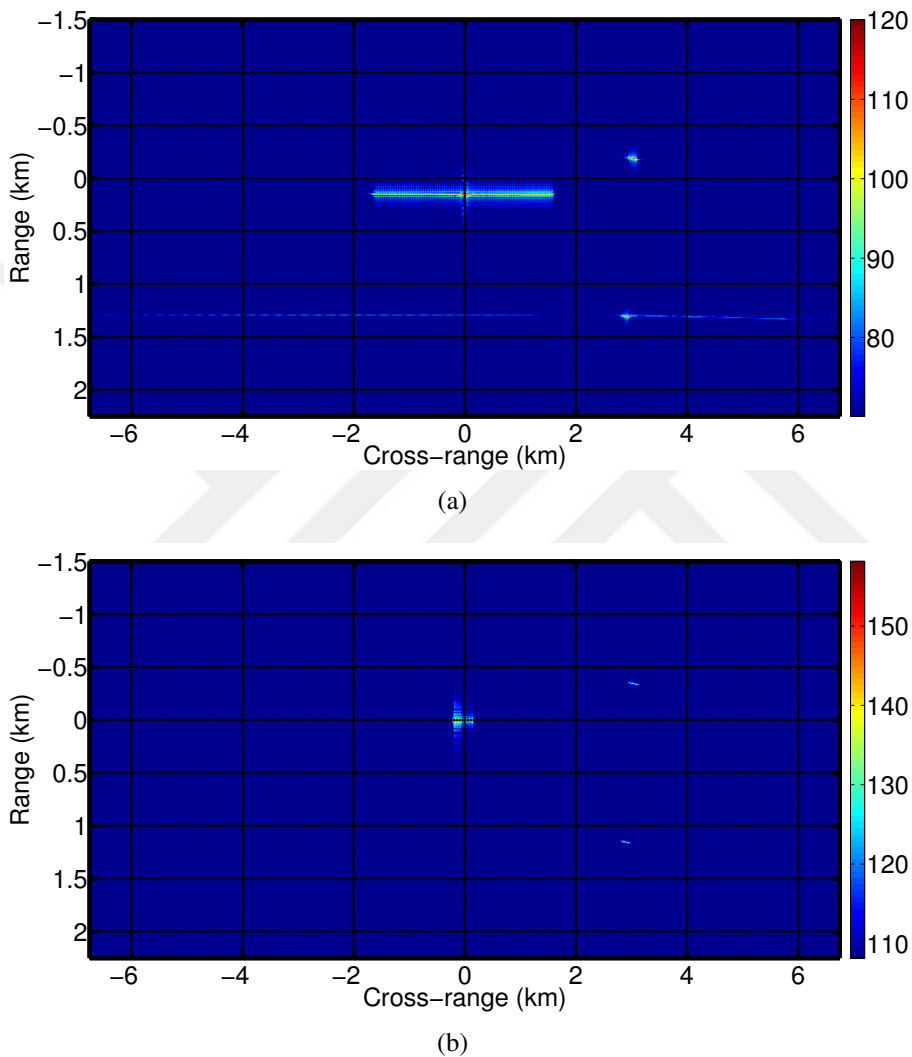
Figure 6.2 : SAR imaging results for a) Scenario 1, b) Scenario 2.

Simulation result of the Scenario 2 is demonstrated in Figure 6.2b. In this scenario, the radar is settled with an altitude value of 300 m. For the cases in which the radar and the WTs are in altitudes close to each other as in this scenario, great differences might occur between the scattering levels of the tower and the blades. This can make the WTs' blades desensitized and reduce the deterioration about spreading over cross-range positions. Consistency of those interpretations are proven through the

figure. It is clearly seen that all of three WTs exhibit nearly the stationary target signatures. It is also obvious from the scenario that, beside the WTs' blades, other targets that are in the same cross-range with the turbines have the risk of being desensitized depending on their scattering levels.

7. CONCLUSIONS AND RECOMMENDATIONS

Recent statistics on renewable energy area clearly denote that the wind farm (WF) installations are becoming widespread all over the world depending on the increasing clean energy necessities. They have been used as an electricity resource to meet energy demands in a variety of fields. Depending on the energy needs, wind farms might consist of wind turbines (WT) with variable quantities and physical structures. According to the literature related to the last decade, wind turbines have the possibility to violate radar systems' operation due to their structural and rotational characteristics. The WT-based violation might be seen in a great number of forms and vary with the WFs' and WTs' individual characteristics. Although the interaction between the radar systems and WTs/WFs have been investigated with a great effort, WT/WF-based degrading effects have not been fully characterized for all radar systems yet. In this dissertation, by developing a novel WT signal model, adverse effects of the WTs/WFs on the radar systems' detection, multiple target tracking (MTT) and imaging performances are investigated.

According to the investigation results about the WT effects on radar systems' detection performance;

- **WTs present unpredictable detection characteristics:** As demonstrated through theoretical simulations and experimental analyses, stationary and rotational parts of the WTs might have quite variational scattering levels for successive radar scans due to their varying aspects with respect to the radar system. In some aspects, it is possible for high reflective tower echoes to desensitize the ones produced by rotational blades. Additionally, their unsteady aspects due to the blades' rotation, WTs could also produce echoes with different Doppler shifts in consecutive scans. Therefore, such scattering and Doppler characteristics cause unsteady detection cases for radar systems.

- **WTs could desensitize or mask genuine target (GT) echoes:** With their huge structural properties, WTs that are in the LoS of the radar system generally produce echoes with high power levels. Obviously, this cause weaker genuine target echoes to be desensitized or masked during detection processing. Moreover, radar systems are likely to experience degradations in the detection performance of genuine targets passing over or close to a WF area.

- **It is possible to construct a wind turbine clutter (WTC) model by using the scattering levels of the WT parts:** Studies on the investigation of WTs' detection characteristics made possible to come up with a WTC model. To this model, by using the physical properties and yaw angle of a WT that are priorily assumed to be known, the detection behaviour of that WT could be estimated.

WTs' adverse effects on the MTT performance of radar systems are investigated in terms of variable WF configurations, different WT yaw angle values, track filter settings, different genuine target types and two types of association methods. The investigation results about the WT effects on radar systems' multiple target tracking performance state that;

- **WTs could cause generation of stationary and/or moving false tracks:** As an outcome of the WTs' unsteady detection characteristics, radar systems could experience stationary or moving false tracks. With the consideration of lower correlation between different WTs' detections in successive scans, the probability of the occurance of a moving false track is expected to be low. Additionally, these false tracks would occur for short time durations.

- **WTs could cause seduction or breakage of tracks related to GTs:** When GTs pass over or near to a WF area, its echoes might be desensitized or masked by WT echoes. Furthermore, their detections might be erroneously associated to the WT-based detections. As a result, MTT performance of the radar system on GTs' tracks would be deteriorated in the manner of track seduction and/or track breakage phenomena.

- **Both GNN and PDA association methods are vulnerable to adverse WT effects:** Radar system's MTT performance under WT effects is evaluated for both the GNN

and PDA type association cases. It can be easily concluded from the results for two association cases that the PDA method outperforms GNN. On the other hand, radar systems that use PDA for the association operation would also experience WT-based deteriorations.

WTs' degrading effects on radar imaging operation are examined through theoretical derivations and also simulations. The simulation results are seen to be consistent with the theoretical derivations and demonstrate that the rotational blades of the WTs might cause WT-based blurring and desensitization effects through cross-range dimension in SAR images. It can be clearly inferred from different results that these effects strongly depend on instantaneous aspects of the WTs.

Additional to the investigations, two mitigation approaches have also been introduced in order to reduce deteriorating WT effects in this dissertation. One of the approaches employ CLEAN algorithm to subtract WT-based echoes from radar raw data, and aims at mitigating WT effects at the radar detection stage. The other mitigation effort approaches the WT-based problems at the radar target tracking stage. In this context, a novel WF design is suggested in order to higher up radar detection and MTT performances for GT targets. The success of two mitigation approaches are presented through various simulations.

Consequently, deteriorating effects of WTs on detection, tracking and imaging operations of radar systems are examined throughout this dissertation. Moreover, in order to employ at the detection and tracking stages of PDR systems, two novel WTC mitigation approaches are proposed. The examinations, obtained results and also introduced mitigation procedures could be utilized for forming baselines and constituting frameworks in dealing with the WT problem.

REFERENCES

[1] **GWEC** (2015). *Global wind statistics 2014*, Technical Report, Global Wind Energy Council, Brussels, Belgium.

[2] **TWEA** (2015). *Turkish wind energy statistics report*, Technical Report, Turkish Wind Energy Association, Ankara, Turkey.

[3] **Url-1**, <www.ewea.org>, date retrieved 15.12.2015.

[4] **Url-2**, <http://www.conserve-energy-future.com>, date retrieved 21.12.2015.

[5] **Url-3**, <http://www.nordex-online.com>, date retrieved 30.03.2016.

[6] **Url-4**, <http://www.small-generator.com>, date retrieved 12.12.2015.

[7] **Url-5**, <http://michiganradio.org>, date retrieved 12.12.2015.

[8] **Yücedağ, O. M.**, **Yücedağ, S. M. and Serim, H. A.** (2013). Radar cross section calculation of a wind turbine modeled by PEC canonical structures, *Proceedings of IEEE International Conference on Electrical and Electronics Engineering*, Bursa, Turkey, pp.562–565.

[9] **Theil, A.**, **Schouten, M. W. and de Jong, A.** (2010). Radar and wind turbines: A guide to acceptance criteria, *Proceedings of the 2010 IEEE Radar Conference*, Washington, DC, USA, pp.1355–1361.

[10] **Matthews, J. C.**, **Sarno, C. and Herring, R.** (2008). Interaction of wind turbines with radar systems, *Proceedings of the 2008 Antennas and Propagation Conference*, Loughborough, UK, pp.461–464.

[11] **De la Vega, D.**, **Matthews, J. C.**, **Norin, L. and Angulo, I.** (2013). Mitigation techniques to reduce the impact of wind turbines on radar services, *Energies*, *6*(6), 2859–2873.

[12] **Poirier, R.** (2010). *Technical information and coordination process between wind turbines and radiocommunication and radar systems*, Technical Report, Ottawa, Canada.

[13] **Theil, A. and Van Ewijk, L. J.** (2007). Radar performance degradation due to the presence of wind turbines, *Proceedings of the 2007 IEEE Radar Conference*, Boston, MA, USA, pp.75–80.

[14] **Office of the Director of Defense Research and Engineering** (2006). *Effect of windmill farms on military readiness*, Technical Report to the Congressional Defense Committees, USA.

[15] **Aldirmaz, S.**, **Saynak, U.**, **Karabayir, O.**, **Coskun, A. F.**, **Serim, H.**, **Karahan, S.**, **Unal, M.**, **Bati, B.**, **Bati, O.**, **Colak, M. A.** *et al.* (2013). Wind turbine effects on radar performance, *Signal Processing and Communications Applications Conference (SIU) 2013*, Lefkosa, Mersin, Turkey, pp.1–4.

[16] **Borely, M.** (2010). *Guidelines on how to assess the potential impact of wind turbines on surveillance sensors*, Technical Report, Eurocontrol, June.

[17] **Jackson, C.** (2007). Windfarm characteristics and their effect on radar systems, *Proceedings of the 2007 IET International Conference*, Edinburgh, UK, pp.1–6.

[18] **Hubbard, O.**, **Ding, Z.**, **Ghadaki, H.**, **Wang, J. and Ponsford, T.** (2008). Advanced mitigating techniques to remove the effects of wind turbines and wind farms on primary surveillance radars, *IEEE Radar Conference 2008*, Rome, Italy, pp.1–6.

[19] **Lute, C. and Wieserman, W.** (2011). ASR-11 radar performance assessment over a wind turbine farm, *IEEE Radar Conference 2011*, Kansas City, MO, USA, pp.226–230.

[20] **Wang, J.**, **Lok, Y. F.**, **Hubbard, O.**, **Fournier, B. and Palevsky, A.** (2013). Impact of wind turbines On ATC radars and mitigation results, *IEEE Radar Conference 2013*, Ottawa, ON, Canada, pp.1–4.

[21] **Hood, K.**, **Torres, S. and Palmer, R.** (2010). Automatic detection of wind turbine clutter for weather radars, *Journal of Atmospheric and Oceanic Technology*, *27*(11), 1868–1880.

[22] **Kong, F.**, **Zhang, Y. and Palmer, R.** (2012). Wind turbine clutter mitigation for weather radar by adaptive spectrum processing, *IEEE Radar Conference 2012*, Atlanta, GA, USA, pp.471–474.

[23] **Wang, W.Q.** (2013). Detecting and mitigating wind turbine clutter for airspace radar systems, *The Scientific World Journal*, *2013*, 1–8.

[24] **Nai, F.**, **Palmer, R. D. and Torres, S. M.** (2011). Range-Doppler domain signal processing to mitigate wind turbine clutter, *IEEE Radar Conference 2011*, Kansas City, MO, USA, pp.841–845.

[25] **Jia, Q.**, **Wu, R. and Wang, X.** (2012). Recognition and supression of wind farm clutter via dynamic clutter map, *Signal Processing (ICSP), 2012 IEEE 11th International Conference on, volume 3*, Beijing, China, pp.1949–1952.

[26] **Isom, B.** (2007). *Characterization and mitigation of wind turbine clutter for the WSR-88D radar network*, Ph.D. Thesis, University of Oklahoma.

[27] **Mishra, K. V. and Chandrasekar, V.** (2010). Signal analysis and modeling of wind turbine clutter in weather radars, *IEEE International Geoscience and Remote Sensing Symposium 2010*, Honolulu, HI, USA, pp.3561–3564.

[28] **Gallardo-Hernando, B.**, **Muñoz-Ferreras, J.**, **Pérez-Martínez, F. and Aguado-Encabo, F.** (2011). Wind turbine clutter observations and theoretical validation for meteorological radar applications, *Radar, Sonar & Navigation, IET*, *5*(2), 111–117.

[29] **Karabayir, O.**, **Yucedag, S. M.**, **Coskun, A. F.**, **Yucedag, O. M.**, **Serim, H. A. and Kent, S.** (2014). Wind turbine signal modelling approach for pulse Doppler radars and applications, *IET Radar, Sonar & Navigation*, *9*(3), 276–284.

[30] **Hansen, K.**, **Thomsen, A.**, **Riis, M.**, **Marqversen, O.**, **Pedersen, M. and Nielsen, E.** (2012). Detection and tracking of aircraft over wind farms using scanter 4002 with embedded tracker 2, *Proceedings of the IET International Conference*, Glasgow, UK, pp.1–6.

[31] **Thomsen, A.**, **Marqversen, O.**, **Pedersen, M.**, **Moeller-Hundborg, C.**, **Nielsen, E.**, **Jensen, L. and Hansen, K.** (2011). Air traffic control at wind farms with TERMA SCANTER 4000/5000, *IEEE Radar Conference 2011*, Kansas City, MO, USA, pp.247–252.

[32] **Ling, H.**, **Hamilton, M.**, **Bhalla, R.**, **Brown, W.**, **Hay, T.**, **Whitelonis, N.**, **Yang, S. and Naqvi, A.** (2013). *Assessment of offshore wind farm effects on sea surface, subsurface and airborne electronic system*, Final Report for DE-EE0005380, Department of Energy.

[33] **Rüegg, M.**, **Meier, E. and Nüesch, D.** (2007). Vibration and rotation in millimeter-wave SAR, *Geoscience and Remote Sensing, IEEE Transactions on*, *45*(2), 293–304.

[34] **Clemente, C. and Soraghan, J. J.** (2012). Vibrating target micro-Doppler signature in bistatic SAR with a fixed receiver, *Geoscience and Remote Sensing, IEEE Transactions on*, *50*(8), 3219–3227.

[35] **Clemente, C. and Soraghan, J. J.** (2012). Analysis of the effect of wind turbines in SAR images, *Proceedings of the IET International Conference*, Glasgow, UK, pp.1–4.

[36] **Chu, T. H.**, **Lin, D. B. and Kiang, Y. W.** (1989). Microwave diversity imaging of perfectly conducting object in the close near-field region, *Antennas and Propagation Society International Symposium, 1989. AP-S. Digest*, San Jose, CA, USA, pp.82–85.

[37] **Ozdemir, C.** (2012). *Inverse synthetic aperture radar imaging with MATLAB algorithms*, John Wiley & Sons.

[38] **Jenn, D. C.** (1995). *Radar and laser cross section engineering*, Washington, DC: American Institute of Aeronautics and Astronautics, Inc, 1995.

[39] **Mahafza, B. R.** (2002). *Radar systems analysis and design using MATLAB*, Chapman and Hall/CRC; 3 edition.

[40] **Skolnik, M. I.** (1970). *Radar handbook*, McGraw-Hill Education; 3 editionn.

[41] **Richards, M. A.** (2005). *Fundamentals of radar signal processing*, McGraw-Hill Education; 2 edition.

[42] **Xiaowei, C., Jiajun, L. and Jie, Z.** (2006). Performance Analysis of Track Initiation Algorithm, *2006 6th World Congress on Intelligent Control and Automation*, volume 1, pp.4239–4243.

[43] **Li, X. R. and Jilkov, V. P.** (2003). Survey of maneuvering target tracking. Part I. Dynamic models, *Aerospace and Electronic Systems, IEEE Transactions on*, *39*(4), 1333–1364.

[44] **Gul, E.** (1994). On the track similarity test in track splitting algorithm, *IEEE transactions on aerospace and electronic systems*, *30*(2), 604–606.

[45] **Url-6**, <http://csclab.murraystate.edu>, date retrieved 22.12.2015.

[46] **Wiley, C.**, (1989), Pulsed Doppler Radar Method and Means, US Patent, No: 3,196,436t, dated July 1965.

[47] **Sherwin, C. W., Ruina, J. and Rawcliffe, R.** (1962). Some early developments in synthetic aperture radar systems, *IRE Transactions on Military Electronics*, *2*(MIL-6), 111–115.

[48] **Cutrona, L. J., Leith, E. N., Palermo, C. J. and Porcello, L. J.** (1960). Optical data processing and filtering systems, *Information Theory, IRE Transactions on*, *6*(3), 386–400.

[49] **Lacomme, P.** (2001). *Air and spaceborne radar systems: An introduction*, 108, William Andrew.

[50] **Jenn, D. and Ton, C.** (2012). Wind turbine radar cross section, *International Journal of Antennas and Propagation*, *2012*, 1–14.

[51] **Kong, F., Zhang, Y., Palmer, R. and Bai, Y.** (2011). Wind turbine radar signature characterization by laboratory measurements, *IEEE Radar Conference 2011*, Kansas City, MO, USA, pp.162–166.

[52] **Pinto, J., Brown, A., Rashid, L. and Moore, Z.** (2006). *Requirements capture summary report*, Technical Report, Stealth Technology for Wind Turbines, TP/2/RT/6/I/10117 APPS2B.

[53] **Balanis, C. A.** (2012). *Advanced engineering electromagnetics*, Wiley Online Library.

[54] **DiCaudo, V. and Martin, W.** (1966). Approximate solution to bistatic radar cross section of finite length, infinitely conducting cylinder, *Antennas and Propagation, IEEE Transactions on*, *14*(5), 668–669.

[55] **Norland, R.** (2003). Multipath of flat plate radar cross section measurements, *IEEE International Radar Conference, 2003*, Alabama, USA, pp.152–155.

[56] **Eugene, F. K., John, F. S. and Michael, T. T.** (2004). *Radar cross section, second edition*, SciTech Publishing.

[57] **Url-7**, `<http://www.samraksh.com>`, date retrieved 01.12.2015.

[58] **Karabayir, O.**, **Unal, M.**, **Coskun, A. F.**, **Yucedag, S. M.**, **Saynak, U.**, **Bati, B.**, **Biyik, M.**, **Bati, O.**, **Serim, H. A. and Kent, S.** (2015). CLEAN based wind turbine clutter mitigation approach for pulse-Doppler radars, *IEEE Radar Conference 2015*, Virginia, Arlington USA, pp.1541–1544.

[59] **Högbom, J.** (1974). Aperture synthesis with a non-regular distribution of interferometer baselines, *Astronomy and Astrophysics Supplement Series*, *15*, 417.

[60] **Kulpa, K.** (2008). The CLEAN type algorithms for radar signal processing, *Microwaves, Radar and Remote Sensing Symposium (MRRS) 2008*, Kiev, Ukrain, pp.152–157.

[61] **Karabayir, O.**, **Coskun, A.**, **Yucedag, O.**, **Makal Yucedag, S.**, **Serim, H. and Kent, S.** (2016). Investigation of wind farm effects on radar multiple target tracking, *Journal of Electromagnetic Waves and Applications*, *30*(2), 232–250.

[62] **Karabayir, O.**, **Yucedag, S. M.**, **Yucedag, O.**, **Coskun, A. F.**, **Serim, H. A. and Kent, S.** (2014). Investigation of deteriorating effects of wind farms on SAR imaging, *Signal Processing and Communications Applications Conference (SIU) 2014*, Trabzon, Turkey, pp.409–412.

[63] **Karabayir, O.**, **Yucedag, S. M.**, **Yucedag, O.**, **Serim, H. A. and Kent, S.** (2014). Radar Cross Section and Doppler Effects of Wind Turbines on SAR Imaging, *EUSAR 2014; 10th European Conference on Synthetic Aperture Radar*, Berlin, Germany, pp.1–4.

CURRICULUM VITAE

Name Surname: Osman KARABAYIR

Place and Date of Birth: TRABZON-TURKEY 01.Jan.1984

E-Mail: osman.karabayir@tubitak.gov.tr

EDUCATION:

- **B.Sc.:** 2007, Yıldız Technical University, Faculty of Electrical and Electronics Engineering, Electronics and Communications Engineering Programme

- **M.Sc.:** 2010, Istanbul Technical University, Department of Electronics and Communications Engineering, Telecommunications Engineering Programme

PROFESSIONAL EXPERIENCE AND REWARDS:

- 2007-2010 Nortel Netaş A.Ş. Istanbul, Turkey (Software Engineer)

- 2011-Continue, TÜBİTAK BİLGEM. Kocaeli, Turkey (Senior Researcher)

- 2007 Graduated with a first from Yıldız Technical University, Faculty of Electrical and Electronics Engineering

- 2007 Graduated with a first from Yıldız Technical University, Faculty of Electrical and Electronics Engineering, Electronics and Communications Engineering Programme

PUBLICATIONS, PRESENTATIONS AND PATENTS ON THE THESIS:

- **Karabayir O.**, Yucedag S. M., Yucedag O. M, Coskun A. F., Serim H. A. and Kent S., 2014. Investigation of deteriorating effects of wind farms on SAR imaging. *Signal Processing and Communications Applications Conference (SIU), 2014*, April 23-26, 2014 Trabzon, Turkey.

- **Karabayir O.**, Unal M., Coskun A. F., Yucedag S. M., Saynak U., Bati B., Biyik M., Bati O., Serim H. A. and Kent S., 2015. CLEAN based wind turbine clutter mitigation approach for pulse-Doppler radars. *Radar Conference (RadarCon), 2015 IEEE*, May 11-16, 2015 Arlington, Virginia, USA.

- **Karabayir O.**, Yucedag S. M., Yucedag O. M, Serim H. A. and Kent S., 2014. Radar Cross Section and Doppler Effects of Wind Turbines on SAR Imaging. *EUSAR 2014; 10th European Conference on Synthetic Aperture Radar*, June 11-16, 2014 Berlin, Germany.

- **Karabayir, O.**, Yucedag, S. M., Coskun, A. F., Yucedag, O. M, Serim, H. A. and Kent, S., 2014. Wind turbine signal modelling approach for pulse Doppler radars and applications. *IET Radar, Sonar & Navigation*, 9(3), 276-284.

- **Karabayir, O.**, Coskun, A. F., Yucedag, O. M, Yucedag, S. M., Serim, H. A. and Kent, S., 2016. Investigation of wind farm effects on radar multiple target tracking. *Journal of Electromagnetic Waves and Applications*, 30(2), 232-250.